Investigation of Fibre Volume Fraction as Key Parameter in Cryogenic Hydrogen Tank Development

Master Thesis

J.P. Appels

TUDelft

DLR

Investigation of Fibre Volume Fraction as Key Parameter in Cryogenic Hydrogen Tank Development

Master Thesis

by

J.P. Appels

TUDelft
Delft
University of
Technology

DLR **Deutsches Zentrum**
für Luft- und Raumfahrt
German Aerospace Center

Acknowledgements

Abstract

In developing Type V hydrogen tanks for energy storage and propulsion in commercial airliners, the key design criterion is maintaining tightness under cryogenic conditions. A concern is that anomalies in the laminate could cause microcracks which compromise the tightness. This study examined how resin flow, caused by an expanding mould during curing, creates a gradient in the local fibre volume fraction (FVF) across the laminate. The impact of resin system selection, autoclave cycle parameters, mandrel material, and fibre tension on the FVF gradient was investigated. Cylindrical specimens were manufactured in a process replicating automated fibre placement (AFP), with a piezoelectric sensor measuring contact pressure at the mandrel-laminate interface during the autoclave cycle as an indicator of resin flow and FVF spread. Significant correlations were found between resin flow and all parameters except fibre tension. The resin's viscosity profile and gelation characteristics had the most substantial impact on the FVF spread. Resins with high viscosity and short gelation times lowered the FVF spreads the most. Mandrel materials with lower thermal expansion coefficients (CTE) also reduced FVF gradients, though to a lesser extent. Adjusting the autoclave cycle to lower temperatures for longer periods resulted in the least significant reduction in FVF spread; however, this approach holds high potential for further improvement if more data on resin rheology and cure kinetics are available to optimise the autoclave cycle. These findings provide valuable insights for minimising FVF gradients in the design of carbon fibre-reinforced polymer (CFRP) tanks for liquid hydrogen.

Contents

List of Figures

List of Tables

Nomenclature

Abbreviations

Abbreviation	Definition
AFP	Automated Fibre Placement
BWB	Blended Wing Body
CFRP	Carbon Fibre-Reinforced Plastic
CH_4	Methane
CO_2	Carbon dioxide
CTE	Coefficient of Thermal Expansion
DLR	Deutsches Zentrum für Luft- und Raumfahrt e.V. (engl. German Aerospace Center)
DSC	Differential Scanning Calorimetry
EU	European Union
FBD	Free Body Diagram
FVF	Fibre Volume Fraction
H_2	Hydrogen
ICAO	International Civil Aviation Organization
LH_2	Liquid Hydrogen
OEW	Operating Empty Weight
TDS	Technical Data Sheet
TMA	Thermomechanical Analysis

<div align="right">

1

</div>

Introduction

Climate change is a critical global challenge and significantly threatens the environment, human health, and economic stability. The anthropogenic release of greenhouse gases, such as carbon dioxide (CO_2) and methane (CH_4), into the atmosphere leads to the greenhouse effect and subsequent global warming. This results in a higher frequency and intensity of natural disasters and disruptions to ecosystems (IPCC, 2021).

The aviation industry is vital for global connectivity and economic progression but also significantly contributes to greenhouse gas emissions. In 2018 the aviation industry was responsible for 2.4% of the worldwide CO_2 emissions from fossil fuel use (Graver et al., 2019). Within the European Union, aviation accounted for 3.8% to 4% of the greenhouse gas emissions[1]. If continuous aviation growth is allowed without further technological and operational improvements, the United Nations International Civil Aviation Organization (ICAO) expects the emissions caused by aviation to triple from 2015 to 2050, as projected in Figure 1.1. By then, they would account for 25% of global emissions (Fleming et al., 2022). This increases the challenge of limiting global temperature increases to $1.5°C$ compared to pre-industrial levels, as agreed upon in the Paris Agreement (UNFCCC, 2016).
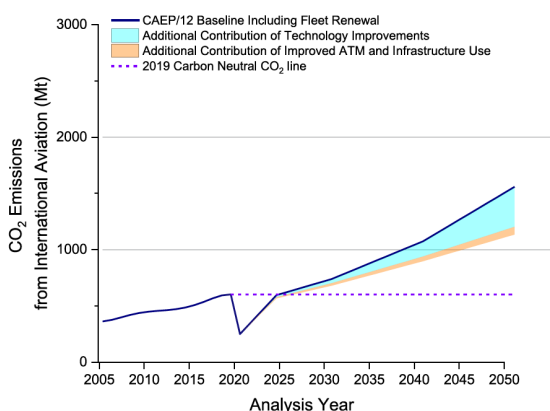
Note: Results were modelled for 2005, 2006, 2010, 2015 (Prior CAEP work cycles), 2018, 2020, 2024, 2030, 2040, and 2050 (CAEP/12).

Figure 1.1: Projected CO_2 emissions from international aviation 2005 to 2050 (Fleming et al., 2022).

---

[1] https://climate.ec.europa.eu/eu-action/transport/reducing-emissions-aviation_en [Accessed: Jul. 16, 2024]

With the pressing need to address climate change, reducing emissions from the aviation sector has become a top priority. This can only be achieved through the decarbonisation of aviation, which requires disruptive changes in technology and operations. Decarbonisation plays a key role in multiple directives such as the Green Deal by the European Commission. Its aim is net carbon neutrality among all sectors in the EU by 2050. Within this framework, policy makers set goals and implement policies to transform the economy towards carbon neutrality. For the aviation industry, this specifically includes funding research and innovation of carbon neutral energy carriers such as hydrogen, as well as creating the necessary regulatory frameworks to integrate hydrogen into aviation.

1.1. Hydrogen in Aviation

The aviation industry faces increasing societal and political pressure to find sustainable alternatives to fossil fuels. Hydrogen is progressively being recognised as a potential next-generation fuel for aviation due to its capacity for zero-emission operation, coupled with recent technological advancements and consistent support from policy makers (IEA, 2019). Hydrogen thus presents a promising solution to decarbonise the aviation sector. As fuel for combustion engines or fuel cells, hydrogen emits only water vapour, thus eliminating CO_2 emissions. This establishes hydrogen as a crucial element in the future of sustainable aviation to achieve the aviation industry's rigorous objectives for carbon footprint reduction.

Figure 1.2 compares the mass- and volumetric-specific energy of different energy carriers such as batteries, fossil fuels or hydrogen. Electric propulsion powered by batteries remains unfeasible for long-haul flights due to the fractional mass specific energy of all battery chemistries compared to fossil fuels or hydrogen. In contrast to battery powered propulsion, hydrogen seems to offer a comprehensive solution with a mass-specific energy exceeding even the fossil fuels. This however does not include the additional weight from structures and systems required for storing the fuel. While avgas and other conventional aviation fuels can be stored in lightweight tank systems in existing structures like the wing, hydrogen requires a more complex tank structure for two main reasons: Firstly, hydrogen is the first element in the periodic table and therefore the molecular size of the H_2 molecule is very small. It only consists of two protons and two electrons. Hence it is able to diffuse or leak through many materials. Secondly, due to volume constraints in an aircraft for fuel storage the hydrogen must be stored either under high pressure or even in cryogenic conditions (i.e. at cold temperatures to reach liquid form).

Figure 1.2: Mass- and volumetric-specific energy of multiple energy carriers (Drone Industry Insights, 2017).

1.2. Composite Tanks for Cryogenic H$_2$ Storage

The integration of a tank for the storage of hydrogen poses new challenges for aircraft construction. On the one hand, this is due to the significantly lower volumetric energy density of liquid hydrogen compared to aviation fuels. Switching from kerosene tanks to liquid hydrogen tanks more than triples the required tank volume for the same energy content, as observed in Figure 1.2. For kerosene, the wing structures serve a dual function as both a lift generating surface and the enclosure structure for the kerosene. This dual function advantage vanishes for hydrogen tanks as they require a cylindrical tank shape to stand the internal pressure, and thus cannot efficiently be fitted into conventional airliner wings. Currently ongoing holistic developments of next generation airliners such as the *Flying V* by TU Delft or the BWB model as part of the ZEROe strategy by Airbus tackle this problem by introducing blended-wing body designs that combine the aerodynamic surfaces and the fuselage in one combined structure. In addition, the hydrogen tank requires a complex insulation structure to strictly limit heat inflow. A promising design solution is a vacuum insulation layer around the tank. Figure 1.3 illustrates a possible hydrogen tank design with a vacuum insulation structure.

Taking various aircraft concepts into account, an increase in aircraft operational empty weight (OEW) of approximately 23% is expected as a result of the required LH2 tank structure (Airbus Deutschland GmbH et al., 2003). This significant increase in weight makes it imperative to develop more lightweight design concepts for cryogenic hydrogen tanks.
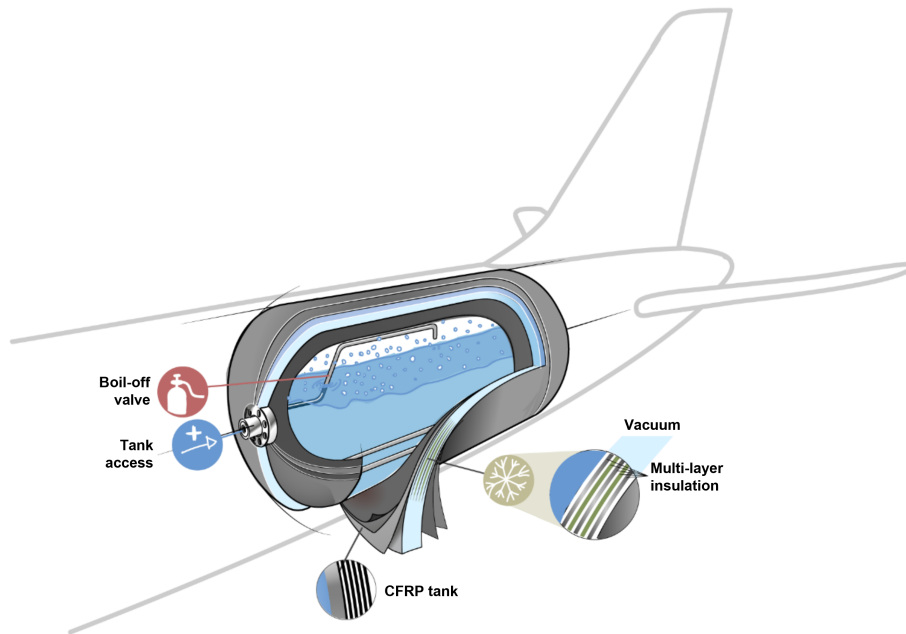
Figure 1.3: Potential design of cryogenic hydrogen tank in aircraft with vacuum insulation (Adapted from DLR).

In general, hydrogen tanks are classified as *Type I, II, III*, or *IV*. The differences between each type are shown in Figure 1.4. *Type I, II*, and *III* tanks have metallic liners. *Type I* tanks consist purely of metal, while *Type II* and *III* tanks have a composite material wrapped around either the cylindrical part only or both the cylindrical part and the dome area of the tank. *Type IV* is wrapped in composite material, similar to *Type III*, but the liner is made of a polymeric material. *Type V*, which is currently in development, should have no liner at all and is supposed to ensure leak tightness only by the composite material.

Tanks of *Type I* and *II* are not weight-optimised and therefore not ideal for aviation use. *Type III* is problematic in cryogenic use due to the high discrepancy in the coefficients of thermal expansion between metal and CFRP, which would quickly lead to delamination of the metal liner from the composite shell. Hence, *Type IV* and *V* are of main interest for lightweight cryogenic hydrogen storage. The DLR Institute for Lightweight Systems directed its research and development efforts mainly toward a liner-less (*Type V)* hydrogen tank, as it has the potential to be more lightweight, simpler to manufacture, more fatigue resistant as it consists of only one material or composite (Azeem et al., 2022), and less complex to certify without a liner.
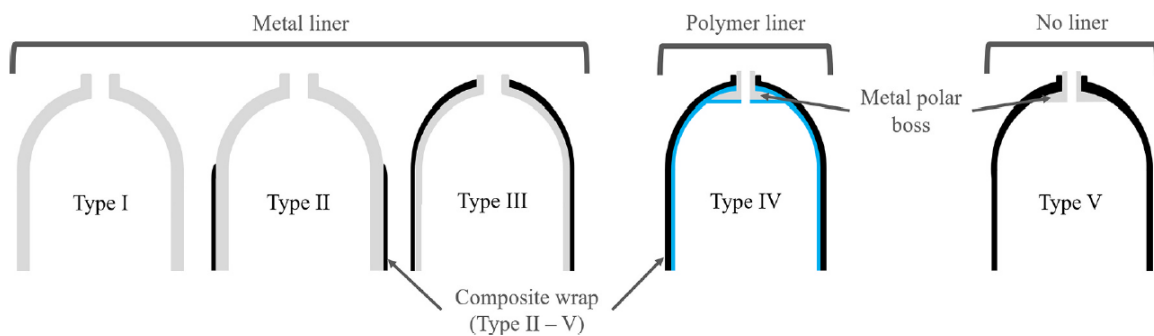
Figure 1.4: Pressure vessel types I to V (Air et al., 2023).

When using *Type V* tank systems made purely from composite materials in combination with hydrogen, a major challenge is to limit permeability, i.e. the ability of hydrogen to penetrate the composite material. Two effects can contribute to permeability. One is diffusion, and the other is leakage. Diffusion considers a three-step process in which the hydrogen molecules are absorbed at the composite surface, travel through the material in diffusion, and are desorbed at the opposite surface. During leakage, the hydrogen molecules penetrate the composite via microcracks and do not enter the state of diffusion.

The permeation through leakage increases with the number and size of microcracks. The occurrence of microcracks is a challenge in cryogenic tanks. The different coefficients of thermal expansion of the fibres versus the matrix result in high loads when the component is cooled from ambient to cryogenic temperatures. This can lead to microcracks in the matrix. Multiple microcracks may form a critical leakage path through which hydrogen can leak out of the tank. In manufacturing a tank suitable for hydrogen, composite material, laminate lay-up, and manufacturing parameters must be selected such that the leak-tightness requirements are met in the final product. Multiple projects at the DLR Institute for Lightweight Systems are pursued in parallel to create such a product together with respective partners.

1.3. DLR Project Background

The DLR Institute for Lightweight Systems is heavily involved in the industrial development of a cryogenic hydrogen tank of *Type V* for next-generation aircraft. DLR is collaborating with its industrial partners to enable this key technology. A stepwise approach is followed to break down the development of hydrogen tanks into smaller steps with increasing complexity and size as visualised in Figure 1.5. The planar specimens in the beginning allow for coupon tests which mainly serve the material screening. The single curved specimens introduce multiple effects related to the curvature of the tank and the small- and full-scale tank demonstrators introduce the full complexity with double curvature and complex material deposition strategy.
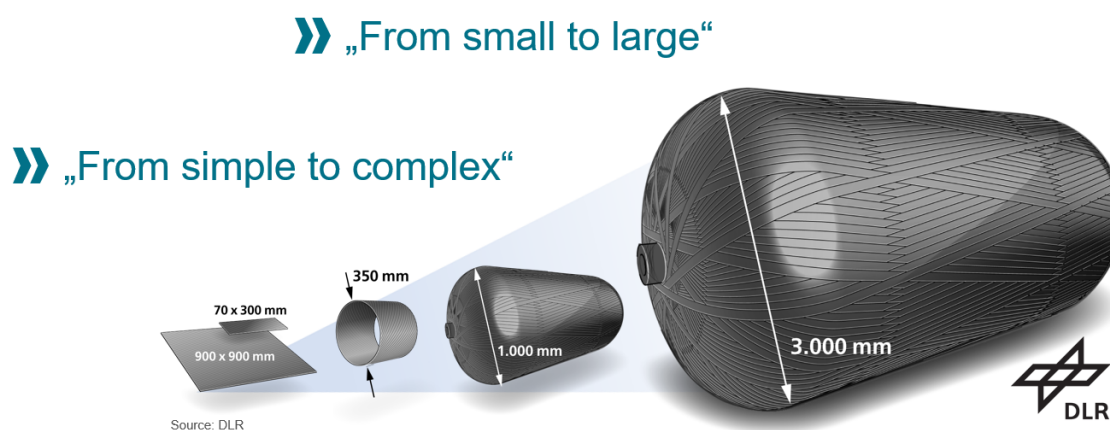
Figure 1.5: Increasing complexity and size of samples in development of hydrogen tank (Adapted from DLR internal documents).

Testing of materials, samples or demonstrators is performed in different environments. The test pyramid in Figure 1.6 illustrates some of the tests that must be executed on the way towards certification. Standard tests like uniaxial tension or compression, torsion and bi-axial

loading tests are performed in the beginning. Additional thermal loads are added by performing the tests in cryogenic conditions. In the early phases, cooling the specimens is done with liquid nitrogen for reasons of convenience and safety. Later in more advanced tests, liquid hydrogen is used. A similar strategy is used for permeability tests which are performed with helium in the beginning, and later change to hydrogen.
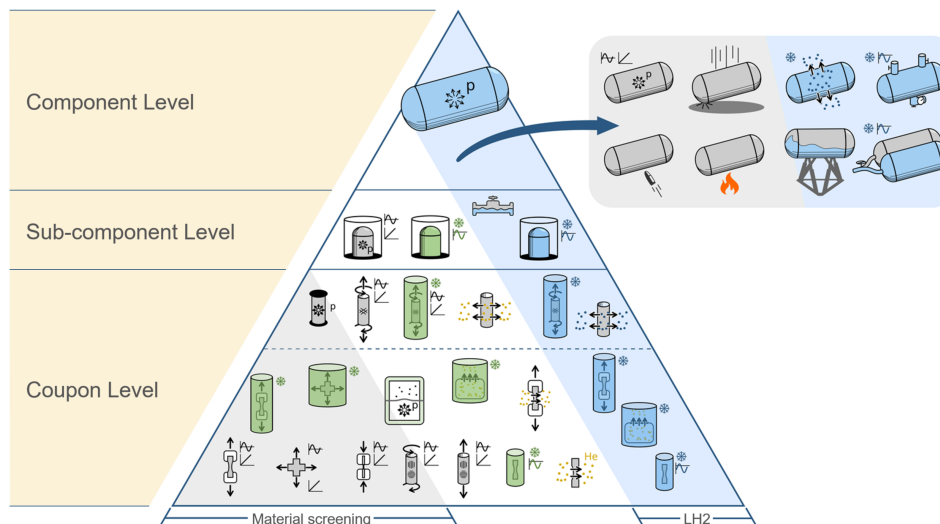
Figure 1.6: Overview of coupon and component tests for development of hydrogen tank (Adapted from DLR internal documents).

1.4. Resin Flow as a Concern in Cryogenic Type V Hydrogen Tanks

During manufacturing of a *Type V* hydrogen tank with thermoset pre-preg, tows are deposited on a mandrel using an automated fibre placement (AFP) or winding process. The mandrel provides the shape of the future tank. Mandrels are usually metal tools with a coefficient of thermal expansion (CTE) significantly different from that of CFRP, which typically has a CTE of zero or even slightly negative (Joven et al., 2012). Typically, mandrels are made of aluminium or steel. Both have positive CTE values. The difference in CTE between fibres and mandrel is particularly notable in layouts where the fibres are placed in a circumferential direction around the mandrel. During the cure cycle, heat is applied to cure the resin. The heat causes the mandrel to expand and the fibres to build up tension as they are wrapped around the mandrel but expand less than the mandrel. An important effect caused by fibre tension is visualised in Figure 1.7. The fibres are wound onto the mandrel with fibre tension F_T. Due to the curvature, each individual ply exerts an inward pressure p_f. It can be assumed that the pressure from each ply will superimpose on the pressure from the ply above and thus build up to the maximum expected closest to the mandrel. However, this only applies to fibres that are wound in the circumferential direction and wrap around the full circumference. Fibres placed orthogonally, i.e. parallel to the mandrel axis, are placed without curvature and therefore do not create inward pressure.

A curing step is required to finish the laminate. This can be done in an autoclave or in an oven. Heat is applied to initiate the chemical curing process of the thermoset resin. Due to the positive CTE of metals, the mandrel undergoes thermal expansion and its diameter increases. However, carbon fibres have a slightly negative CTE, as explained in more detail in subsection 1.5.1, and therefore shrink with increasing temperature. As a result, the fibre

F$_T$ Fibre tension

p$_f$ Pressure due to fibre tension
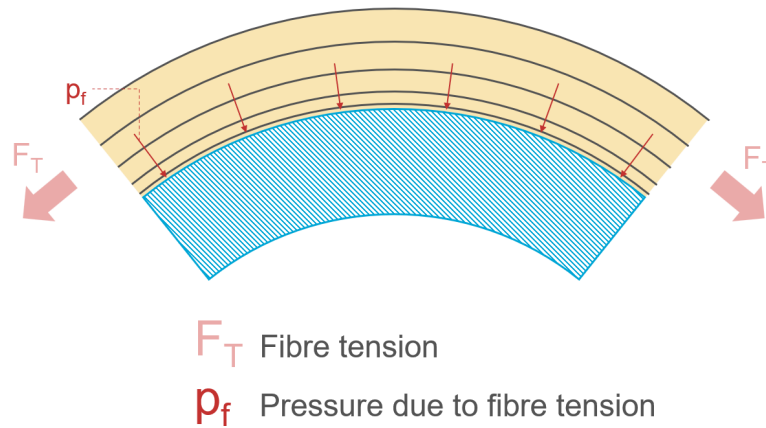
Figure 1.7: Fibres wrapped with tension around a curved tool exert pressure on the tool.

tension and the pressure from Figure 1.7 increase even further.

The second effect of heat is to affect the viscosity of the resin. In prepreg systems at low temperatures the resin has a relatively high viscosity with limited ability to flow. As the temperature increases, the molecular mobility increases, and the viscosity drops low enough to allow the resin to flow for a certain time window. At some point, once gelation is reached, too many cross-links have formed, causing the viscosity to rise rapidly and the flow to stop.

The combination of the pressure exerted by the expanding tool and the low viscosity of the resin during this particular time window can be imagined as a wet towel wrapped under tension around a cylindrical rod. The liquid, or resin, is squeezed out and begins to flow. This phenomenon of resin flow is illustrated in Figure 1.8. The outward flow of resin results in a change in fibre volume fraction (FVF) as the inside of the laminate is resin-deficient, while the outside of the laminate is much more resin-rich.
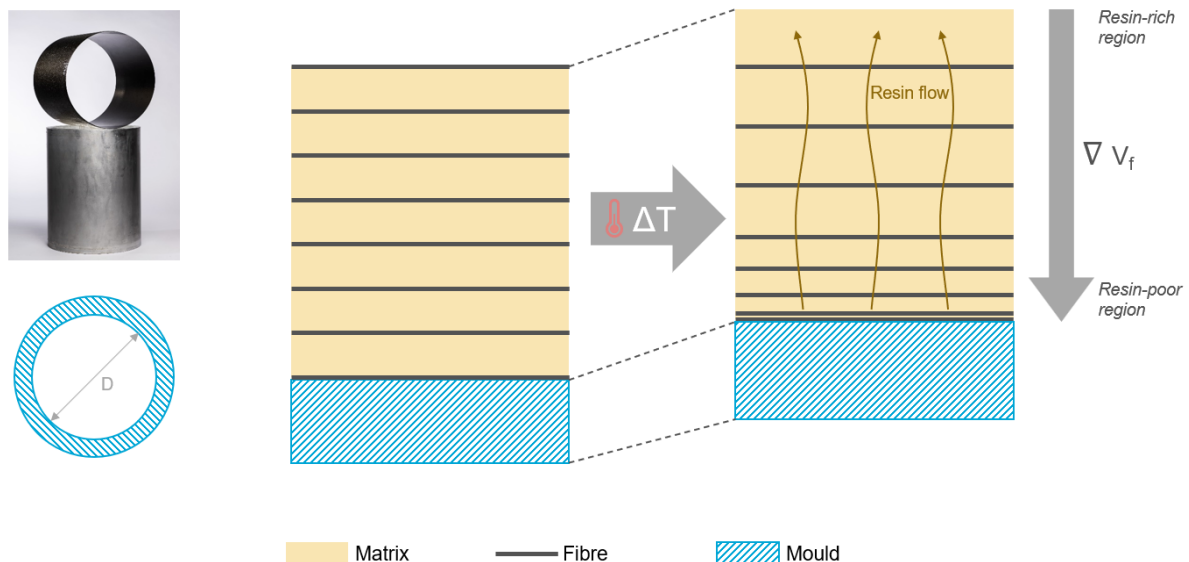
Figure 1.8: The increase in fibre tension and pressure due to the thermal expansion pushes the resin outwards. It results in a gradient in the FVF.

Concern

It is hypothesised that in the warm state, when the resin is relatively fluent, fibres with high tension will move inwards, inducing an outward resin flow. However, the fluent state is preserved only for a limited duration as indicated by the manufacturer's viscosity profiles. This intricate situation results in a gradual FVF through thickness. The FVF is an important parameter that material suppliers set to very precise levels to achieve the desired material properties. A deviation from the predefined volume fraction during the manufacturing process is an unintentional deviation. This raises the concern that this gradient might intensify the initiation and propagation of micro-cracks which ultimately could lead to undesirable leakage of hydrogen through the CFRP wall structure.

To better understand the phenomenon of resin flow, it is essential to identify the most influential parameters. A suitable theory describing the flow of a viscous medium through a porous medium is Darcy's law (Darcy, 1856). He described flow as a function of permeability, viscosity and pressure. Permeability depends on the size and packing of the fibres. The higher the permeability, the easier it is for the resin to flow. The viscosity of the resin is important as it will only flow within a certain viscosity range. If the viscosity is too high, the flow slows down or stops altogether. Pressure drives resin flow - higher pressure results in more resin flow. Permeability, viscosity and pressure are the important parameters that need to be studied more closely. The thesis at hand aims to prove, understand and ideally control the resin flow. To achieve this, a parametric study is planned in which the phenomenon will be isolated as much as possible using single curved tools (i.e. mandrels) of different materials (aluminium and steel). One of these mandrels is shown in Figure 1.9 with a CFRP specimen on top.

Figure 1.9: Single-curved mandrel made from Aluminium with CFRP probe on top from previous experiments. Diameter 350mm, height 450mm (DLR).

1.5. Literature Overview

The following section provides an overview of the existing literature on the phenomenon of resin flow in the direction of thickness in single-curved composite structures. It is assumed that the resin flow is caused by a discrepancy in CTE between the metal mandrels and the carbon fibres. The literature overview thus starts with a section on the CTE values and their implications. It then continues with theoretical models and experiments described in the scientific literature that are relevant to resin flow.

1.5.1. CTE of Carbon Fibres and Relevant Metals

In the manufacturing of CFRP components the material is deposited on special tools that provide support and shape to the laminate. The combined tool and laminate undergo a curing process in an autoclave. During this process, the temperature rises from room temperature to $175°C$ [2]. Every material exhibits a certain amount of thermal expansion or contraction. The linear coefficient of thermal expansion, α_L or CTE, can be written as

$$\alpha_L = \frac{1}{L}\frac{dL}{dT} \tag{1.1}$$

where L is the linear size of the sample and T is the temperature. It can be assumed that α_L remains constant throughout the relevant temperature range from $20°C$ to $175°C$. Wilson (1941) and Yakout et al. (2018) showed that the increase in CTE of aluminium is smaller than $+4 \cdot 10^{-6} m/mK$ and for steel smaller than $+3 \cdot 10^{-6} m/mK$ between $20°C$ and $200°C$. Pradere and Sauder (2008) showed in their study that the CTE of carbon fibres does not change noticeably between $300K$ and $500K$. The change in linear dimension can therefore be written as

$$\frac{\Delta L}{L} = \alpha_L \Delta T \tag{1.2}$$

Table 1.1 lists the linear CTE of the relevant materials. Torayca® T700G is a Toray carbon fibre with mechanical properties close to those of the carbon fibres used for the thesis experiments. No CTE data was available for the actual carbon fibres.

Table 1.1: Overview of the linear CTE values of various materials.

Material	CTE [$\cdot 10^{-6}$m/mK] at 20 $°C$	Source
Aluminium 6082	24	Link[3]
Steel S355	12	Link[4]
Invar 36	2.0 [20-150$°C$]	Link[5]
Torayca® T700G (carbon fibre)	-0.3	TDS of Torayca®[6]
Torayca® T300 (carbon fibre)	-0.6	Mallick (2018)

---

[2] Based on the recommended curing cycle of HexPly® 6376.
[3] https://www.thyssenkrupp-materials.co.uk/aluminium-6082.html [Accessed: Nov. 20, 2023]
[4] https://eurocodeapplied.com/design/en1993/steel-design-properties [Accessed: Nov. 20, 2023]
[5] https://www.sandmeyersteel.com/spanish/ssc-invar36.html [Accessed: Nov. 20, 2023]
[6] https://www.toraycma.com/wp-content/uploads/T700G-Technical-Data-Sheet-1.pdf [Accessed: Jan. 24, 2024]

Carbon fibres exhibit special behaviour when exposed to heat because they are one of the few materials with a negative coefficient of thermal expansion in the longitudinal direction. This is due to the atomic structure of the carbon fibres. As shown in Figure 1.10, a carbon fibre consists of graphite crystallites made up of layered basal planes that contain hexagonal covalently bonded carbon atoms. These covalent bonds give the material its high stiffness in the fibre direction. Between the basal planes are the weaker Van-der-Waals bonds (Langston, 2016).

As the material heats up, the carbon atoms increasingly vibrate in the direction normal to the basal planes because they are less constrained by the Van-der-Waal forces in this direction. Because of the out-of-plane osscilation, the distance between the atoms in the plane reduces. Hence, the hexagonal rings and, with that, the basal planes get smaller. The basal planes are aligned with the longitudinal direction of the fibre. As a consequence, the described anisotropic behaviour causes the fibre to shrink as the temperature increases (Geng et al., 2018).
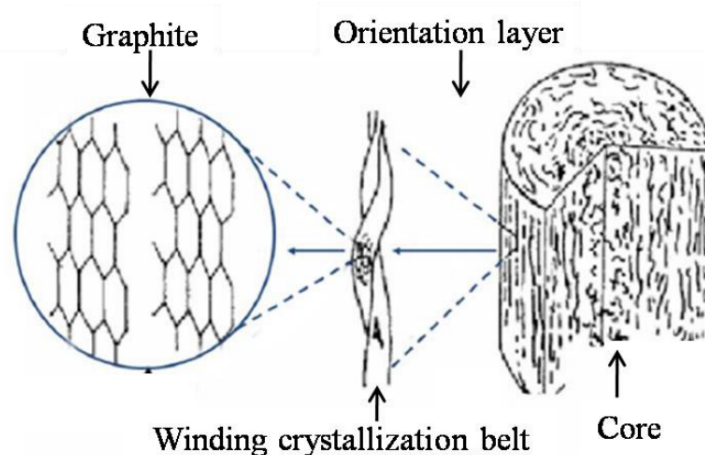
Figure 1.10: Schematic diagram of carbon fibre structure. On the left two basal planes are depicted (Liu et al., 2020).

Aluminium and steel have a positive CTE, which may vary slightly depending on the alloy and grade selected. For the selected grades, aluminium has a CTE twice that of steel. Another special material developed specifically for low thermal expansion is Invar, a nickel-iron alloy with a nickel content of exactly 36%, which minimises the value of CTE. If the large thermal expansion of a tool during the manufacturing process of a CFRP part is unacceptable, Invar can be a solution for the choice of tool material. However, it should be noted that Invar is considerably more expensive than more conventional metals such as aluminium and steel. In addition, the use of Invar for rotationally symmetric tools is limited because the finished part will not shrink free upon cooling, which presents an immense challenge to the demoulding strategy.

The large discrepancy in the thermal expansion coefficients between conventional tool metals, i.e. aluminium and steel, and carbon fibres are believed to play a key role in causing the resin flow effect mentioned as a concern in section 1.4.

1.5.2. Resin Flow Phenomenon

While AFP manufactured CFRP tanks for cryogenic hydrogen storage are still under development, CFRP has been used in fibre-wound pressure vessels for gases for a longer period of time. Therefore, there is a much larger base of experience around the topic of tank winding technology. The similarities with an AFP process are significant. Therefore, the experience is still very applicable. For instance, already in the early 1990s, wet winding experiments were carried out showing resin flow in the thickness direction.

The flow of resin in the thickness direction has been found to affect the local FVF, as discovered by Hahn and Lee (1992) and Pérès et al. (2017). Traditionally, only winding experiments have been carried out in which fibre bundles are drawn through liquid resin and then wound around a mandrel. Accurate regulation of the tension of the fibres during winding is necessary to control the position in which the fibres are deposited on the mandrel and to prevent wrinkles and undulations, as Sbanca et al. (2023) explains. For more complex shapes, Sbanca et al. developed a variable tensioning system that adapts the tension during the process.

In the following, selected theoretical resin flow models and experimental investigations relating to resin flow in thickness direction are presented.

Theoretical Resin Flow Models

The theory behind resin flow has already been described in literature from the 1980s and 1990s. Tzeng (1988) developed a detailed analytical model for resin flow called the *Layer Tension Loss Model*. The title already hints at the cause of resin flow, which is the release of fibre tension accompanied by resin flow. Tzeng postulated that the inward motion of a fibre is equal to the displaced volume of resin and built the model from the perspective of the fibre. Therefore, it is assumed that the resin flows through the fibre grid rather than the fibres sliding through the resin, allowing for the application of Darcy's law. The equation proposed by Darcy in 1856 describes the flow of a viscous medium through a porous medium as a function of permeability, viscosity, and pressure difference.

Another theoretical model was developed and published in three companion papers by Calius and Springer (1990), Lee and Springer (1990) and Calius et al. (1990). Their model was also based on Darcy's equation, but there are differences in the assumptions made. Tzeng's model was limited to cylinders with thin wall thickness compared to the mandrel diameter, whereas Calius, Lee and Springer specifically developed their model with applicability for thick cylinders as well. The criteria for determining whether a thickness-to-diameter ratio is considered thin or thick are unclear in the above-mentioned publications.

Additionally, Calius, Lee, and Springer assumed that the fibres move through the resin, while Tzeng assumed that the resin flows through the fibres. These perspectives do not contradict each other; they simply represent different reference frames and their subsequent effects on the mathematical model.

Tzeng utilised the following form of Darcy's equation, which is applicable for anisotropic porous media:

$$\vec{q} = -\left(\frac{1}{\mu}\right)[S]\vec{\nabla}P \tag{1.3}$$

Here, $\vec{q}$ represents the resin flow rate, μ the resin viscosity, $[S]$ the permeability tensor of the composite and $\vec{\nabla}P$ is the pressure gradient due to fibre tension.

Calius, Lee, and Springer employed the same approach, albeit in a slightly different mathematical representation.

Each parameter in the equation (i.e. resin viscosity, fibre sheet permeability and pressure gradient) is the result of a separate model, which will be briefly discussed below.

Resin Viscosity   The resin viscosity μ is a function of the degree of cure α and the temperature T. For thin-walled cylindrical laminates, α and T can be determined by a thermochemical model as proposed by Calius and Springer (1990). The authors used a differential equation based on the conservation of energy. For an axisymmetric structure, assuming that it has constant properties along its axis z, and its azimuth ϕ,

$$\rho C \frac{\partial T}{\partial t} = \frac{1}{r} \frac{\partial}{\partial r} \left(r \kappa \frac{\partial T}{\partial r} \right) + \rho \dot{H} \tag{1.4}$$

where

- T refers to the temperature inside the composite and mandrel,
- t is the time,
- r the radial coordinate as specified in Figure 1.11,
- $\dot{H}$ is the rate of heat generation due to the exothermic nature of the curing reaction of thermoset resins,
- ρ is the density,
- κ is the transverse thermal conductivity and
- C is the specific heat of the composite.

In his dissertation Tzeng (1988) used a similar approach with the same differential equation but extended it to include changes along the z-axis. For the sake of simplicity, no changes along z were assumed in this report and the approach of Calius and Springer (1990) was continued.
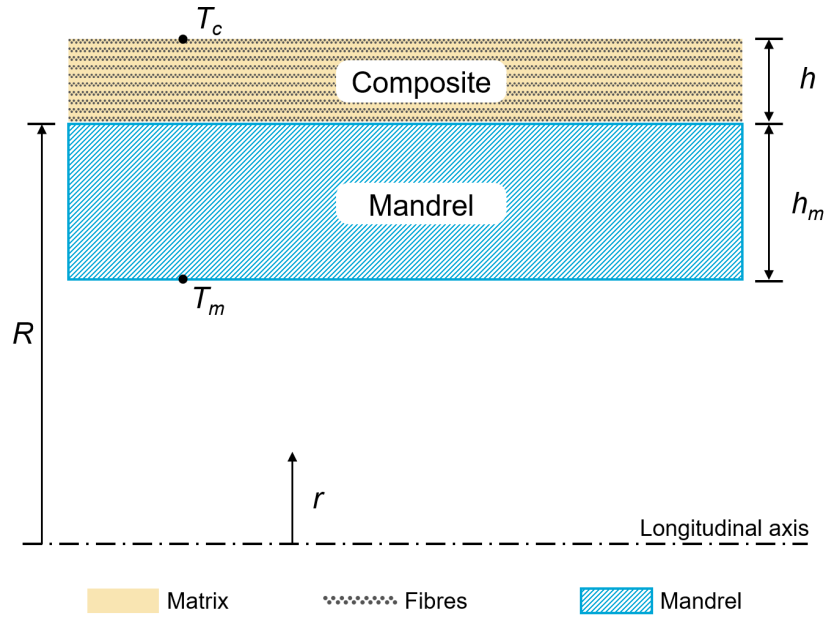
Figure 1.11: Illustration of the radial coordinate r in the cylinder, consisting of mandrel and composite (Adapted from Calius and Springer (1990)).

As defined by Mallick (2018), the degree of cure α at any time t is defined as

$$\alpha = \frac{H}{H_r} \tag{1.5}$$

where H_r is the total heat released during the curing reaction from $\alpha = 0$ to $\alpha = 1$ and H is the heat released from the start t_0 until present time t. Rearranging and differentiating Equation 1.5 over time yields

$$\dot{H} = \left(\frac{d\alpha}{dt}\right) H_r \tag{1.6}$$

Substitution of Equation 1.6 into Equation 1.4 yields

$$\rho C \frac{\partial T}{\partial t} = \frac{1}{r}\frac{\partial}{\partial r}\left(r\kappa\frac{\partial T}{\partial r}\right) + \rho H_r \frac{d\alpha}{dt} \tag{1.7}$$

As there are two unknowns in the equation, α and t, a second equation is required to obtain a solution. This equation can be obtained from the experimental cure kinetics of the particular resin, expressing $\frac{d\alpha}{dt}$ as a function of α and t. This is usually done by differential scanning calorimetry (DSC) or alternatively by specific models, which are briefly described later in this section. For now, the expression is kept general as

$$\frac{d\alpha}{dt} = f_1(\alpha, t) \tag{1.8}$$

To solve the differential equation, the initial and boundary conditions must be known. The initial conditions can be written as

$$T = T_0 \quad \text{and} \quad \alpha = \alpha_0 \quad \text{at} \quad t = t_0 \tag{1.9}$$

The boundary conditions are set by the temperatures at the points T_c and T_m, as seen in Figure 1.11, and must be known at all times.

$$\left.\begin{array}{ll} T = T_c & \text{at } r = R + h \\ T = T_m & \text{at } r = R - h_m \end{array}\right\} \quad t > 0 \tag{1.10}$$

Equations 1.7 to 1.10 can be used to solve the differential equation. The authors proposed a numerical solution method. As a result, the values for α and T are known as functions of radial position r and time t. Finally, once α and T are known, the resin viscosity, μ, can be determined. It can be written as a function of α and T which are found by solving the differential equation 1.4.

$$\mu = f_2(\alpha, T) \tag{1.11}$$

f_2 is a function of the resin viscosity, which unfortunately has to be determined experimentally or approximated by special models for each resin system. An example is given below.

Potential Models for $f_1(\alpha, t)$ and $f_2(\alpha, T)$ In general, as Ermanni (2007) explains, the viscosity decreases with increasing temperature until the chemical crosslinking increases. The increase in cross-linking leads to an increase in viscosity. This is qualitatively illustrated in Figure 1.12.
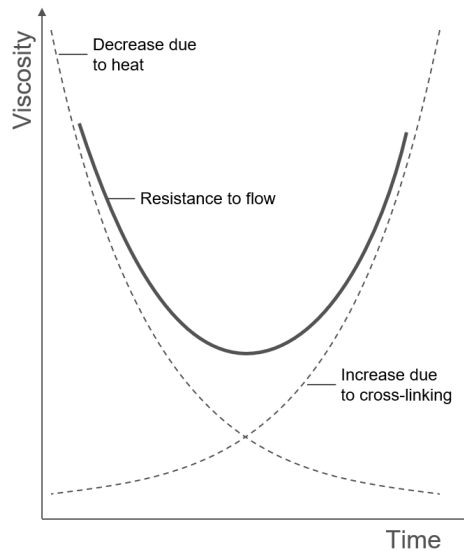
Figure 1.12: Qualitative viscosity vs. time graph of thermoset resin system (Adapted from Ermanni (2007)).

Ermanni (2007) gives examples of models commonly used to describe cure rate $\frac{d\alpha}{dt}$ and viscosity μ, referred to as $f_1()$ and $f_2()$ in Equation 1.8 and 1.11.

For epoxies, polyesters and polyurethanes, Ermanni (2007) suggested to approximate the cure rate according to Kamal and Sourour (1973) as

$$\frac{d\alpha}{dt} = f_1(\alpha) = (K_1 + K_2\alpha^m)(1 - \alpha)^n \tag{1.12}$$

where m and n are temperature independent constants and K_1 and K_2 are temperature dependent coefficients defined according to Arrhenius (1889) as

$$K_i = A_i e^{-\frac{E_i}{RT}} \tag{1.13}$$

where A_i is the Arrhenius factor for the chemical reaction, E_i is the molar activation energy for the reaction and R is the universal gas constant.

Furthermore, Ermanni (2007) suggested to approximate the viscosity according to Castro and Macosko (1980) as

$$\mu = f_2(\alpha, T) = Ae^{\left(\frac{B}{T}\right)} \left(\frac{\alpha_g}{\alpha_g - \alpha}\right)^{C + D\alpha} \tag{1.14}$$

where A, B, C and D are constants and α_g is the degree of cure at gelation.

Fibre Sheet Permeability   The permeability of the fibre grid is an important parameter as it has a direct effect on the flow rate and, therefore, on the equilibrium between fibre tension and tension release by resin flow. Calius, Lee and Springer included permeability as an input parameter to the fibre stress calculation in their fibre motion submodel. However, they neglected the change in permeability as a result of consolidation. Compaction during curing causes a change in FVF and therefore permeability.

Tzeng (1988) provided a more detailed explanation of the permeability of fibre sheets. It is a function of FVF and fibre dimensions. Tzeng used the Kozeny-Carman equation in Equation 1.15 to describe permeability (Carman, 1937, 1956; Kozeny, 1927):

$$S = \frac{P^3}{CS_0^2(1 - P)^2} \tag{1.15}$$

where S is the permeability of the fibre sheet, C is a constant, P is the porosity of the fibre sheet and S_0 is the specific surface area of the fibre sheet.

The specific surface area is the area exposed to the fluid per unit volume. In hydrodynamics, this is commonly referred to as the wetted area. As seen in Figure 1.13, Tzeng assumed a hexagonal packing of the fibres with a uniform fibre diameter at all locations. As seen in the sketch, the shaded areas precisely form a full circle. The same applies to the partial circumferences. The specific surface area can therefore be determined as follows:

$$S_0 = \frac{2\pi r}{\pi r^2} = \frac{4}{d} \tag{1.16}$$

The relevant flow direction is in the thickness direction. Therefore, the applicable porosity is the one perpendicular to the fibres, which can be geometrically derived as

$$P_n = \frac{T - \frac{2r}{\cos(\pi/6)}}{T} \tag{1.17}$$

where T is the distance between two fibre centres in the hexagonal packing. T is a function of the fibre volume fraction v_f and can be derived from Figure 1.13 as follows:

$$T = \sqrt{\frac{\pi r^2}{v_f \sin(\pi/3)}} \tag{1.18}$$

However, note that C is a constant that, according to Tzeng, should be found experimentally. There is no explanation of how this could be done, which limits the scientific applicability of this work.
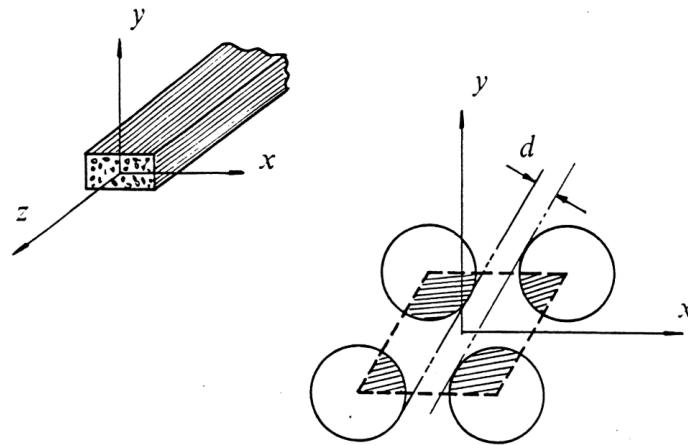
Figure 1.13: Geometric relations of an idealised hexagonal packing of fibres as a basis for the permeability model (Tzeng, 1988).

Pressure Gradient   In his finite-element approach, Tzeng determined the pressure at the nodes of each element and constructed a pressure field from this. The pressure is based on the fibre tension and the curvature of the element. Using superposition logic, a pressure gradient can be derived by superimposing the individual elements.

Lee and Springer (1990) derived the pressure difference by a force equilibrium approach of a single fibre sheet cut along the semicircle as shown in Figure 1.14. The fibre sheet has a thickness of $\Delta\xi$ and its centreline is at radius r_f. The stress in the fibre sheet at the cut lines depends on the winding angle. For simplicity, the approach of Lee and Springer (1990) is adapted by assuming $0°$ of winding angle (i.e. in circumferential direction only). Therefore the stress is just σ_f.
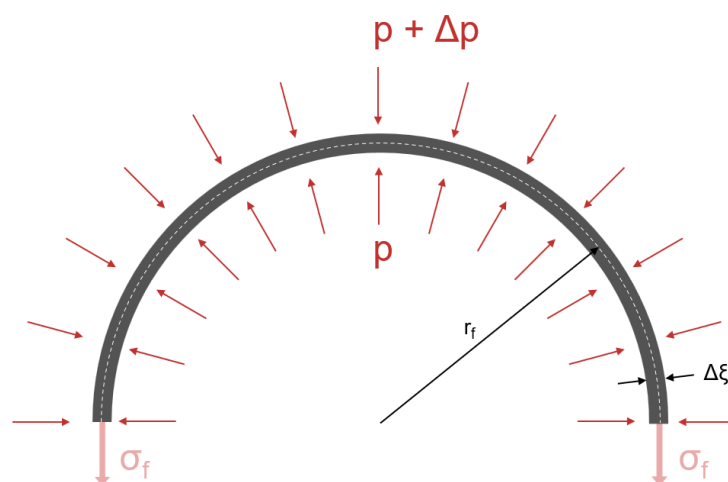
Figure 1.14: Illustration of pressures at the inner and outer surface of a fibre sheet (Adapted from Lee and Springer (1990))

Using Figure 1.14 as a free body diagram (FBD) and taking the sum of the forces in the vertical direction with positive down, one can write

$$2\sigma_f \Delta\xi \Delta z \quad + \quad 2(p + \Delta p)(r_f + \frac{\Delta\xi}{2})\Delta z \quad - \quad 2p(r_f - \frac{\Delta\xi}{2})\Delta z \quad = \quad 0 \qquad (1.19)$$

where Δz is the width of the fibre sheet along the z-axis. Assuming that the fibre sheet thickness $\Delta\xi$ is negligibly small compared to the radius r_f, the following can be stated:

$$r_f + \frac{\Delta\xi}{2} \approx r_f \qquad (1.20)$$

$$r_f - \frac{\Delta\xi}{2} \approx r_f \qquad (1.21)$$

This simplifies the force equilibrium from Equation 1.19 to

$$\frac{\Delta p}{\Delta\xi} = -\frac{\sigma_f}{r_f} \qquad (1.22)$$

The authors expressed the left-hand side of Equation 1.22 in its derivative notation to emphasise the meaning of the change in pressure per change in radial position.

$$\frac{\Delta p}{\Delta\xi} = \frac{dp}{dr} = -\frac{\sigma_f}{r_f} \qquad (1.23)$$

σ_f is simply related to the fibre tension F by A_f, which is the cross-sectional area of the fibre sheet.

$$\sigma_f = \frac{F}{A_f} \qquad (1.24)$$

From this basic approach, Lee and Springer (1990) extended further by adding additional pressures caused by the thermal expansion of the tool and the shrinkage of the resin due to its chemical changes.

Assessment and Limitations   Both Tzeng (1988) and the articles by Calius, Lee and Springer (1990) provide an excellent theoretical description of the resin flow phenomenon. Tzeng describes in detail how the necessary parameters for Darcy's equation are derived and modelled. The Calius, Lee and Springer model extends the model for thicker laminates and includes more effects for the curing model. However, it lacks detailed explanations of certain aspects, such as the lack of dependence of fibre sheet permeability on FVF. Tzeng, on the other hand, provides a detailed model of permeability but is partially relying on constants that can only be determined experimentally.

Both papers have in common that they provide purely theoretical models and lack experimental validation. Furthermore, both papers focus on the wet winding manufacturing method. However, for this master thesis, a process that mimics AFP will be investigated.

Experimental Investigations

In addition to the theoretical models of resin flow, several experimental studies have been carried out. Hahn and Lee (1992) carried out an experimental study of thick CFRP cylinders produced by wet winding. They present a test setup with pressure sensors between the mandrel and the first layer, as shown in Figure 1.15. They observed that the resin flows radially outward during winding. According to the authors, this phenomenon can also be observed for B-stage resin[7]. However, it takes much longer than uncured liquid resin due to the higher viscosity.
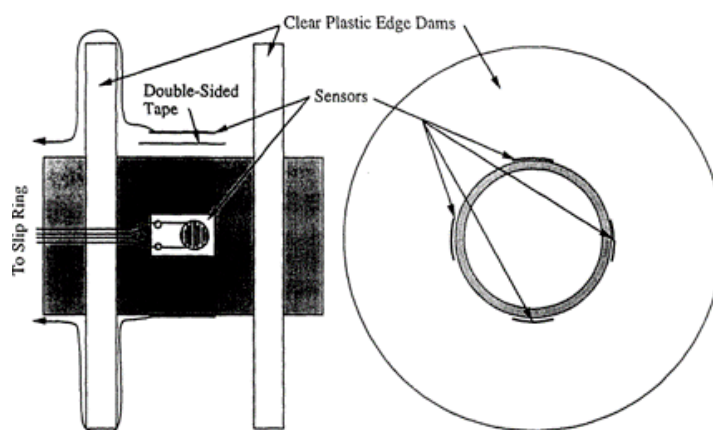
Figure 1.15: Experimental setup including sensors placed on the mandrel. The wet filament is wound around the mandrel between the dams (Hahn & Lee, 1992).

The pressure sensors are piezoelectric force sensors that allow the pressure p_f of Figure 1.7 to be measured. Each layer exerts pressure on the layers below. As the number of layers increases, so does the pressure. However, after about 6 layers, the pressure on the mandrel did not increase any further. According to the authors, the pressure of the subsequent layers is carried by compression of the inner fibres in the circumferential direction. This increases the risk of induced fibre buckling. However, Hahn and Lee were unable to demonstrate fibre buckling even with a high number of layers. The compressive stresses remained too low for fibre buckling even at higher tensile forces.

The most recent publication is a conference paper from Pérès et al. (2017). It is an experimental study to validate a process model of the wet winding process. The focus of this study is on the winding tension and the thermal expansion of the mandrel. Similarly to the test setup of Hahn and Lee (1992), piezoelectric pressure sensors were integrated between the mandrel and the laminate to measure the pressure exerted by the fibres.

Peres et al. divided the experiment into 3 phases. Figure 1.16 shows the pressure and temperature profile in the winding phase (A), the pregelation phase (B), and the post-gelation phase (C). Two samples were produced and recorded, one with 55N fibre tension and the other with 100N.

---

[7] B-stage resin: Resin in a partially cured stage (pre-preg)
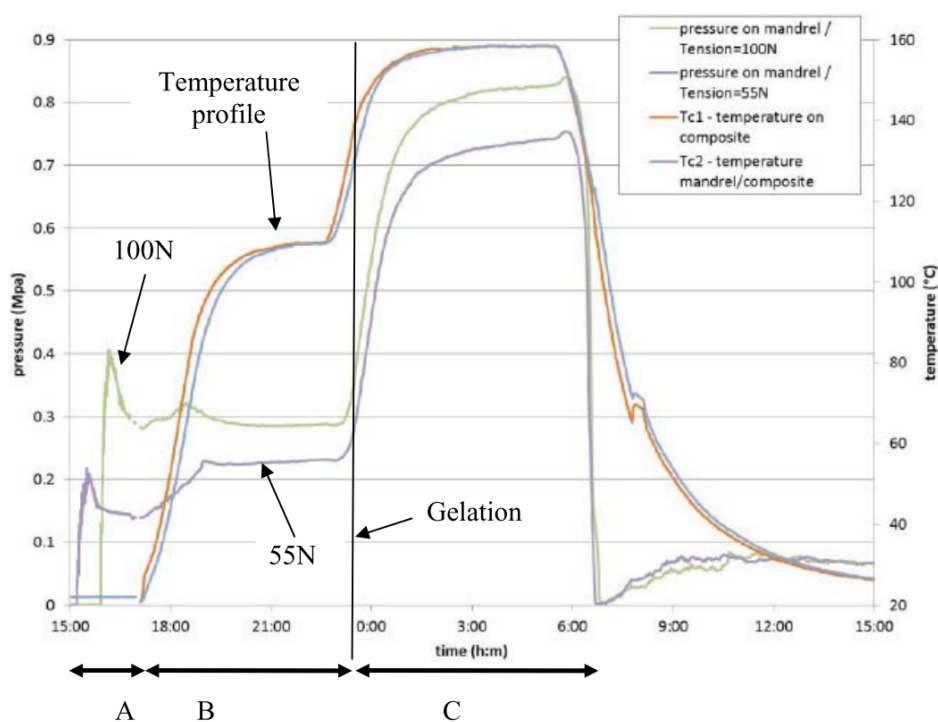
Figure 1.16: Pressure and temperature profile for two different winding tensions (55 & 100N) (Pérès et al., 2017).

Phase A - Winding Phase   During the winding phase, after a peak in the pressure build-up, a relaxation was observed. A total of 20 layers were placed. However, the peak occurred at the placement of layer 8 when winding at 55N and layer 9 when winding at 100N. Peres et al. explain this as resulting from the resin flow that starts during the ongoing winding process and release of the pressure. This explanation differs from that of Hahn and Lee (1992) who observed a constant pressure after layer 6 and suggested that the pressure was taken up by the fibres close to the core. Both considerations are logical and reasonable and likely contributed to the observed measurements.

Phase B - Pregelation Phase   Phase B is the initial heating in the autoclave, in which the composite and the mandrel are heated. Aluminium has a very positive CTE, whereas carbon fibres have a CTE close to zero or even slightly negative. This causes the mandrel to expand more than the fibres and puts the fibres under tension. At the same time, the increase in temperature causes the viscosity of the resin to decrease. Based on Darcy's law in Equation 1.3, this leads to a higher resin flow which releases the fibre tension relatively quickly. As a result, the measured pressure increase is moderate compared to the increase later in the post-gelation phase.

Phase C - Post-gelation Phase   In the second heating phase, the gelation temperature is exceeded and the pressure increases significantly. Peres et al. attribute this to the fact that the fibres are locked in the resin, preventing any further resin flow and therefore any further stress release. During the cooling phase, the pressure drops to zero as the mandrel completely detaches from the composite due to its higher CTE.

Gradient in FVF   Peres et al. prepared polished micrographs of the composite to assess the variation in FVF. The result is seen in Figure 1.17. The authors reported a range of FVF from 70% on the inside to 55% on the outside. This is considered a wide range, as manufacturers try to control the FVF in the range of ± 1 percentage points. Of course, this can vary with the requirements of each part. In all cases, the observed spread will have a significant impact on the performance of the composite. It will affect the structural performance of the material and, especially important for this research, the permeability.
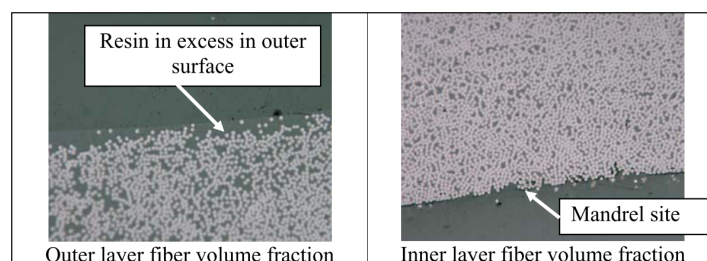
Figure 1.17: Significant spread in FVF ranging from 55% on the outside to 70% on the inside (Pérès et al., 2017).

Assessment and Limitations   The experimental studies demonstrate a simple but effective method of studying pressure variations using thin piezoelectric force sensors on the mandrel. In addition, Peres et al. provide interesting results on the variation of pressure during manufacturing and on the gradient of the FVF. However, it should be noted that Peres et al. only tested two samples in their study and winding tension was the only parameter that was changed. The same applies to Hahn and Lee, who also only varied the winding tension.

Furthermore, Peres et al. did not present the details of their manufacturing process. For example, the type of fibre and resin is unknown, the winding speed and uniformity remain unclear, and the method of measuring the winding tension is not specified. The authors were not available by email for further information.

All publications, including the theoretical ones from section 1.5.2, are tailored to a wet winding process. At the time of their publication and even today, this is the predominant method of manufacturing pressure vessels. The disadvantage of this method is an over-design of the dome areas, which can be avoided by using the AFP process. In the experimental part of the thesis at hand, an AFP process will be imitated, which is mainly characterised by a compaction roller pressing the composite layers against the mandrel. There are three main differences between AFP and wet winding:

1. **Reduced fibre tension**
   While wet winding requires a relatively high fibres tension, this is not the case for AFP, which has a considerably lower fibre tension. The selected papers are still relevant as the majority of fibre tension will be caused by the thermal expansion of the mandrel, leading to the same phenomena.

2. **Additional compaction pressure**
   The effect of the compaction pressure on the resin flow phenomenon has not yet been studied.

3. **Prepreg material instead of wet fibres**
   A prepreg material is used instead of fibres impregnated with liquid resin. The uncured B-stage resin has a much higher viscosity than the wet winding resin, which will slow

down the resin flow during the winding phase. However, the experiences from wet winding as reported in the literature are highly relevant, as the B-stage resin experiences a drop in viscosity with increasing temperature, which might lead to similar observations. The viscosity drop is likely to coincide with the thermal expansion of the mandrel, which eventually causes the resin flow phenomenon observed in wet winding.

1.6. Research Gap and Research Question

Although the selected papers are relatively old, they are still the most relevant papers for the topic of this master thesis. Apart from the publication by Pérès et al. (2017), most of the research was carried out in the 1980s and 1990s. However, new processes and technologies such as AFP open up new research gaps, making it necessary to revisit the topic of resin flow in the thickness direction of curved laminates. Overall, there are three main research gaps:

1. **Insufficient experimental validation**
   The literature review shows that the models presented by Tzeng, Lee and Springer are not sufficiently validated by experimental studies. The existing studies only vary the winding tension. This highlights the need for an experimental study with multiparameter variation, including mandrel material, fibre tension and temperature and pressure profiles of the autoclave cycle.
2. **Focus on wet winding only**
   None of the studies investigated the resin flow phenomenon in an AFP fabricated tubular specimen. Such an investigation is needed to explore whether the AFP process ultimately results in gradients in FVF that are unacceptable for cryogenic hydrogen tanks.
3. **Conclusions tailored on mechanical properties and not on permeability yet**
   The reviewed literature mainly draws conclusions about the influence of resin flow on the mechanical properties of the specimens. However, for the development of cryogenic hydrogen tanks, it is of greater interest to understand which parameters influence the gradient of the FVF and to what extent the gradient can be controlled by changing the manufacturing parameters. This will allow future research into the influence of the gradient of the FVF on the permeability of a hydrogen tank.

The research question follows from the identified research gaps. It is formulated as follows:

How do changes in manufacturing parameters affect the gradient of the fibre volume fraction along the cross-section of curved laminates?

The chosen formulation clearly frames the phenomenon to be studied, namely *the gradient of the fibre volume fraction*. It also specifies that this will be studied in *the cross-section of curved laminates* to link them with cylindrical tank structures, such as the future cryogenic hydrogen tank. It deliberately does not include any constraints that might relate to size or exact shape, in order to allow experimental study with smaller, single-curved specimens that isolate the desired phenomenon as much as possible. At the same time, the formulation leaves open the manufacturing parameters that will be studied. These had to evolve during the course of the thesis and were likely to change along the way. A specific focus is placed on *changes in manufacturing parameters* to gain an understanding of what needs to be done to control and eventually reduce the gradient.

2

Methodology

An experimental study was planned and executed to test the research question. For this experimental study, multiple tubular specimens were built, which were a simplified representation of the middle section of a hydrogen tank. The specimens differed in certain manufacturing parameters in order to provide insight into the parameters that influence the resin flow and FVF.

The chapter starts with an explanation of the methodology chosen and how it was developed in section 2.1. Then it progresses in section 2.2 with the process of making the specimens and focuses especially on how the parameters were varied during the manufacturing. It ends with section 2.3, which explains the sensors and methods used to examine specimens and materials.

2.1. Method Development & Justification

The manufacturing development for the production of cryogenic hydrogen tanks is a highly complex field with many dependencies. As illustrated in the sample pyramid in Figure 1.6, testing of the hydrogen tank is broken down into simpler test samples and specimens. By reducing complexity, knowledge gain is accelerated and results are generated more straightforwardly.

One simplification is to reduce the specimen size to a diameter of only 350mm compared to a full-scale tank with diameters of 3 - 5m. 350mm diameter is standard size for industrial tubing and therefore cost-efficient and available off-the-shelf. The reduction in size therefore reduces tooling cost and material cost for specimen manufacturing. It also speeds up the process compared to large full-size tools. The curvature of the tools is simplified to a single curvature compared to the double curvature found on the two domes of the tank. Though the double curvature introduces further challenges, at the current stage in development it is necessary to first understand the simpler geometric structures before moving on to the more complex ones. The test campaign started at the coupon level with planar coupons and evolved to the subcomponent level with single-curved specimens like the ones manufactured for this thesis, to the component level with full-scale tank models in the end. With the shape of the specimen established, the next step was to select the parameters to be varied.

Parameter Selection

Due to limited resources, decisions had to be made carefully regarding the manufacturing parameters that are varied in this study. The relevant parameters are the following:

1. Pre-preg material (thermoset materials with different viscosity profiles)
2. Mandrel material (mandrels with different CTE)
3. Stacking sequence (e.g. unidirectional, cross-ply, quasi-isotropic etc.)
4. Fibre tension
5. Compaction force
6. Material deposition speed
7. Autoclave cure cycle (temperature and pressure profile)

Number 1, the pre-preg material, is a very critical parameter as the viscosity is assumed to have a strong impact on the resin flow based on Darcy's law. Therefore, two materials were chosen, one with comparably high viscosity and one with low viscosity.

Number 2, the mandrel material, is also assumed to have a large impact on the specimens, as a higher CTE results in more fibre tension and therefore more resin flow. Aluminium and steel were therefore chosen because they are readily available metals with high and low CTEs, respectively.

Number 3, the stacking sequence, is relevant as only the circumferential hoop windings cause the resin flow. It was chosen to not include different stackings in the parametric study and to utilise only fully unidirectional stacking in the circumferential direction. This was selected to isolate and exaggerate the resin flow phenomenon to achieve clearer results. However, an additional specimen with cross-ply stacking was manufactured to have at least one data point with alternative stacking.

Number 4, the fibre tension, determines the pre-tension under which the fibres are wrapped around the mandrel. The fibre tension then drives the resin flow. As fibre tension is a parameter which can be tuned relatively easily on an AFP endefector, it was chosen to manufacture the specimens with two tension levels (high vs. low).

Number 5, the compaction force, is also a parameter which can be easily varied in an AFP endefector. However, it does not have a direct impact on the resin flow and was therefore kept constant.

Number 6, the material deposition speed, also has no direct impact on the resin flow and was kept as constant as possible.

Number 7, the autoclave cure cycle, is a crucial parameter. For each material, the manufacturer recommends a temperature and pressure profile to cure the material. However, with adapted cycles it is possible to minimise the resin flow by manipulating the temperature profiles so that fibre tension is minimised in the critical phases when the resin is able to flow. Therefore, the specimens were manufactured either with the recommended cycle or with an adapted cycle that had the goal of minimising the resin flow.

In summary, the four parameters chosen for the variation are shown in Figure 2.1 with their respective variation options.
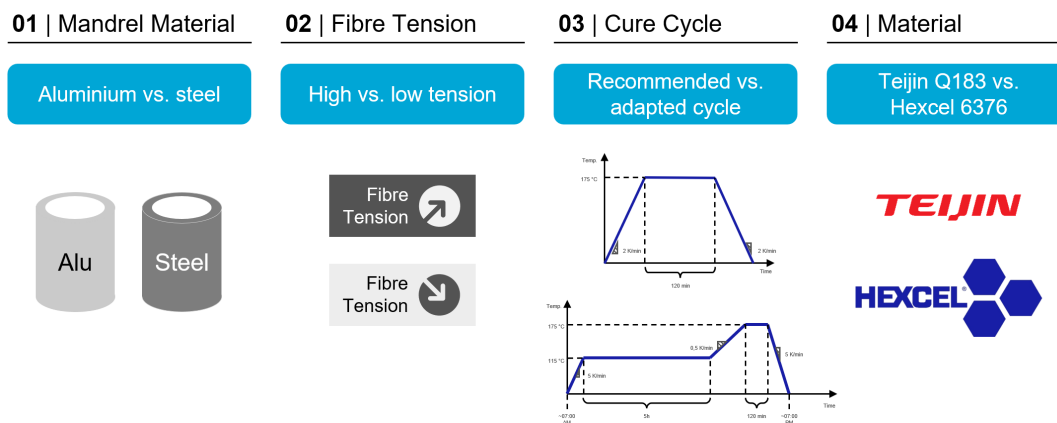
Figure 2.1: Parameters with their variation options for the manufacturing of the specimens

Test Matrix

With the variable parameters selected, a test matrix was drawn. It is found in Figure 2.2. Material from only one supplier can be cured per autoclave cycle as both materials require different cure cycles. The first cycle was performed with Teijin material in the recommended cure cycle profile and all possible combinations of mandrel material and fibre tension. Preliminary evaluation of the results revealed that the resin flow was very minor with the Teijin material. Therefore, no adapted cycle was performed which had the goal of reducing the resin flow by changing the temperature profile. Instead, for the second cycle, a special cross-ply stacked specimen and a reference specimen (equal to the first specimen in cycle 1) were cured.

In cycles 3 and 4, the Hexcel material was cured, once with the recommended cycle and once with the adapted cycle. The available material was only sufficient for 6 specimens rather than the 8 that would be needed to fill the full matrix of cycles 3 and 4. The priority was to manufacture the combinations *Aluminium* & *High Tension* as well as *Steel* & *Low Tension*, as it was expected that they represent the maximum and minimum extend of resin flow. The combination *Steel* & *High Tension* was then preferred over *Aluminium* & *Low Tension* to have more data points with a steel mandrel.
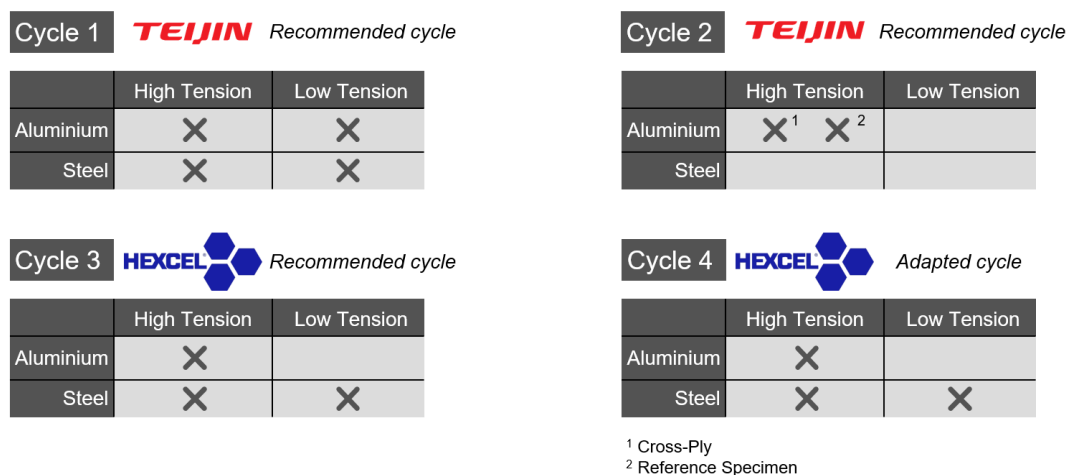
Figure 2.2: Test matrix with an overview of the chosen combinations for the manufacturing production

Material Deposition

For placing the prepreg material, different options were considered. The typical method is AFP and winding. Compared to winding, AFP is considered the most promising manufacturing technology according to the literature review of Air et al., 2023. With its abilities for tow steering and selective reinforcement by flexibly starting and ending tows at the desired places, it has the potential to overcome traditional winding techniques. However, operating the AFP robots requires specially trained personnel, and the machines availability is limited due to the high utilisation.

Due to the simple specimen geometry and CFRP layup it was possible to avoid AFP by using an alternative self-developed manufacturing rig that simplifies the process to the minimal requirements but still mimics the relevant AFP parameters and eliminates the need for an AFP machine. The top-level requirements for this manufacturing rig were as follows:

The manufacturing rig
1. shall allow for continuous placement of prepreg tapes with the fibres oriented in the circumferential direction of the mandrel.
2. shall exert a controllable and reproducible compaction force on the tapes.
3. shall generate a controllable and reproducible pre-tension in the tape.
4. shall allow for controllability over the tape placement speed.

How these requirements are fulfilled is described in the next section, which presents the design solution for the manufacturing rig.

2.2. Specimen Manufacturing

The following sections document the manufacturing process of the specimens. Section 2.2.1 presents the manufacturing rig which was specifically designed to mimic the crucial aspects of an AFP endefector. Section 2.2.2 gives an overview about the mandrels on which the specimens were produced. Section 2.2.3 introduces the specifications and properties of thermoset pre-preg material and finally, section 2.2.4 explains the cure cycles recommended by the manufacturers and the deviation of those for the adapted cycle.

2.2.1. Manufacturing Rig

The manufacturing rig had to meet the requirements listed in section 2.1. Its purpose was to provide a simple, cheap and fast setup to manufacture the specimens with varying parameters, as discussed before. The parameters had to be controllable to ensure a reproducible production process.

The parameters to be controlled were the following:
1. Compaction force
2. Tow tension
3. Material deposition speed
4. Revolutions (i.e. number of plies)

The conceptual sketch illustrating the design idea is seen in Figure 2.3. The finalised manufacturing rig follows in Figure 2.4. The designed system was based on three main phases: material supply, tensioning system and mandrel winding.
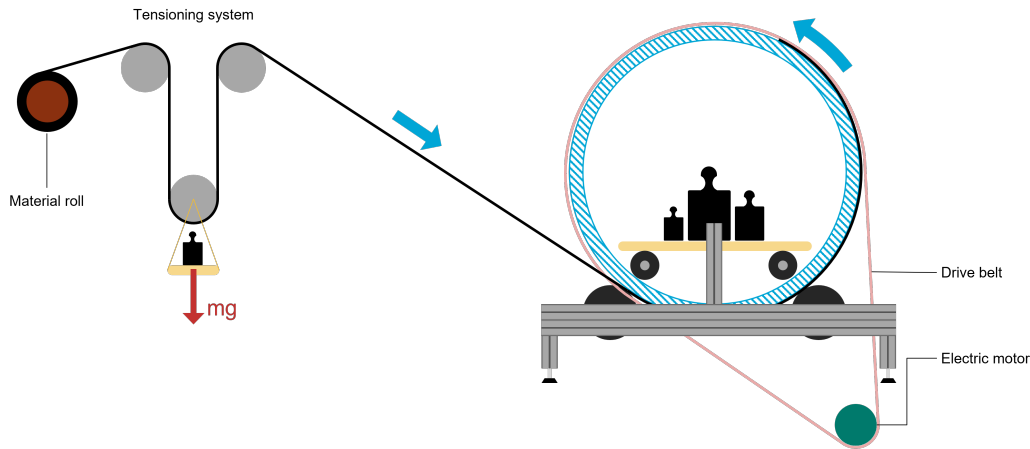
Figure 2.3: Conceptual sketch of manufacturing rig.

Material Supply   The process began on the left with the first phase - the material supply. A roll of pristine material was secured on a bar and the subsequent phases were fed with tape from this point. During specimen manufacturing, an operator held the roll with two hands and ensured that the right amount of material was fed into the upcoming tensioning unit at the desired speed.

Tensioning System   In the second phase, the tape was guided through a tensioning system consisting of three rollers. The upper two rollers were in a fixed position. The third roller hung freely in two chains in its resting position with additional lead plates mounted underneath. Once the tension on the tape increased, the tape lifted the roller from its resting position, and the weight of the roller and the lead plates were carried by the tape. In a designated vertical range of about 40cm above the resting position, the roller could move up or down without obstruction, with the whole weight carried by the tape. During the manufacturing of specimens, the operator at the material supply had to ensure that the roller remains in the desired range, as only then a constant and controlled tension in the tape is ensured. The tension could be adjusted by changing the number of lead plates underneath the roller.

Mandrel Winding   In the third phase, the pretensioned tape was wound on a mandrel that operated on two compaction rollers with a soft polyurethane coating, having a shore hardness of 50. This specific hardness was selected to closely match the standard rollers in the AFP industry. The tape was compressed between the mandrel and the compaction rollers. The compaction force resulted from the weight of the mandrel itself, plus the additional weight added to the cart that ran inside the mandrel. The entire system was driven by a stepper motor, which powered the mandrel via a belt. This configuration allowed the mandrel to pull the tape through the system while the operator controlled the material feed from the other side. An electric stepper motor was chosen over a conventional DC motor because it could provide precise control of the rotational speed, even with varying counterforce due to changes in the applied tape tension. AFP endefectors for thermoset materials have a heat source to increase

the tackiness of the tapes or tows. In this setup which is closer to a winding process no heating source is needed as the material tackiness is not relevant.
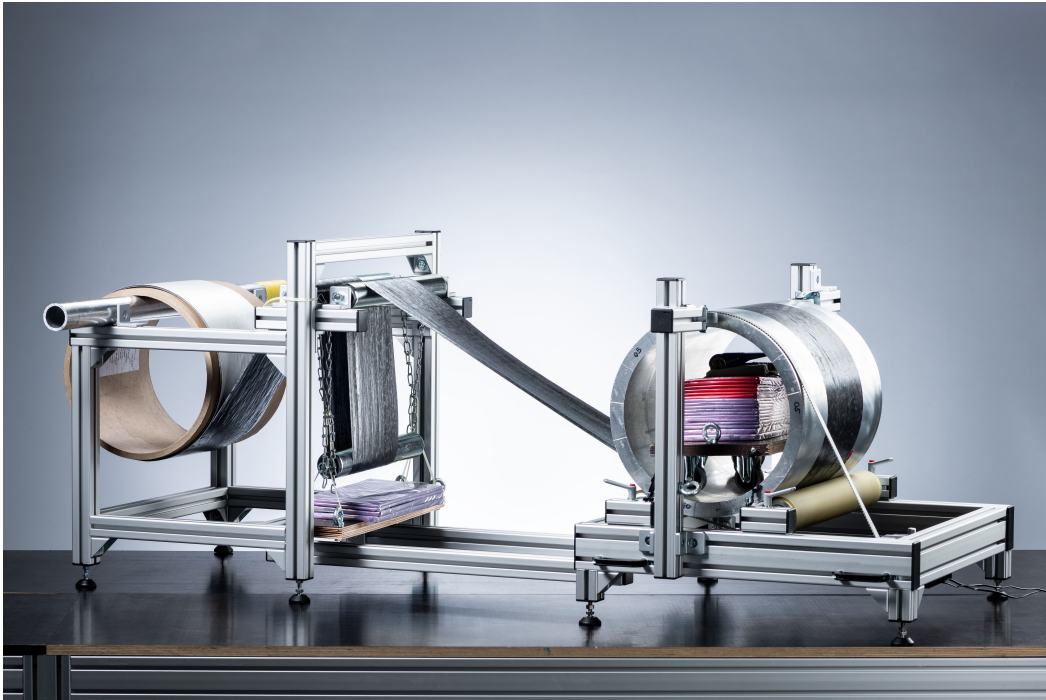
Figure 2.4: Picture of finalised manufacturing rig (DLR).

Manufacturing Parameters

In the following, the magnitudes of the winding tension and the compaction force are determined to match the width of the tape used.

Winding Tension A standard end effector used for AFP or ATL processes is depicted in Figure 2.5. It consists of a system of wheels and pulleys that guide the tow from the creel through a tension system and a tension measurement unit to the feeding rollers which are electrically driven and feed the material to the compaction roller. During the initial phase of placing a tow, the feeding rollers are required for active material feeding. Once the tack is sufficient, the feeding rollers are turned off and the tows are passively pulled off the creel actuated by the movement of the robotic arm (Bahar & Sinapius, 2020). In a study conducted by Kwik (2019) at DLR Stade, the tow tension of 0.25 inch prepreg tows was measured. The author attached the tow to a force sensor and measured the force as the end effector moved down with $2000 \frac{mm}{min}$. After a short peak at the beginning, the force settled at an average value of $2.26N$. With a $0.25inch$ wide tow, this yields a tension per width of $0.3559 \frac{N}{mm}$.
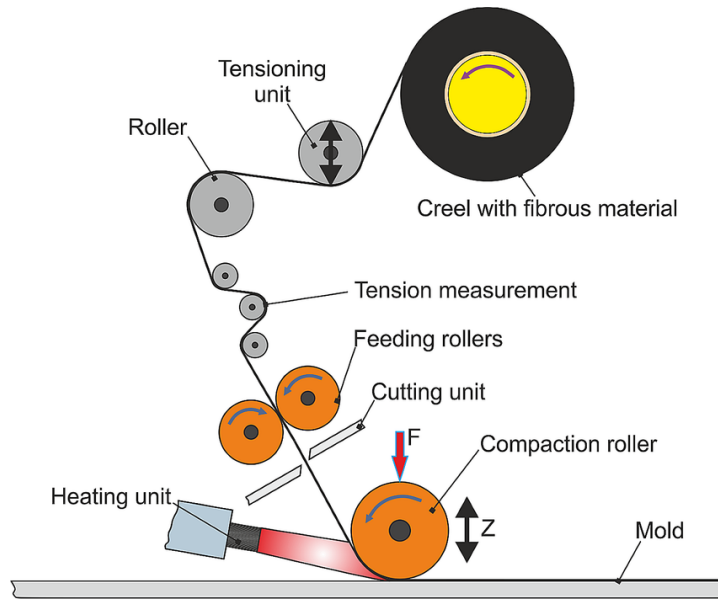
Figure 2.5: Schematic of end effector used in AFP or ATL (Arrabiyeh et al., 2024).

The manufacturing rig used in this thesis controlled the winding tension by adjusting the number of lead plates placed underneath the tensioning rollers. By visualising the forces in the free body diagram (FBD) in Figure 2.6, it became apparent that the tension on the tape equalled half of the weight pulling on the lower roller. The fibre tension was chosen in the order of typical AFP processes. The specimens produced for the thesis used tapes of width $200mm$ (when using Teijin Q183) or $200m$ (when using Hexcel 6376). Consequently, for $200mm$ a tape tension of $71.2N$ was required, or $14.5kg$ of mass was placed on the lower tensioning roller. For $100mm$, the tape tension was $35.6N$ and the required mass was $7.25kg$. The calculated tensions and masses served for the *high tension* case of the parameter variation. For the *low tension* case half of the respective tension and thus half of the mass was chosen. The mass was adjusted by placing a suitable number of lead plates on the tensioning roller.
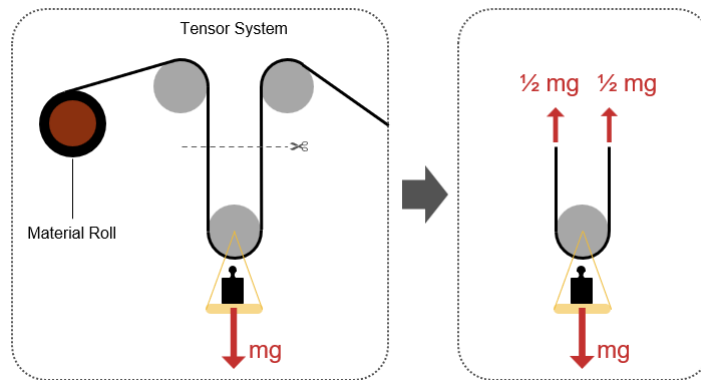
Figure 2.6: FBD indicating the forces acting in and on the tape.

Compaction Force   The internal benchmark at DLR Stade for the compaction force during AFP is to use $10N$ per $1mm$ of contact width. Published studies like the experimental study by Bakhshi and Hojjati (2020) on the reduction of defect formation in AFP processes have identified an optimal compaction force of $50lbf$ or $222.4N$ for a roller of $35mm$ width. This

is equivalent to $6.3\frac{N}{mm}$. For the manufacturing rig, the compaction force was exerted by two rollers which counteracted the weight of the mandrel from below as illustrated to the left of Figure 2.7. This deviates from the industrial standard, where only one compaction roller is used in AFP end effectors. However, it was assumed that the second compaction roller did not adversely affect the laminate quality. Instead, it improved the compaction and reduced the required compaction force as the laminate spent more time in the compaction zones of the two rollers. To determine the force on the compaction roller, an FBD was drawn, as seen to the right of Figure 2.7. In the next step, the rollers were replaced with reaction forces R_1 and R_2. Due to symmetry, their magnitude is equal.

$$R_1 = R_2 = R$$

Taking the sum of forces in y-direction yields the term for R.

$$\Sigma F_y \uparrow + \qquad 0 = 2R_y - F_g$$
$$0 = 2cos(30°)R - mg$$
$$R = \frac{mg}{2cos(30°)} \qquad (2.1)$$
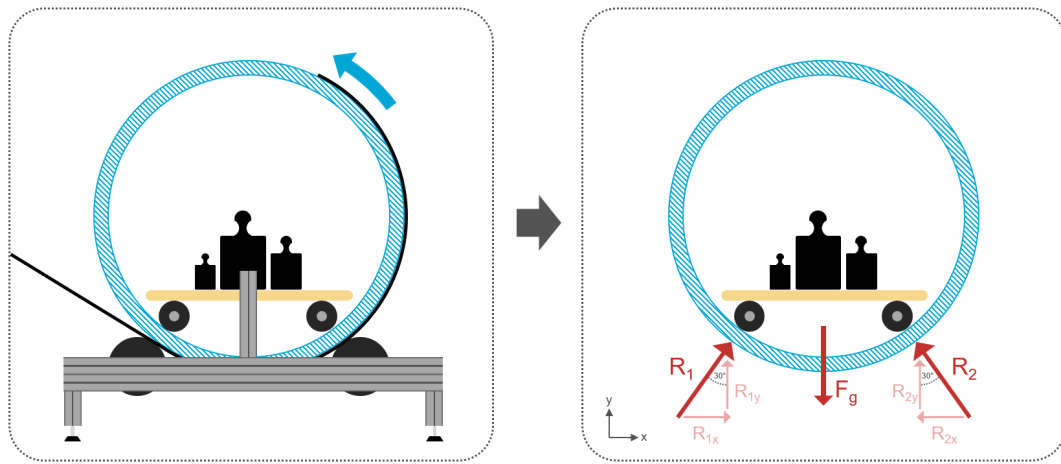
Figure 2.7: FBD with compaction rollers.

In this case, the mass m was the sum of the mass of the mandrel and the mass of the weight cart inside the mandrel. The mandrels had an empty weight of $35kg$. The maximum number of lead plates on the weight cart inside the mandrel was limited by dimensional constraints. The maximum weight therefore was $52kg$. Together with the mandrel this resulted in $87kg$. Using Equation 2.1, this resulted in a compaction force of $493N$ per roller. The compaction force scales with the contact width. Due to the fairly large width of the material of $100mm$ or $200mm$, the mandrel lifted a bit once the first layer of material passed through the compaction roller and the full weight rested only on the width of the tape. Hence, the contact width was not the full width of the mandrel but only the tape width (i.e. $100mm$ or $200mm$). Therefore, with maximum loading, a compaction force of $2.5\frac{N}{mm}$ per roller was achieved for the $200mm$ wide Teijin specimens. For the $100mm$ wide Hexcel specimens only half the weight was used to achieve the same compaction force of $2.5\frac{N}{mm}$ per roller. This remained below the internal reference value of $10\frac{N}{mm}$ or the value of $6.3\frac{N}{mm}$ in the study conducted by Bakhshi and Hojjati (2020). Nevertheless, for the purpose of this experiment the compaction force was sufficient, as the compaction took place twice because of the two rollers, and because the winding speeds were low, which resulted in an increased compaction time.

Revolutions   The number of revolutions of the mandrel determined the total number of plies and, with that, the thickness of the laminate. All specimens were manufactured with a thickness of 12 plies. This number was selected because it is very suitable for more complex stacking sequences in potential future studies, such as cross-ply, block stackings or quasi-isotropic. The following layup is an example of a typical balanced and symmetric quasi-isotropic layup with 12 plies:

$$[0/90/ + 45/ - 45/0/90]^S$$

In this way, the results of this study can be compared more easily with potential future studies.

2.2.2. Mandrels

Two different mandrel materials were available for the experimental study, aluminium and steel. Both were of hollow cylindrical shape with the same outer dimensions. Only the wall thickness differs. This was chosen from the standard dimensions available so that both mandrels approximately have the same weight. More details about the mandrels are listed in Table 2.1. In the picture in Figure 2.8, the steel mandrel is shown on the left and the aluminium mandrel on the right.

Table 2.1: Specifications of aluminium and steel mandrel.

	Aluminium	Steel
Height [mm]	450	450
Outer diameter [mm]	350	350
Wall thickness [mm]	25	10
Mass [kg]	32	36
Alloy / Type	Aluminium 6082	Steel S355
CTE [$10^{-6} \frac{m}{mK}$]	24 [Link[1]]	12 [Link[2]]
Availability	2x	2x

Figure 2.8: Picture of the steel (left) and aluminium (right) mandrel.

---

[1]   https://www.thyssenkrupp-materials.co.uk/aluminium-6082.html [Accessed: Nov. 20, 2023]
[2]   https://eurocodeapplied.com/design/en1993/steel-design-properties [Accessed: Nov. 20, 2023]

2.2.3. Material

High-quality prepreg materials with carbon fibres are expensive, and due to their relatively short shelf life of around 12 months, they are usually not in stock in high quantities. For the purpose of this thesis, Teijin sponsored a thermoset prepreg, named Q183. A second material was added later to introduce another variation of the parameters. The second material is a thermoset prepreg from Hexcel, named HexPly 6376.

The main specifications of the materials are summarised in Figure 2.9. More details can be found in the respective data sheets in Appendix E.

		TEIJIN	HEXCEL
Matrix	Name	Q183	HexPly 6376
	Curing temp.	160°C	175°C
	Holding phase	20min	120min
Fibre	Name	IMS65	Tenax HTS
	Nr. of filaments	24k	12k
	Tensile modulus	290GPa	240GPa
	Fibre volume fraction	65%	65%

IM: Intermediate Modulus   HT: High Tenacity

Figure 2.9: Material main specifications (Data retrieved from respective datasheets)

HexPly® 6376

HexPly® 6376 by Hexcel Corporation is a well-established material for primary aerospace structures that was formerly known as Fibredux 6376. It is an epoxy system based on TGMDA (tetraglycidyl methylene dianiline) with a DDS (diaminao diphenyl sulfone) curing agent. The matrix was combined with a Tenax HTS 12k fibre.

Teijin Q183

Tenax™ Prepreg Q183 by Teijin Carbon is a rapid cure prepreg system. With a curing holding time of only $20min$, it was originally designed for high-rate part manufacturing in the aerospace industry. The resin composition is subject to IP protection and cannot be disclosed, as agreed upon with Teijin. The epoxy system was combined with Tenax™ IMS65 fibres.

Cutting Process

The Teijin material was delivered as a 24" ($609.6mm$) wide tape and the Hexcel material was delivered as a $300mm$ wide tape. Both materials had to be slit into more narrow tapes to

manufacture the desired specimens. The cutting instructions are illustrated in Figure 2.10 and 2.11. Figure 2.12 shows the cutting process for the Hexcel material on the Zünd digital CNC cutter table with a drag blade at DLR Stade.
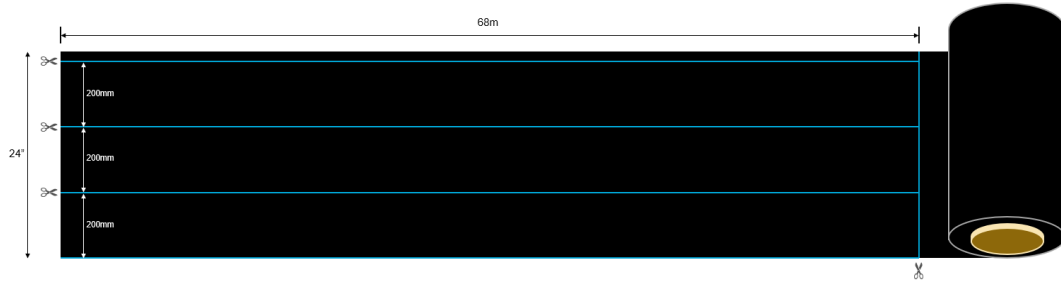
Figure 2.10: Cutting instruction Teijin Q183.
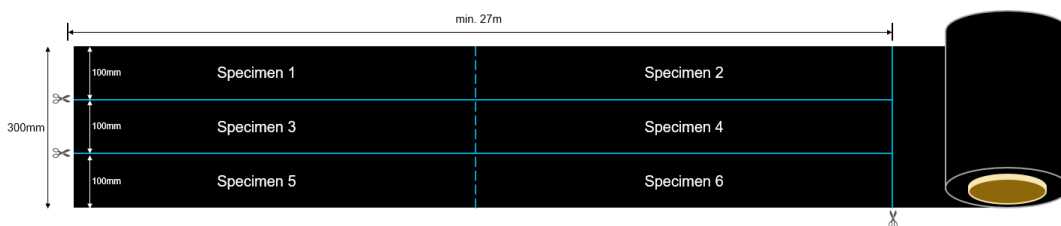
Figure 2.11: Cutting instruction Hexcel 6376.
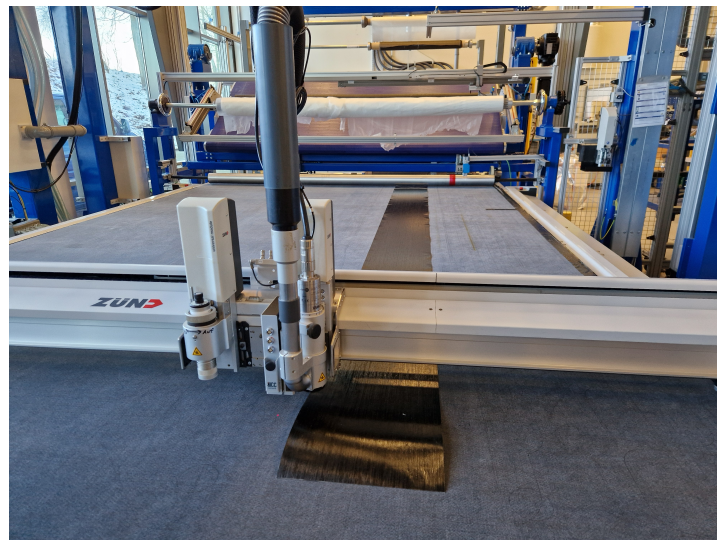
Figure 2.12: Slitting the prepreg material at the Zünd digital CNC cutter table.

2.2.4. Curing

All specimens were cured in an autoclave. However, the curing temperature of each specimen differed. While Teijin samples were cured at $160°C$ and $5bar$ pressure for only $20min$, Hexcel samples were cured at $175°C$ and $7bar$ pressure for $120min$. The curing cycles are depicted in Figure 2.13. An additional cycle, called the adapted cycle, as seen in Figure 2.14, aimed to modify the curing cycle for the Hexcel specimens such that expected resin flow would be

(a) Teijin

(b) Hexcel
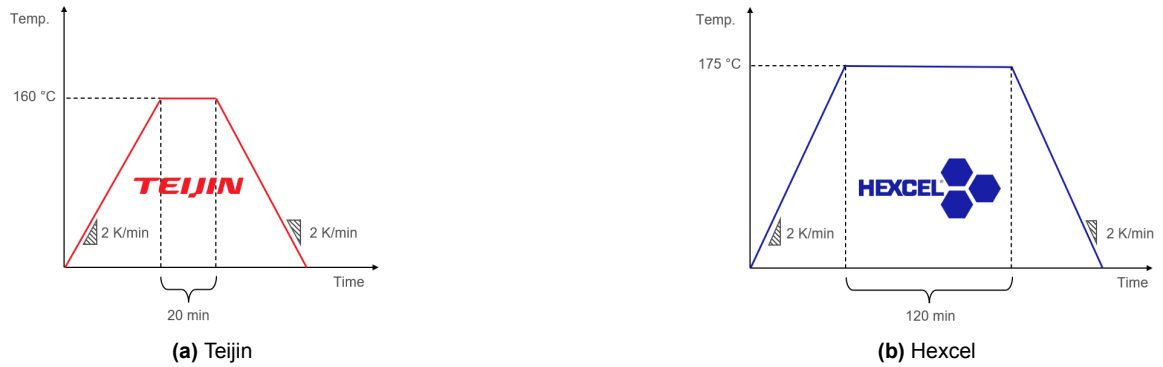
Figure 2.13: Cure cycle as recommended by the respective material supplier.

minimised. To achieve this, an additional plateau was added at a reduced temperature of $115°C$. This temperature was determined after the regular autoclave cycle with Hexcel specimens. On the basis of those results, it was possible to roughly estimate the lowest possible temperature at which the reaction kinetics were still sufficiently fast to complete the autoclave cycle within one day. The plateau at $115°C$ was maintained for $5h$, which was the maximum possible time to keep the whole cycle within the time frame of 07.00 AM to 07.00 PM. The plateau was then followed by a slow temperature increase to the regular curing temperature of $175°C$, which was maintained for $2h$ to ensure a full cure according to the data sheet. The cycle was finalised with a cool-down phase to room temperature.
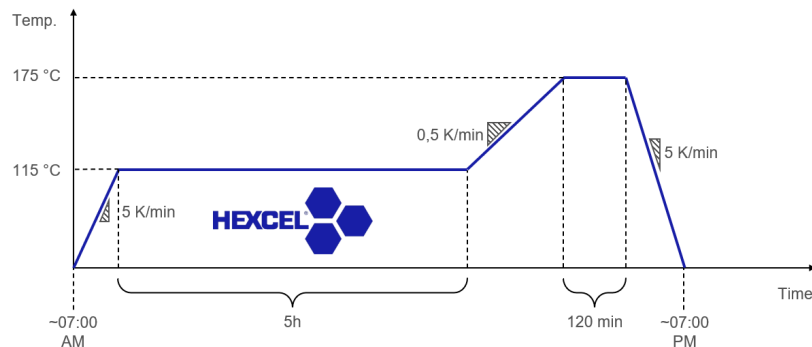
Figure 2.14: Adapted cure cycle for Hexcel material.

All specimens produced in four consecutive autoclave cycles are depicted in Figure 2.15.

Figure 2.15: Overview picture of all cured specimens (DLR).

2.3. Specimen Analysis

Various interconnected methods were used for specimen analysis. Measurements and data collection were performed on the uncured material, during the curing cycle, and after the specimen was cured. Three material characterisation techniques were applied to the uncured material, namely DSC, TMA and Rheology. This is explained in detail in Section 2.3.1. During the curing process, special pressure and temperature sensors embedded in the specimens recorded data inside the autoclave, which is further described in Sections 2.3.2 and 2.3.3. For better understanding, the autoclave loading is illustrated in Figure 2.16. After curing, small samples were cut from the specimens and embedded in resin to create micrographs under the optical microscope. Some samples were also treated with an etching solution to highlight the thermoplastic toughening particles. This is expanded on in Section 2.3.4.
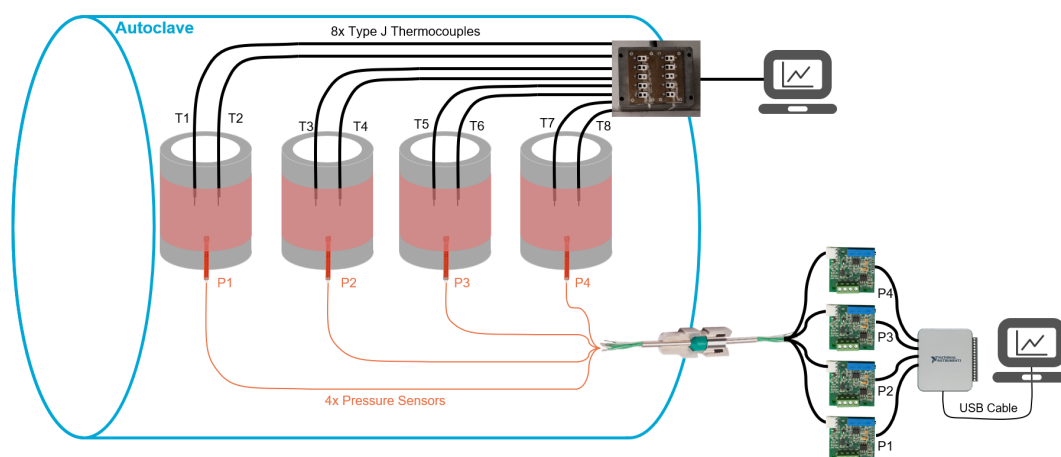
Figure 2.16: Autoclave loading with four specimens; each equipped with two thermocouples and one pressure sensor.

2.3.1. Material Characterisation

To be able to draw conclusions about the curing and flow behaviour of the two resin systems used in this study, three methods of material characterisation were performed - namely, a rheology study, differential scanning calorimetry (DSC) and thermomechanical analysis (TMA). All material characterisation methods had to be performed with the full composite, consisting of resin and fibres. The respective pure resin of the prepreg was not available for these experiments.

Rheology Study

The rheology study was performed on a rheometer by *Anton Paar*. A circle of $25mm$ diameter was cut from the uncured prepreg of both materials, Hexcel and Teijin. That sample was then put between two parallel plates. The lower plate, seen in Figure 2.17, is a bowl intended to to catch drops in the event that highly viscous materials were tested. After installation in the rheometer, the parallel plates were enclosed by a temperature-controlled oven.

Figure 2.17: Uncured Teijin sample between two parallel plates for rheology study.

During the rheology measurement, the same temperature profile was run as recommended by the manufacturer for autoclave curing (see Figure 2.13). The rheology measurement was performed in the strain-controlled mode. During the holding phase, the strain was linearly decreased to account for the stiffening of the sample due to the curing of the resin. The settings for the full cycles are shown in Figure 2.18.

(a) Teijin

(b) Hexcel

Figure 2.18: Rheometer settings for the respective material.

Differential Scanning Calorimetry

DSC was performed using the Mettler Toledo TOPEM® method, which overlays the temperature ramp with random low-amplitude temperature pulses of varying duration. This allowed a separation of the total heat flow into the reversing heat flow and the non-reversing heat flow. For measurement, a small aluminium crucible, as seen in Figure 2.19, was filled with pre-preg material, its weight recorded and the lid closed. After placing the crucible on a rotating sample holder, the machine automatically picked the sample up and inserted it into the measurement chamber (see Figure 2.20). The DSC for both materials was performed following the recommended curing cycle. However, instead of starting at room temperature, the measurement started at $-40°C$. This was done to catch the glass transition temperature of the uncured materials, which was expected to be around $0°C$ for both materials.

Figure 2.19: Teijin DSC sample in aluminium crucible before closing.

Figure 2.20: Automated sample picking in DSC machine.

Thermomechanical Analysis

During the TMA, multiple round patches of pre-preg material were stacked between two glass plates until a thickness of about 1mm was reached. The sample was then placed in a measurement instrument, as seen in Figure 2.21, which was capable of measuring changes in the thickness of the samples with high precision while the temperature varied. The temperature profile for both materials followed the recommended curing cycle. However, the Hexcel material started at $-40°C$ to capture the glass transition temperature. Note that this method does not allow conclusions about the thermal expansion of the fibres along their axis. Instead, it measures a mixture of the thermal expansion perpendicular to the fibres and the resin, which allows conclusions about the resin shrinkage due to curing.

Figure 2.21: Sample between two glass plates in TMA machine for thickness measurement.

2.3.2. Pressure Sensors

The main method for analysing the specimens was to measure the pressure at the interface between the mandrel and the laminate during the curing process. Figure 2.22 shows the slight indentation that the sensor left in its former position on a cured specimen. The pressure at that particular interface is particularly relevant as it correlates with the fibre tension, which in turn correlates with the resin flow in the thickness direction that is the subject of this study, as explained in section 1.4.
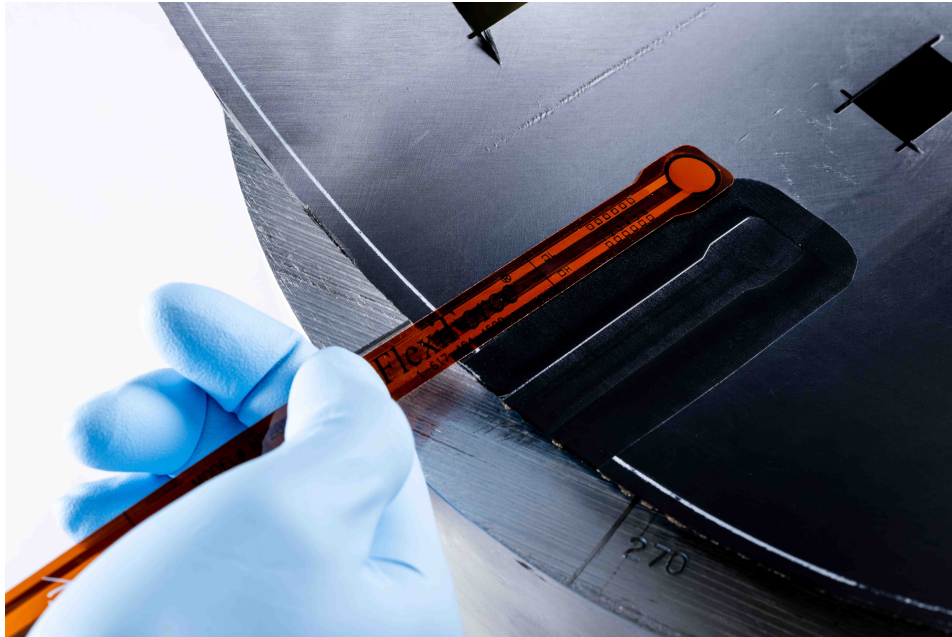
Figure 2.22: FlexiForce HT201 pressure sensor next to where it was implemented in the specimen (DLR).

During a literature study, suitable sensors able to capture pressure were identified. The main requirements for the sensor were the following:

The sensor shall
1. measure the pressure at the interface between mandrel and laminate or between adjacent plies of the laminate.
2. withstand temperatures during the curing cycle of up to $175°C$.
3. not disturb the laminate due to excess thickness or large dimensions.

The sensor chosen for this application is named *FlexiForce^TM HT201* by Tekscan^TM. It is a piezoresistive force sensor specifically designed for applications up to $200°C$. Its thickness is $0.203mm$, which is relatively thin compared to the diameter of the specimens of $350mm$. Figure 2.23 shows the sensor and the main specifications. The sensing surface is only the circular area at one end of the sensor. The metal pins on the other side are for data acquisition. The complete data sheet can be found in Appendix F.
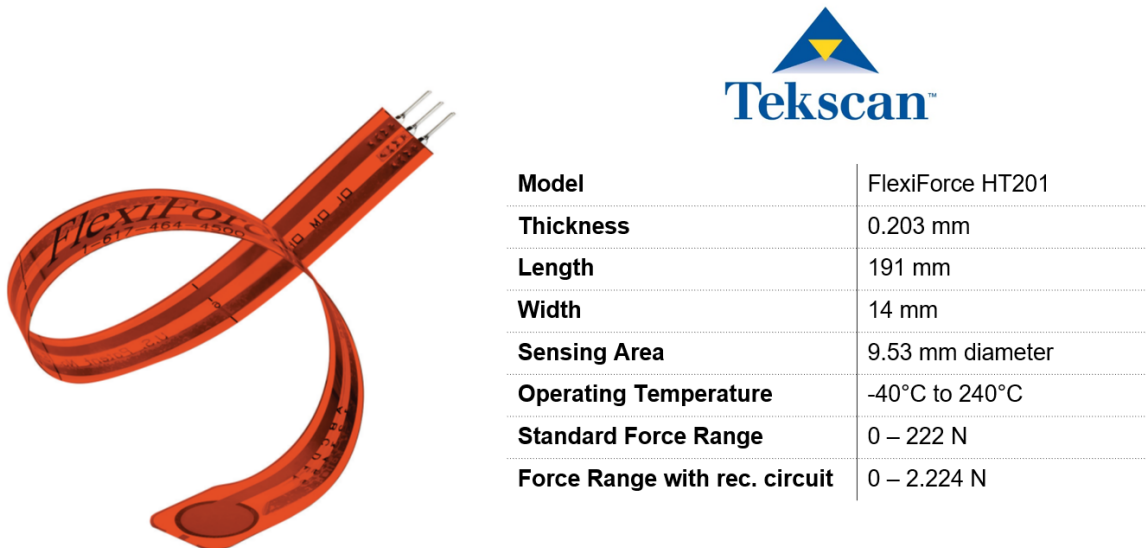
Figure 2.23: Selected specifications of pressure sensor Tekscan FlexiForce HT201 (Adapted from Tekscan).

The sensor was already implemented during the winding process of the specimen. The sensor was placed parallel to the rotation axis of the mandrel as shown in Figure 2.24 and the centre point of the circular sensing surface reached $70mm$ into the specimen for the $200mm$ Teijin specimens. The centre of the specimen (at $100mm$) could not be reached exactly since the total sensor length was too short and the metal pins would have been in the compression area of the compaction rollers. However, the sensor was placed inside the specimen such as to sufficiently avoid unwanted edge effects of the specimens. In the case of the $100mm$ wide Hexcel specimens, the sensor was placed exactly in the middle. To be able to retrieve and reuse the sensor after the curing cycle, it was protected with a thin layer of release film (Wrightlon® 5200) as seen in Figure 2.25.

Figure 2.24: Mandrel on manufacturing rig with the first ply about to be wrapped above the pressure sensor.

Figure 2.25: Pressure sensor protected by layer of release film (Wrightlon® 5200).

Sensor Signal Conditioning & Data Acquisition

To create a linear relationship between the force acting on the sensor and the output, correct signal conditioning was required. The sensor supplier published a guide for the selection of a suitable circuit (see Tekscan[3]). The two recommended circuits are an inverting Op-Amp circuit or a non-inverting Op-Amp circuit. Both ensure a linear relationship between the force and the analogue output voltage. The non-inverting circuit has a constant offset in the voltage output but only requires a single power supply. As Tekscan provided an off-the-shelf PCB (printed circuit board) with a non-inverting OpAmp circuit, this was chosen for the experimental study. The Tekscan PCB, called the Quick Start Board, is depicted in Figure 2.27. It was powered by a $9V$ block battery and was attached to the FlexiForce sensor on one side and to a voltage data acquisition device on the other. The whole system configuration is sketched out in Figure 2.27. Next to the Op-Amp, the Quick Start Board also included a voltage divider which reduced the voltage from $V_{in} = 9V$ to $V_{ref} = 0.5V$ and a low-pass filter to cut off high-frequency noise. For data acquisition of the analogue voltage output signal a *National Instruments USB-6000* was used.
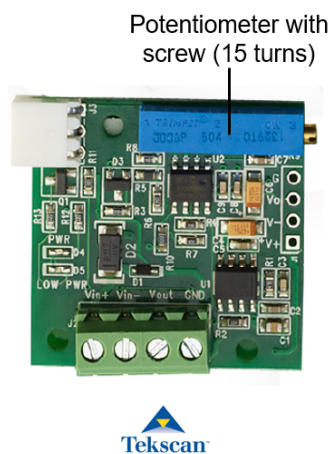
Figure 2.26: Tekscan Quick Start Board (non-inverting Op-Amp Circuit) (Tekscan[4]).

---

[3] https://www.tekscan.com/sites/default/files/FLX-Best-Practice-Electrical-Integration-RevB.pdf [Accessed: Oct. 17, 2023]

[4] https://www.tekscan.com/sites/default/files/FLX-Datasheet-QSB-RevD.pdf [Accessed: Oct. 17, 2023]

The operational amplifier amplified the voltage difference between its two inputs. The output voltage V_{out} of the Op-Amp was given by Equation 2.2 or 2.3.

$$V_{out} = V_{ref} + \frac{R_F}{R_S} V_{ref} \tag{2.2}$$

$$V_{out} = V_{ref}(1 + \frac{R_F}{R_S}) \tag{2.3}$$

V_{ref} is the non-inverting input to the Op-Amp. R_F is a variable resistance controlled by an analogue potentiometer. The setting of the potentiometer was controlled by a screw on the right side of the PCB. R_S is the resistance of the sensor, which changed with changing forces on the sensor. Without any load, the resistance of the sensor is much higher than the resistance of the potentiometer, i.e.:

$$R_S >> R_F \tag{2.4}$$

Hence, without load $\frac{R_F}{R_S}$ approaches 0 and thus $V_{out} = V_{ref}$. This is the constant offset which is typical for the non-inverting OpAmp circuit.

V_{ref} was determined by the voltage divider and follows Equation 2.5:

$$V_{ref} = \frac{R_2}{R_1 + R_2} V_{in} \tag{2.5}$$

Combining Equation 2.3 and 2.5 results in the following combined term for V_{out} in Equation 2.6:

$$V_{out} = \frac{R_2}{R_1 + R_2} V_{in}(1 + \frac{R_F}{R_S}) \tag{2.6}$$
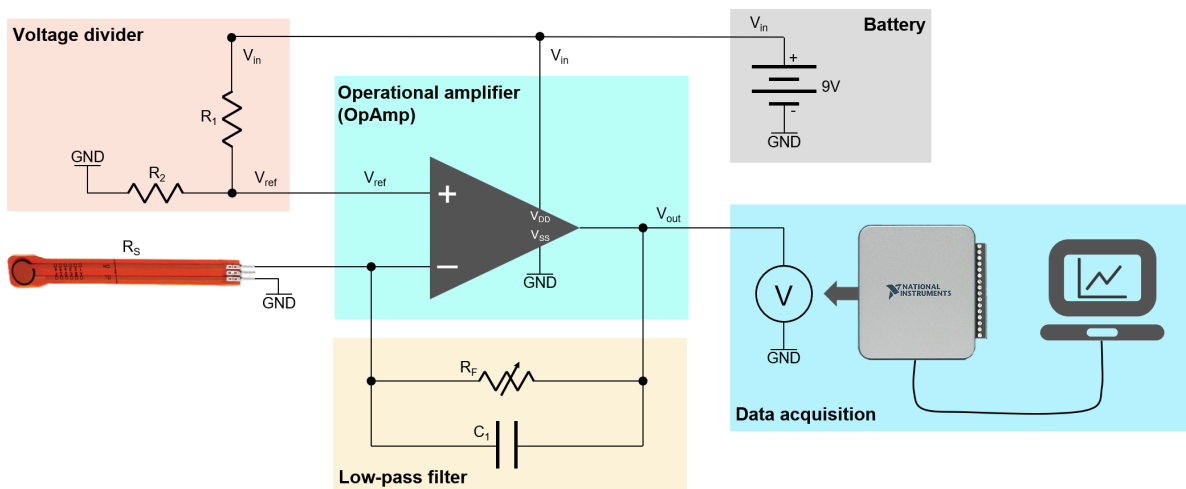
Figure 2.27: Non-inverting OpAmp circuit for signal conditioning with voltage divider, low-pass filter and data acquisition tool (Adapted from Tekscan[5]).

The measurable force range of the sensor was limited. The Quick Start Board outputs a voltage signal between $0.5V$ and $5.0V$. When the output voltage reaches the upper maximum, it remains at $5.0V$ even if the force is increased further. However, the measurable force range can be adjusted by changing the setting of the potentiometer on the Quick Start Board. This

---

[5] https://www.tekscan.com/sites/default/files/FLX-Best-Practice-Electrical-Integration-RevB.pdf [Accessed: Oct. 17, 2023]

can be done by turning the screw on the side of the PCB. In total, the screw is able to do 15 turns. The recommended procedure for calibration is to first apply the maximum expected load on the sensor and then to adjust the measurable force range by turning the potentiometer such that the maximum load is at 90% of the output range. However, the maximum expected load was unknown before the experiment. The sensor was therefore calibrated with multiple settings of the potentiometer (0, 5, 10 & 14 revolutions of the screw). During the curing cycle the output voltage was constantly monitored and kept in the measurable range by manually adjusting the screw between the pre-calibrated settings when necessary.

Sensor Calibration

As FlexiForce sensors have an inherent part-to-part variation, it is necessary to calibrate every sensor before use. For every resistance setting (i.e. 0, 5, 10 & 14 revolutions of the potentiometer), a 5-point force calibration as recommended by the manufacturer was carried out. Defined loads were placed on the sensor and the output voltage was recorded. As a representative example, the calibration of sensor 01, connected to PCB 01 with the potentiometer set on 14 revolutions is displayed in Figure 2.28. In every calibration, the load values were selected so that as much as possible of the output range of 0.5 to $5V$ was covered.

14 Revolutions		
	Load [kg]	Voltage [V]
Point 1	47	4.88
Point 2	37	4.11
Point 3	27	3.3
Point 4	17	2
Point 5	7	1.36
Load=	m	b
m*Voltage+b	10.813558	-6.846436
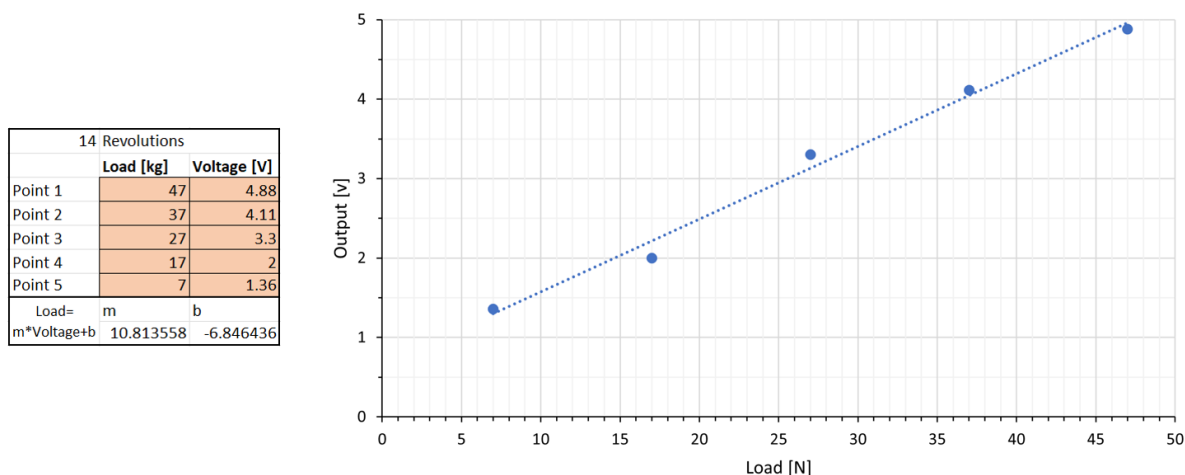
Figure 2.28: Exemplary chosen calibration curve of sensor 01 with PCB 01 at 14 rev. of the potentiometer.

To ensure that the full load is carried by the sensing area, the manufacturer recommends using a rubber puck with a surface slightly smaller than the sensing area. This puck is seen in Figure 2.29. Although this may ensure that the sensor is carrying the full load, it is still a slightly different load case compared to the intended use underneath the laminate, which fully covers the sensor and exerts a distributed load on the sensor. This limits the confidence in the quantitative values of the measurements in the autoclave. However, qualitatively the values can be compared.
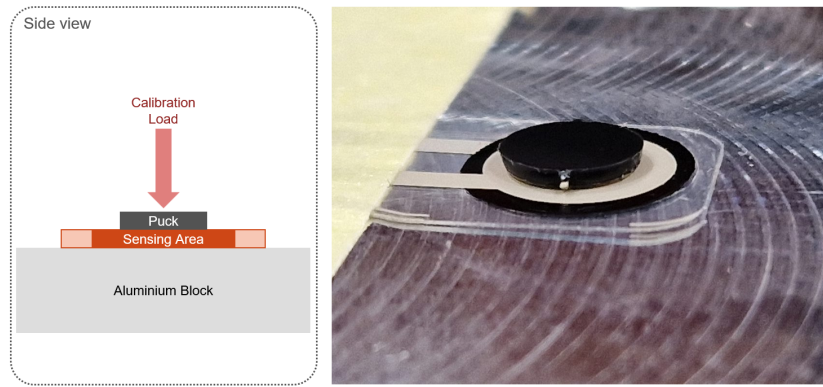
Figure 2.29: Recommended calibration procedure with a puck on the sensing area.

Calibration was performed for different potentiometer settings (0, 5, 10 & 14 revolutions). With increasing revolutions, the sensor was able to capture higher forces. In an excerpt of the calibration table shown in Figure 2.30, the calibration loads can be seen.

		14 Revolutions				**10 Revolutions**				**5 Revolutions**				**0 Revolutions**	
		Load [kg]	Voltage [V]			Load [kg]	Voltage [V]			Load [kg]	Voltage [V]			Load [kg]	Voltage [V]
Sensor 01	Point 1	47	4.88	Point 1		8	4.8	Point 1		3	4.1	Point 1		2.5	4.38
	Point 2	37	4.11	Point 2		6.5	3.8	Point 2		2.5	3.22	Point 2		2	4.05
	Point 3	27	3.3	Point 3		5	3.23	Point 3		1.7	2.58	Point 3		1.5	2.92
PCB 01	Point 4	17	2	Point 4		3	2.02	Point 4		1.2	2.16	Point 4		1	2.51
	Point 5	7	1.36	Point 5		1.5	1.31	Point 5		0.6	1.22	Point 5		0.5	1.26
	Load=	m	b	Load=		m	b	Load=		m	b	Load=		m	b
	m*Voltage+b	10.813558	-6.846436	m*Voltage+b		1.8732535	-0.879705	m*Voltage+b		0.8810461	-0.540058	m*Voltage+b		0.6196122	-0.373707
		14 Revolutions				**10 Revolutions**				**5 Revolutions**				**0 Revolutions**	
		Load [kg]	Voltage [V]			Load [kg]	Voltage [V]			Load [kg]	Voltage [V]			Load [kg]	Voltage [V]
Sensor 02	Point 1	56	4.9	Point 1		6	4.6	Point 1		2.5	4.5	Point 1		2	4.4
	Point 2	45	4.3	Point 2		5	4.2	Point 2		2	3.78	Point 2		1.6	3.8
	Point 3	34	3.73	Point 3		4	3.6	Point 3		1.5	3.45	Point 3		1.2	3.38
PCB 02	Point 4	22	2.65	Point 4		3	3.05	Point 4		1	2.5	Point 4		0.8	2.45
	Point 5	11	1.73	Point 5		2	2.2	Point 5		0.5	1.8	Point 5		0.4	2.1
	Load=	m	b	Load=		m	b	Load=		m	b	Load=		m	b
	m*Voltage+b	13.910612	-14.55854	m*Voltage+b		1.6536965	-1.837549	m*Voltage+b		0.7358903	-0.859264	m*Voltage+b		0.6608321	-0.931844

Figure 2.30: Excerpt from calibration data with applied load and recorded voltage signal.

For revolutions 0, 5 and 10 it was possible to calibrate with standard calibration weights of up to $10kg$ as seen in Figure 2.31. For revolution 14, the weights were not heavy enough. As a hydraulic press was not available for the calibration, a different and more unconventional method was chosen. A pallet truck with an inbuilt weight scale was driven under a heavy and rigid structure. With the sensor placed on top, the pallet truck was then lifted until the sensor with the puck was pressed against the rigid structure, as seen in Figure 2.32. The load on the sensor could be read off the weight scale. With the hydraulic lifting mechanism of the pallet truck, the load was controlled and calibration was performed. Before this procedure, the accuracy of the weight scale was tested and gauged as more than sufficient for the desired force range.

Figure 2.31: Calibration weights for low weight sensor calibration spectrum.

Figure 2.32: Improvised sensor calibration with pallet truck for high weight spectrum. The measurement accuracy is sufficient for the use case.

Autoclave Cable Feed-through

The Quick Start Board and data acquisition tool were not resistant to heat and therefore could not be placed inside the autoclave. Only the sensor was positioned inside the autoclave, with wires routed out to the Quick Start Board. Due to the high pressure conditions inside the autoclave, the cables necessitated a feed-through assembly that ensured a leak-proof passage through the autoclave shell. Since DLR Stade did not have a feed-through for copper cables, one had to be acquired. Three various options, shown in Figure 2.33, were considered. Given that the autoclave was filled with nitrogen gas, it was crucial for safety to ensure a leak-tight seal. Therefore, option 03 was selected because of its guaranteed leak tightness and its reusability for future autoclave studies. Typically, this feed-through supports 24 wires, where the type can be chosen as needed. For the FlexiForce sensors, only eight copper wires were technically required. The chosen feed-through was ordered with 12 copper wires and 12 thermocouple type K cables to accommodate future experimental needs. Throughout all autoclave cycles, the feed-through assembly performed as expected, with no leakage occurring.

	01	02	03
Type of feed-through assembly	3 touching cables	4 individually shielded cables	24 freely selectable wires
Reusability	Temporary assembly | Rubber seal broken after disassembling	Temporary assembly | Rubber seal broken after disassembling	Cables remain in feed-through and can be reused
Assembly	Assembly at DLR	Assembly at DLR	Assembly by supplier
Leak tightness	Not leak tight, according to supplier	Most likely leak tight but no guarantee by supplier	Leak tightness guaranteed by supplier
Heat resistance	Up to 870°C	Up to 870°C	Depends on the implemented cables
Price	No quote provided	105 €	778 €
Lead time	Metal hull on stock, new seal 2-3 weeks	2-3 weeks	2-3 weeks

Figure 2.33: Comparison of three possible solutions for an autoclave cable feed-through.

2.3.3. Temperature Measurement

In order to draw conclusions about the thermal expansion and the curing progress of the prepreg material, it was crucial to know the temperature of the laminate and the tool. Therefore, two thermocouples of type J were inserted in each specimen. One was placed between the laminate and the tool, and the other one was placed on top of the laminate but underneath the vacuum layers. As the thermocouples were relatively thick, they could not be placed underneath the actual laminate. This would cause problems during the winding process as it would introduce unwanted wrinkles. To solve this, a traveller specimen was added to the mandrel. This consisted of small square prepreg patches which were hand-layed on the mandrel with the same lay-up as the actual specimen to ensure equal properties. The thermocouples were then placed underneath and on top of the traveller specimen. In Figure 2.34, above the actual specimen, the traveller specimen with its thermocouples can be seen.

Figure 2.34: Mandrel with quadratic traveller specimen and thermocouples. The large cylindrical specimen on the mandrel was sourced from a different experimental study but was manufactured the same as the specimens for this thesis (DLR).

2.3.4. Micrographs for Optical Microscopy

The specimen analysis continued with an investigation of the laminate cross-section by creating micrographs from the specimens for optical microscopy. During this process, two samples were extracted per specimen. The samples were cut in such a way that the fibres were orientated normally to the observation surface. Using a custom 3D printed holder in an embedding

mould, the samples were strung together and kept in an upright position with the observation surface facing down, as seen in Figure 2.35. The mould was then filled with a transparent 2-component epoxy resin. After curing, the mould was removed and the embedded samples were ground and polished, as seen in Figure 2.36. The finished micrographs in Figure 2.37 are shown ready for optical microscopy.

Figure 2.35: Micrograph clamped in custom 3D printed holders inside embedding moulds.
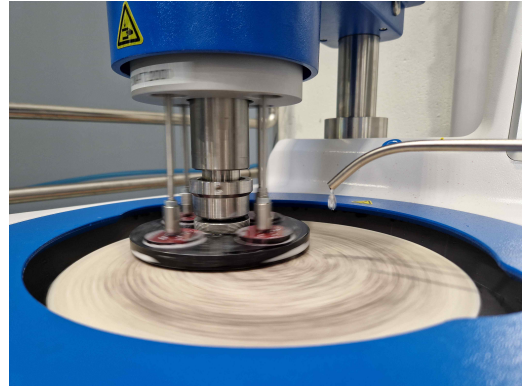
Figure 2.36: Grinding and polishing process of micrographs.

Figure 2.37: Micrographs after polishing.

Figure 2.38: Micrograph under microscope (DLR).

The microscopic images were taken by the microscope *VHX 5000* by *Keyence* at a magnification of 500x and with a 2D stitching procedure including automatic depth composition. This procedure automatically takes multiple pictures in a predefined section and stitches them together to a larger high-resolution image.

NMP Etching

To gain deeper insight into the resin composition, some micrographs were treated with N-Methyl-2-Pyrrolidon (NMP), which makes thermoplastic toughening particles visible by selectively etching them on the surface of the micrograph. Following the procedure described by Farooq et al. (2023), a small amount of NMP was applied to the micrographs as seen in Figure 2.39 and then rinsed with ethanol. New pictures were taken under an optical microscope to compare the before and after states.

(a) N-Methyl-2-Pyrrolidon (NMP) (left) and ethanol (right).
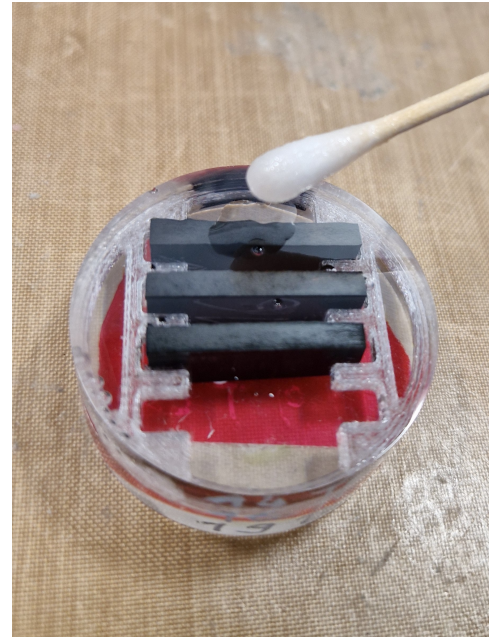
(b) NMP is applied on micrograph and then rinsed with ethanol.

Figure 2.39: NMP etching process.

Heat-Map Generation

To be able to make objective statements about the resin distribution and the local FVF, an algorithm was developed together with Jonas Naumann, a master's thesis student at TU Braunschweig, Germany and DLR Stade. In his master's thesis, Naumann (2024) developed a machine learning-based segmentation algorithm able to classify digital images of CFRP micrographs pixel by pixel. The algorithm was specifically trained to help researchers find microcracks. In addition to the microcracks being one class, the algorithm distinguishes between resin and fibres of different orientations (e.g. $0°$, $45°$ or $90°$). This was used to calculate the local FVF and plot it as a heat-map as seen in Figure 2.40.

With the segmentation data available for every pixel, the FVF could be calculated by assuming that the local FVF of area A was simply given by the ratio of the number of pixels in A attributed to fibres divided by the number of pixels in A attributed to resin:

$$\text{FVF}_A = \frac{\text{pixels of class fibre in A}}{\text{pixels of class resin in A}} \tag{2.7}$$
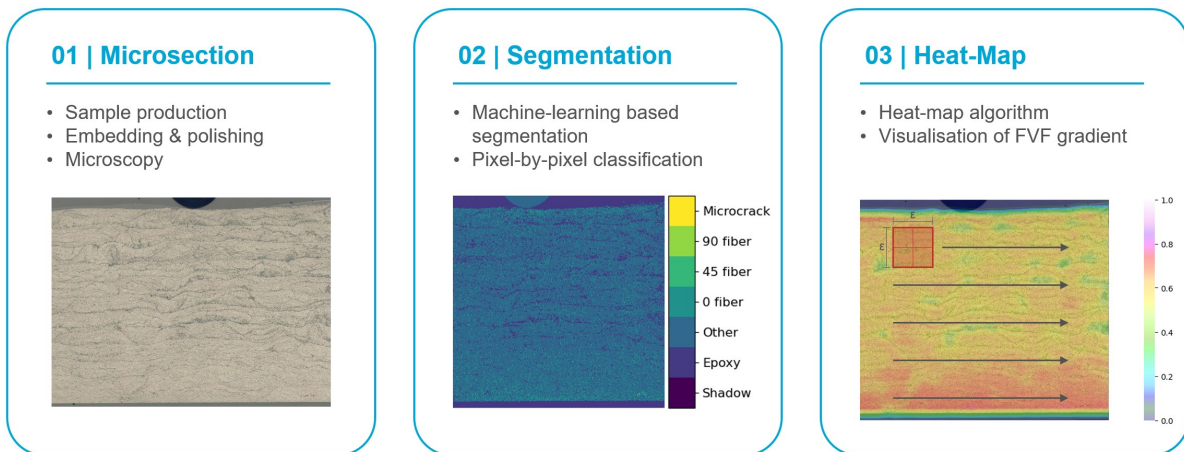
Figure 2.40: Process of generating heat-maps of local FVF.

In Figure 2.41, area A is presented by the red square with edge length ϵ. The algorithm calculated the local FVF of A and saved the result only for the pixel right at the centre point of the square. The square then translated across the whole image to calculate the FVF of every pixel based on its close surrounding. In the shown example $\epsilon = 200px$, the data produced was then used to plot it as a heat-map. For better visualisation, the heat-map is slightly transparent so that the real micrograph can be seen in the background.
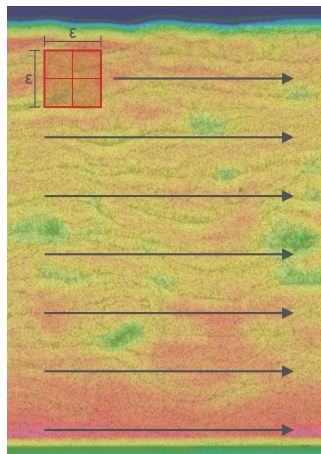
Figure 2.41: Exemplary movement path of small square to determine local FVF.

An inherent flaw of this methodology can be observed at the upper and lower boundary of the CFRP sample, where the FVF seems to drop rapidly. When calculating the FVF of pixels close to the boundary, the square of area A reached beyond the boundary where fibres were not present anymore as the sample had stopped. This was included in the calculation and falsely decreases the FVF. However, the remainder of the micrograph was correctly calculated and plotted.

3

Results

In total, 12 specimens were manufactured in accordance with the test matrix, shown earlier in Figure 2.2. The infrastrucuture developed for this study was also used to produce specimens for a parallel study, investigating the influence of other manufacturing-induced anomalies such as gaps. Looking at Figure 3.1, all lines filled with parameters are specimens produced for the thesis at hand. The remaining empty lines are placeholders for the specimens from the gap-study or empty mandrels which were placed in the autoclave as a wind shield to achieve a uniform temperature among the samples regardless of their position in the autoclave.

Specimen No.	Mandrel	Fibre Tension	Cycle	Material	Notes
01	Steel	High	1	TEIJIN	
02	Aluminium	High			
03	Aluminium	Low			
04	Steel	Low	Teijin recommended		
05					Empty (Wind shield)
06					
07			2	TEIJIN	
08	Aluminium	High			Reference Specimen
09					
10			Teijin recommended		Empty (Wind shield)
11	Aluminium	High			Cross-ply | Minor Leakage in vacuum foil
12					
13	Steel	High	3	HEXCEL	Leakage in vacuum foil
14	Aluminium	High			Vacuum foil bursted at 01:22
15					
16	Steel	Low	Hexcel recommended		
17					Empty (Wind shield)
18					
19	Steel	High	4	HEXCEL	Vacuum foil bursted at 08:24
20	Aluminium	High			Leakage in vacuum foil
21					
22	Steel	Low	Hexcel adapted		
23					Empty (Wind shield)
24					

Figure 3.1: Overview of produced specimens with their respective parameter settings. Lines without parameters are placeholders for a different study.

As explained in the methodology, the data were recorded in multiple instances before, during, and after the specimen production process. The pristine and uncured material was used for material characterisation to gain deeper insights into the resin rheology and curing behaviour. The results of those tests are found in section 3.1. The temperature and pressure sensors recorded data during the curing process. The results are presented in section 3.2. After the specimens were fully cured, micrographs were created and evaluated, as seen in section 3.3.

3.1. Material Characterisation

The results of the three applied material characterisation methods, rheology study, DSC and TMA, are presented below. Note that the Teijin Q183 material was provided on the condition that no data directly related to the material which is not already covered by the publicly available data sheets may be published here. Publication of the results of the material characterisation would be in contravention of this. Therefore, these results are kept in a confidential appendix (see Appendix A) and are not available in the freely accessible version of this thesis.

3.1.1. Rheology Study

The rheology study was performed with the same temperature profiles as recommended for autoclave curing of the respective material. During the heat up phase, the temperature increased linearly at $2\frac{K}{min}$ and was then kept constant at the respective cure temperature of $160°C$ for Teijin Q183 and $175°C$ for Hexcel 6376. In Figure A.1 the rheological moduli for Teijin Q183 are plotted against the temperature. Before reaching the temperature plateau, a strong increase in the storage modulus can already be observed. This is the gelation point. However, in plotting the same graph for Hexcel 6376 in Figure 3.2, such an increase in the storage modulus is not observed. This is because the plot only covers the first temperature ramp and not the holding plateau. When plotting the data on a time scale that extends further and includes the holding plateau as seen in Figure 3.3, it is concluded that gelation occurs during the holding phase at $175°C$.
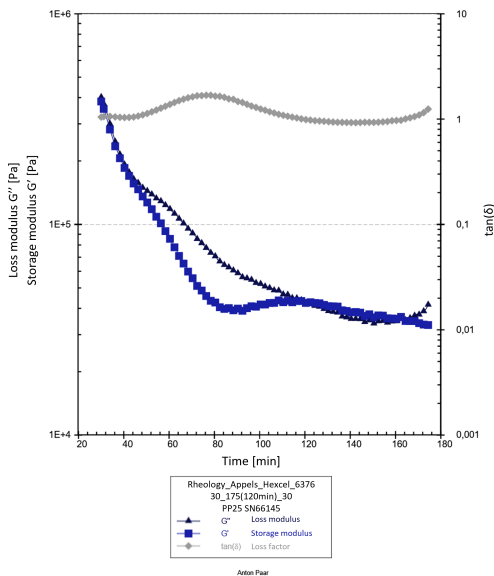
Figure 3.2: Storage and loss modulus plotted against temperature for Hexcel 6376.
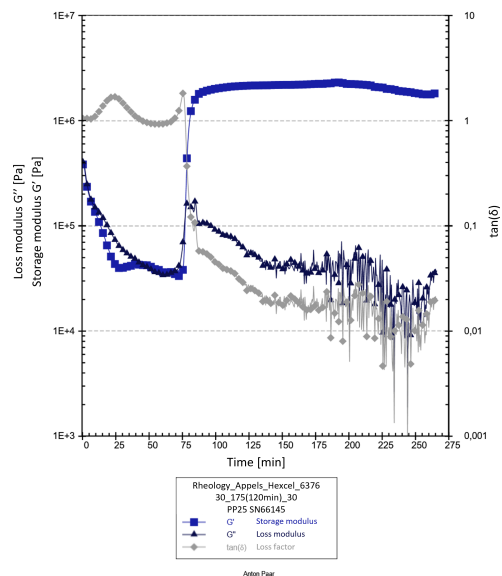
Figure 3.3: Storage and loss modulus plotted against time for Hexcel 6376.

The software of the rheometer also calculates the complex viscosity. Plotting the complex viscosity for both materials together with their respective temperature curves in one graph yields Figure A.2. The Hexcel material reached gelation after $76min$, which is shortly after entering the $175°C$ holding plateau. Teijin reached gelation already during its heat up ramp. When comparing the two materials, it should be noted that the test had to be performed with the fibres, as a separation of resin and fibre was not possible, and with different sample thicknesses, as the prepreg had different ply thicknesses. This had a strong impact on the absolute values as a result of the superior stiffness of the fibres compared to that of the resin. However, the qualitative trends remain correct. For instance, in this measurement the minimum viscosity of Teijin is lower than the one of Hexcel. When comparing it with the viscosity data provided by the manufacturers in the respective data sheets, Hexcel 6376 has an overall lower viscosity than Teijin Q183. Due to the aforementioned reasons, the manufacturer's data is more reliable in this case.

3.1.2. Differential Scanning Calorimetry

The DSC measurements with the temperature modulated method called TOPEM[®] are found in Figure 3.4 for Hexcel 6376 and in Figure A.3 for Teijin Q183. The upper half of each figure shows two lines. The black line is the nonreversible heat flow that includes the exothermic curing behaviour of the resin. The brown line is the reversible heat flow showing effects like the glass transitions or changes in the heating ramp. The lower half of the respective figures shows the heat capacity curve. The DSC measurements started at $-40°C$ and heated with $2\frac{K}{min}$ up to the recommended cure temperatures of $160°C$ with a $20min$ plateau for Teijin Q183 or $175°C$ with a $120min$ plateau for Hexcel 6376. The following cooling phase with $-10\frac{K}{min}$ down to $0°C$ was accelerated compared to the recommendation, as no new insights were expected from this phase after the material has already been fully cured. The material was then heated again by $2\frac{K}{min}$ to $220°C$ to determine the glass transition temperature of the cured material.
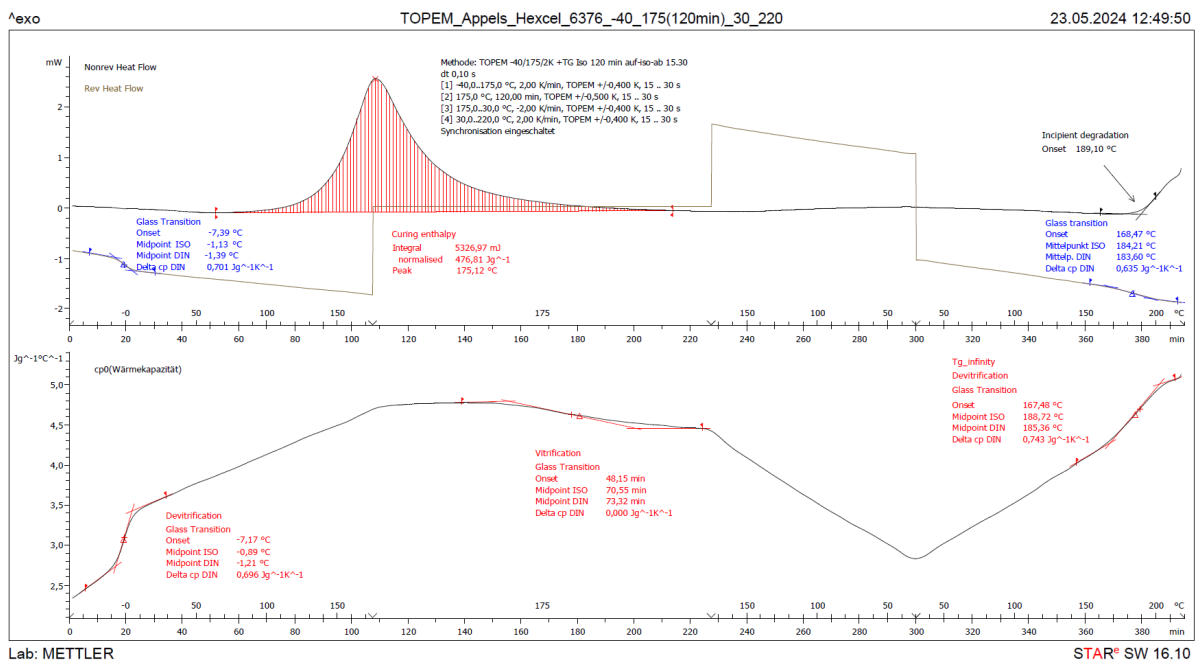
Figure 3.4: DSC measurement of Hexcel 6376. Temperature Modulation with TOPEM[®].

3.1.3. Thermomechanical Analysis

The TMA measurements are found in Figure 3.5 for Hexcel 6376 and in Figure A.4 for Teijin Q183. The measurement of Hexcel 6376 starts again at $-40°C$ to capture the glass transition. The measurement of Teijin Q183 starts at room temperature, as the machine was only available for a limited period of time.
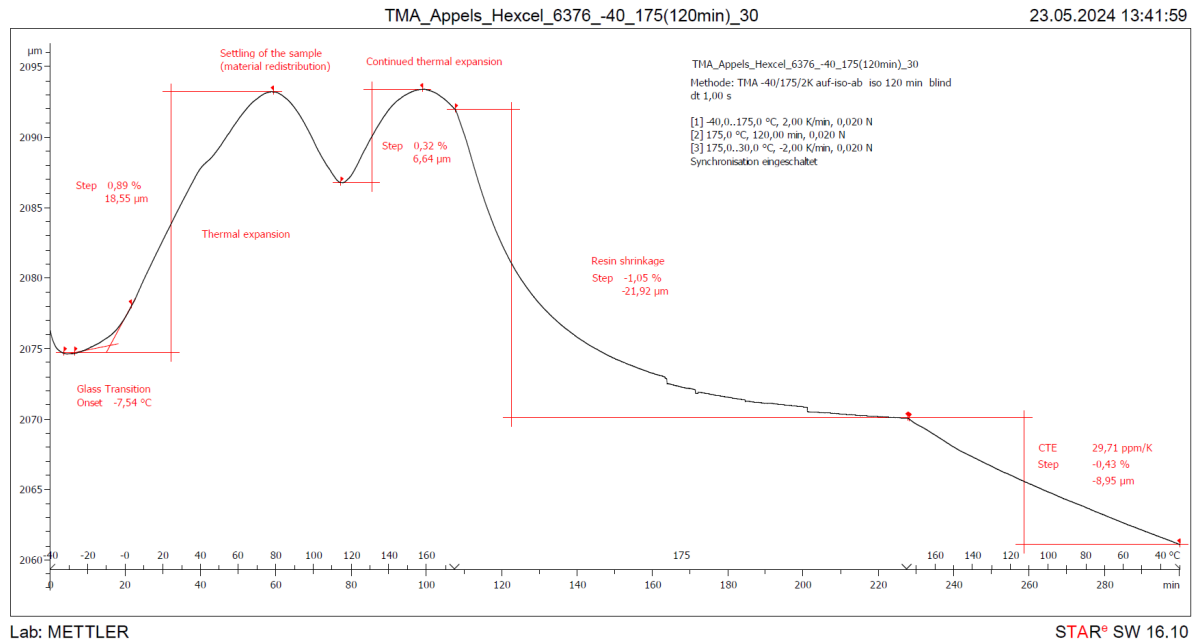
Figure 3.5: TMA of Hexcel 6376.

3.2. Pressure and Temperature Graphs

The temperature data from the two implemented thermocouples and the readings of the pressure sensor are plotted in one graph against the time. As an example, specimen 14 is displayed in Figure 3.6. Each pressure and temperature graph has the chosen manufacturing parameters in the top right corner and a note in the top left corner to document possible unexpected incidents. For specimen 14, for example, the vacuum foil burst. However, the impact on the specimen was limited as curing had progressed sufficiently by the time the burst occurred.

Temperature (bottom) refers to the thermocouple embedded between the laminate of the traveller specimen and the mandrel. *Temperature (top)* refers to the thermocouple on top of the laminate. The nomenclature of the pressure sensors follows the same logic. *Bottom* refers to an implementation between mandrel and laminate. *Top* is a sensor on top of the laminate and *Middle* refers to a sensor embedded between ply 6 and 7 of a total of 12 plies. All specimens had two thermocouples and a bottom pressure sensor implemented. Some selected specimens also had pressure sensors implemented in the middle and top positions.

The pressure sensors were calibrated with a defined force acting through a puck on the sensor sensing area, as explained in subsection 2.3.2. The loading case underneath the laminate without the puck is different and more spread out, which distorts the absolute values when transforming them to pressure values. For this reason, the y-axis has force as a physical

quantity and not pressure. However, for the qualitative interpretation of the results, this is irrelevant.
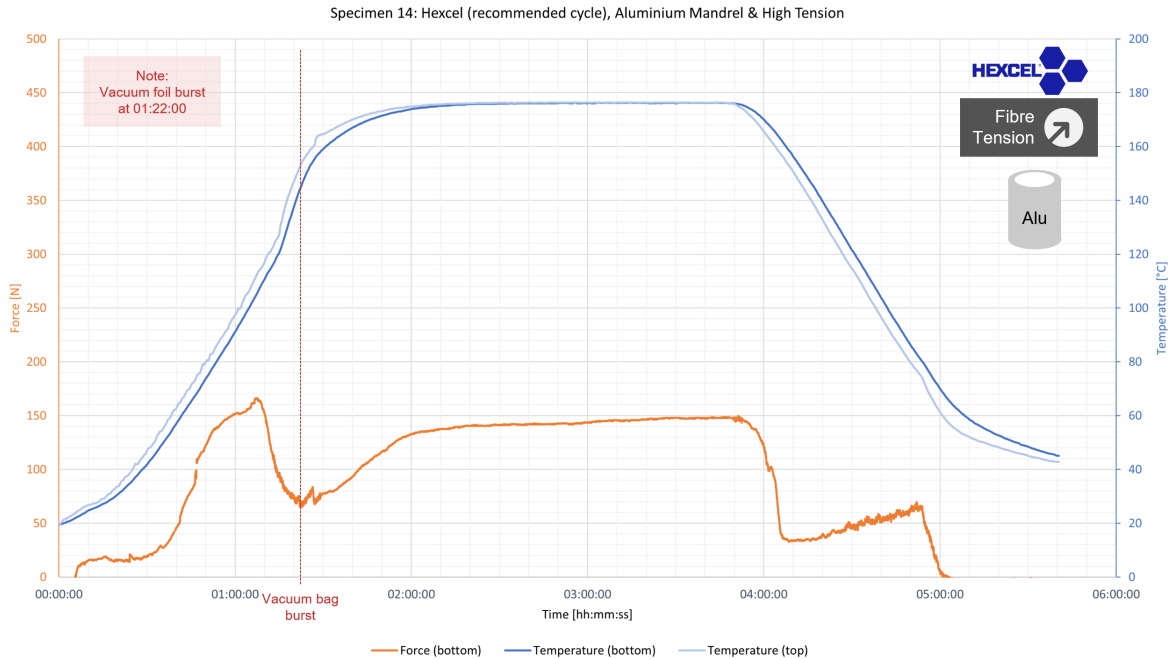
Figure 3.6: Pressure and temperature measurement of specimen 14.

Adding Viscosity

To identify correlations, the pressure and temperature graphs were enhanced by adding the resin viscosity data from the rheology study. To make the viscosity data from the rheometer comparable with the pressure and temperature data from the autoclave cure, a scaling correction was required, as explained in detail in the following.

Scaling the Rheology Measurement to the Autoclave Temperature During the rheology measurement, the same temperature profile was chosen as for the autoclave cure cycle. However, the laminate temperature in the autoclave falls behind because of the high thermal mass of the mandrel. In Figure 3.7 the continuous blue line refers to the temperature measured in the rheometer. Due to the fast temperature response, the rheometer closely followed the desired temperature profile for the laminate in the autoclave. The temperature measured at the laminate by the bottom thermocouple in the autoclave is given by the dashed blue line.

To use the viscosity data for the autoclave-cured specimens, the viscosity curve must be corrected or scaled to the temperature curve measured in the autoclave. One approach is to delay each viscosity data point by the same time as the temperature is delayed. For example, the delay between the autoclave and the rheometer to reach $100°C$ is around $13min$. It could then be assumed that the viscosity data point at that moment should also be delayed by $13min$. This method assumes that the viscosity is merely a function of the temperature. Although this may be true for thermoplastics, it is not applicable for thermosets as their viscosity is a function of the degree of cure and the temperature, as seen below.

$$\eta = \eta(\alpha, T) \tag{3.1}$$
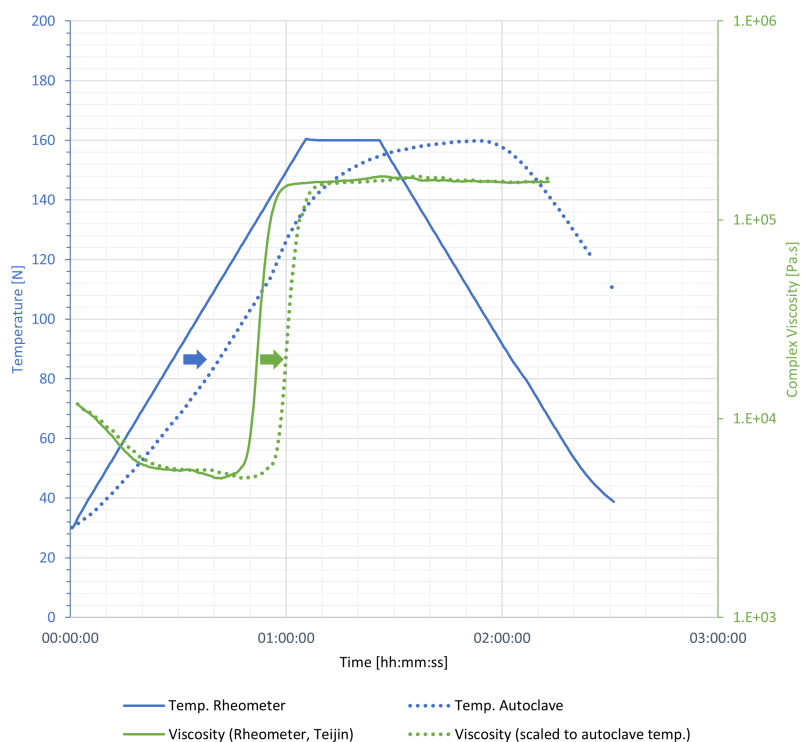
Figure 3.7: Comparison of rheometer temperature and autoclave temperature (in this case bottom thermocouple of specimen 08) combined with the viscosity graph.

where α is the degree of cure and depends on the temperature history to which the resin has been exposed.

A more accurate method is to scale according to the area underneath the temperature curves (i.e. the definite integral), as seen in the example in Figure 3.8. This takes into account the temperature and the time remained at a certain temperature. When the two areas $A_{\text{rheometer}}$ and $A_{\text{autoclave}}$ are the same, the difference in time yields the shift of the viscosity data point, as indicated by the green arrow. With this method, the viscosity data are scaled to the individual temperature curves of each specimen and then combined with the pressure and temperature graphs.

The autoclave temperature data used in this procedure is always the temperature measured between the mandrel and the laminate, referred to as *Temperature (bottom)* in the graphs. After the scaling operation, the viscosity line is added to the pressure and temperature graph as seen in Figure 3.9.
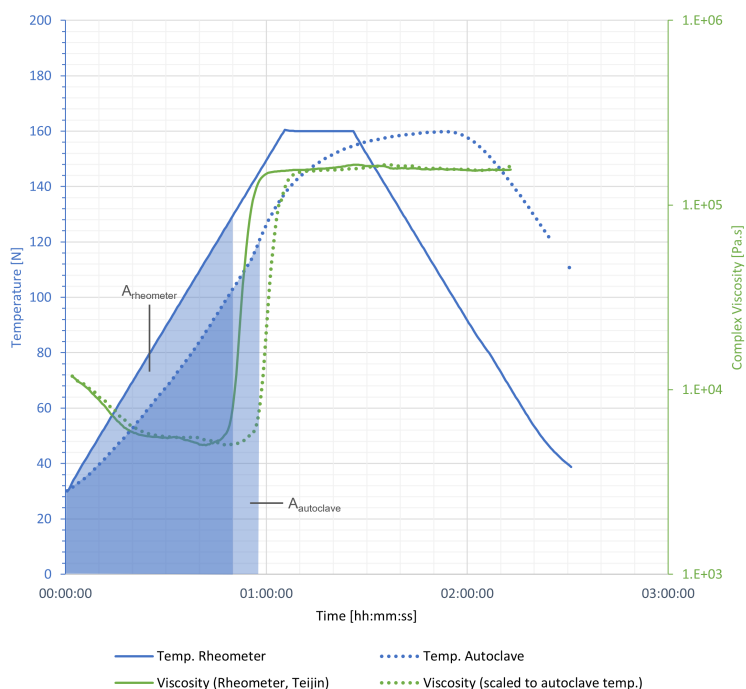
Figure 3.8: The viscosity line is scaled by the area underneath the temperature lines.
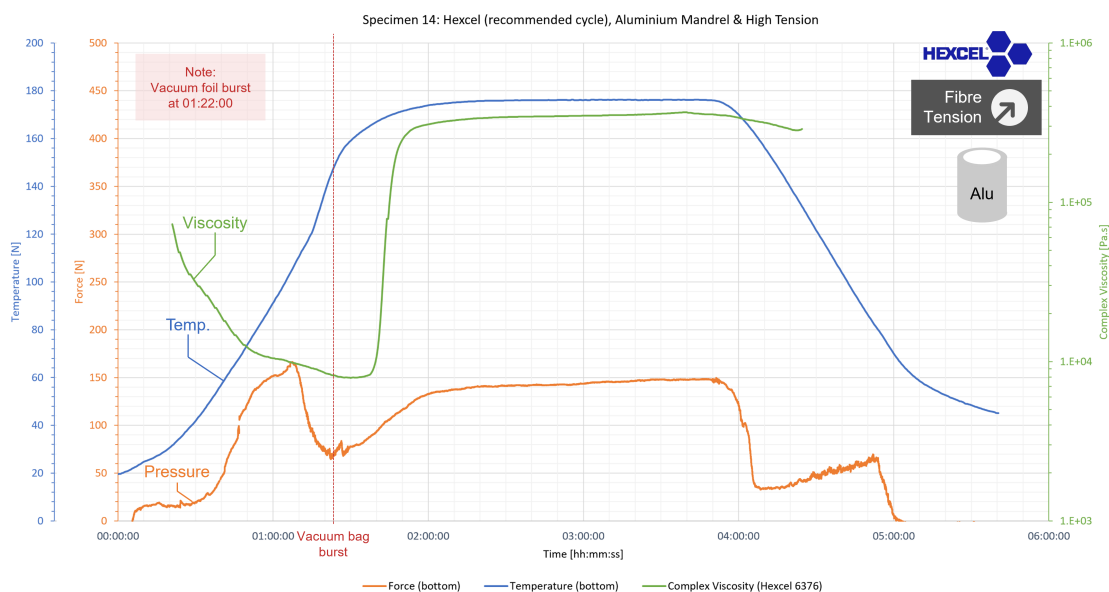
Figure 3.9: Pressure and temperature measurement of specimen 14 with viscosity curve.

Adding Degree of Cure

In the non-reversible heat flow curve in the DSC measurement, the curing enthalpy of the exothermal curing reaction of the resin is determined from the area underneath the graph as indicated by the hatched red lines in Figure 3.4 and A.3. The degree of cure at time t

is defined by the ratio of the enthalpy at t to the total enthalpy of cure (see Equation 1.5). The total enthalpy was achieved from the total area underneath the heat flow curve. For this, it must be assumed that the material was fully cured during the cycle. In order to match the temperature curve of the specimen in the autoclave, the calculated degree of cure must undergo the same scaling as previously described for the viscosity. The result is seen in Figure 3.10 for specimen 14 with Hexcel 6376 and in Figure 3.11 for specimen 08 with Teijin Q183. The latter also includes a pressure sensor at the middle location. Only two graphs are shown here. The graphs for all other specimens are found in Appendix B.
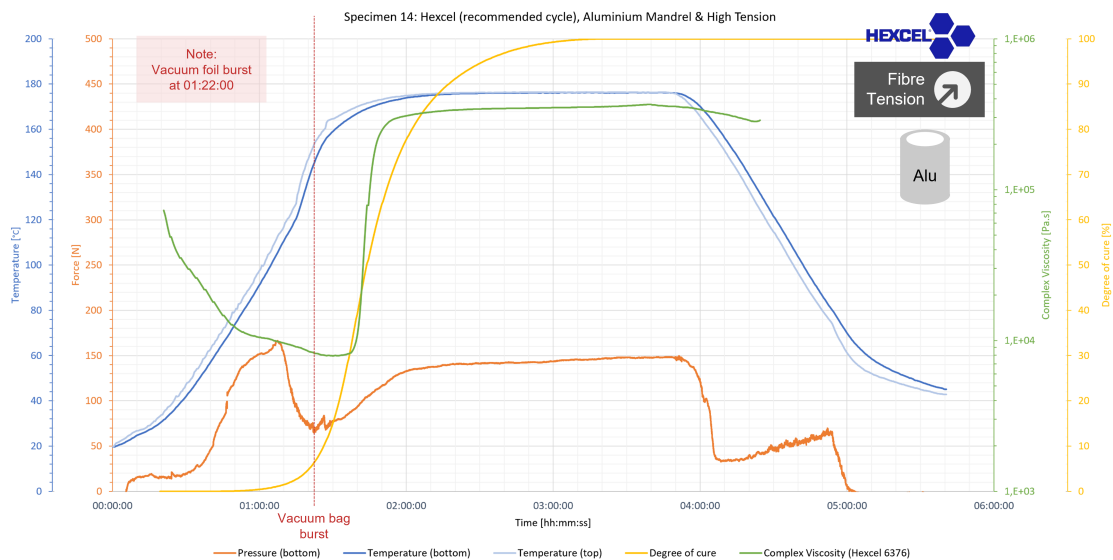
Figure 3.10: Pressure and temperature measurement of specimen 14 with viscosity curve and degree of cure.
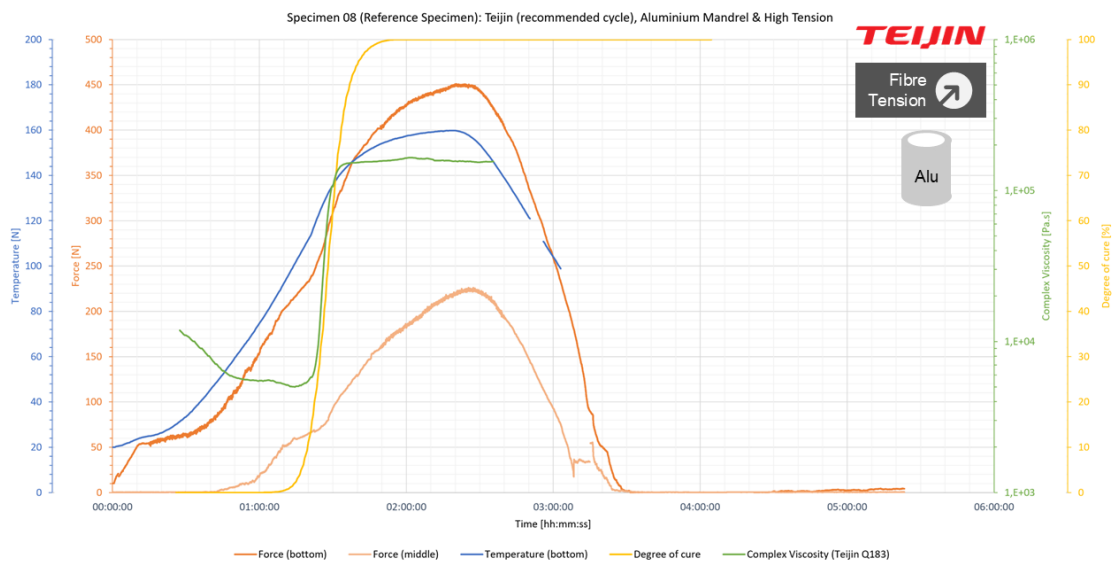
Figure 3.11: Pressure and temperature measurement of specimen 08 with viscosity curve and degree of cure.

3.3. Micrographs

Figure 3.12 and 3.13 show the microscopic images of Teijin Q183 specimen 08 and Hexcel 6376 specimen 14. The micrographs of the remaining specimens are found in Appendix C.
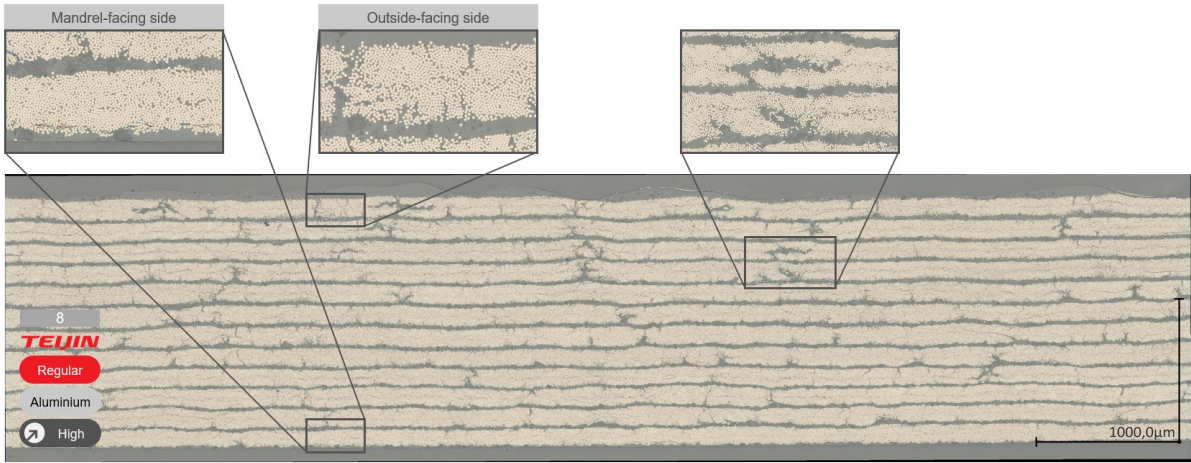
Figure 3.12: Micrograph of Teijin Q183 specimen 08 (high tension, aluminium mandrel). The lower side is the side of the mandrel.
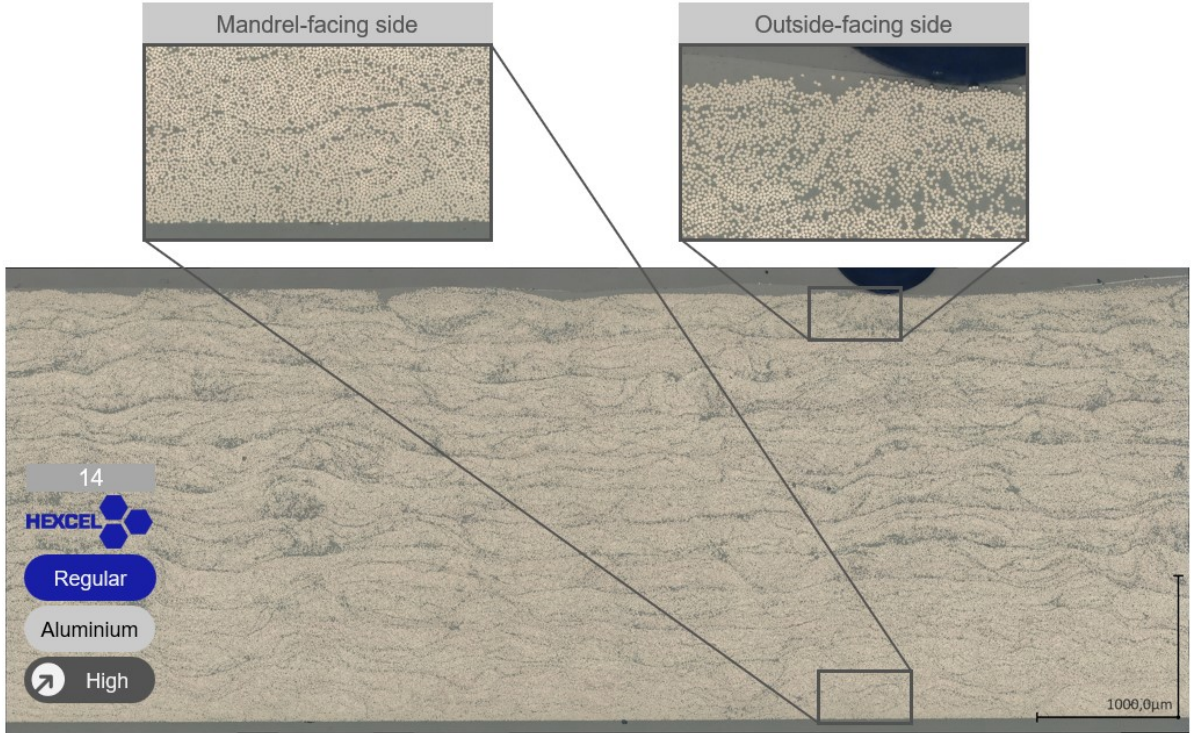
Figure 3.13: Micrograph of Hexcel 6376 specimen 14 (high tension, aluminium mandrel). The lower side is the side of the mandrel.

3.3.1. NMP Etching

As part of the optical microscopy of the micrographs, the method of etching the surface with NMP was applied on both materials. The Teijin Q183 material showed differences in the small round particles when comparing the images taken before and after etching in Figure 3.14. In Figure 3.15 some larger particles became visible with the etching as highlighted with blue circles. Hexcel 6376 showed no obvious changes due to etching as seen in Figure 3.16.
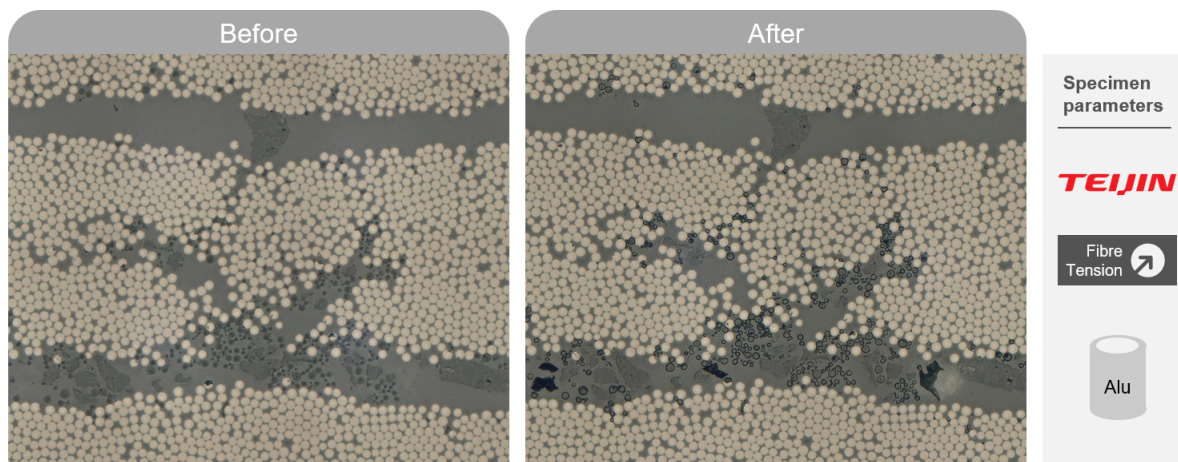
Figure 3.14: Micrographs of specimen 08 before and after etching with NMP.
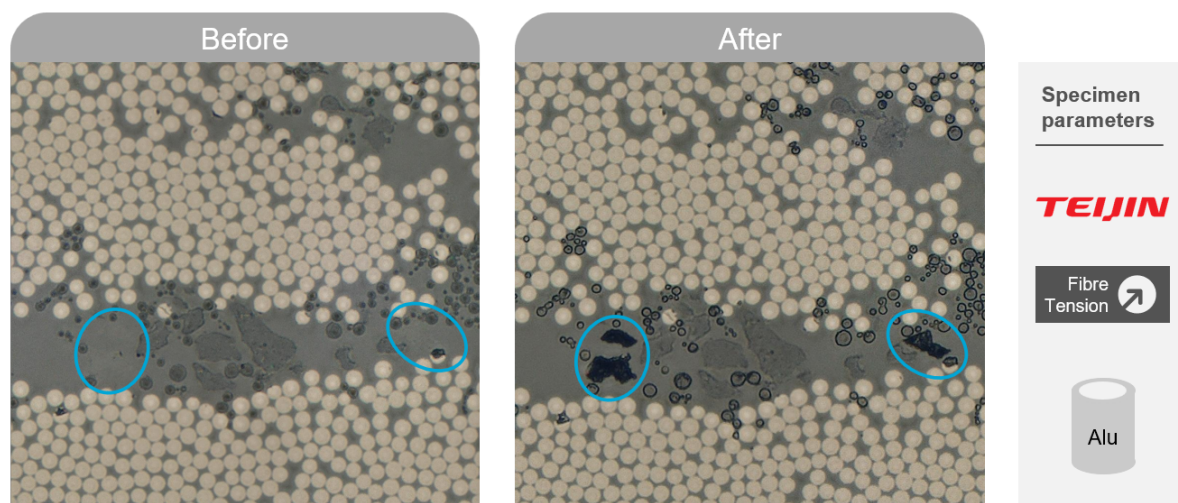
Figure 3.15: Micrographs of specimen 08 before and after etching with NMP. The blue circles indicate bigger TP particles that became visible by the etching.
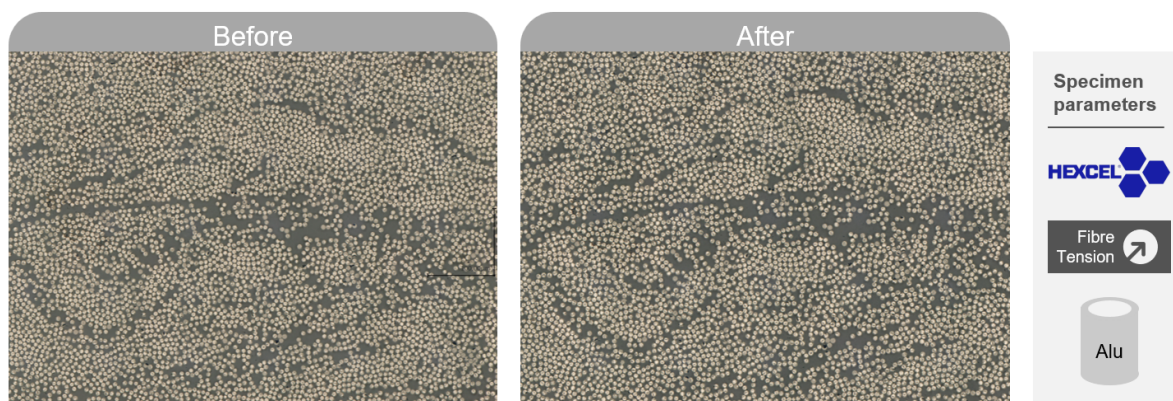
Figure 3.16: Micrographs of specimen 14 before and after etching with NMP.

3.3.2. Heat-Maps

The result of the heat-map generation to visualise the local FVF is seen in Figure 3.17 for Hexcel specimen 14. The heat-maps of the remaining specimens made from Hexcel 6376 are available in Appendix D. For the specimens made from Teijin material, no heat-maps are available, as the classification algorithm used to distinguish between fibres and resin was unable to correctly classify these micrographs. More training data are needed, including using specimens made from Teijin material to include these specimens in future studies.
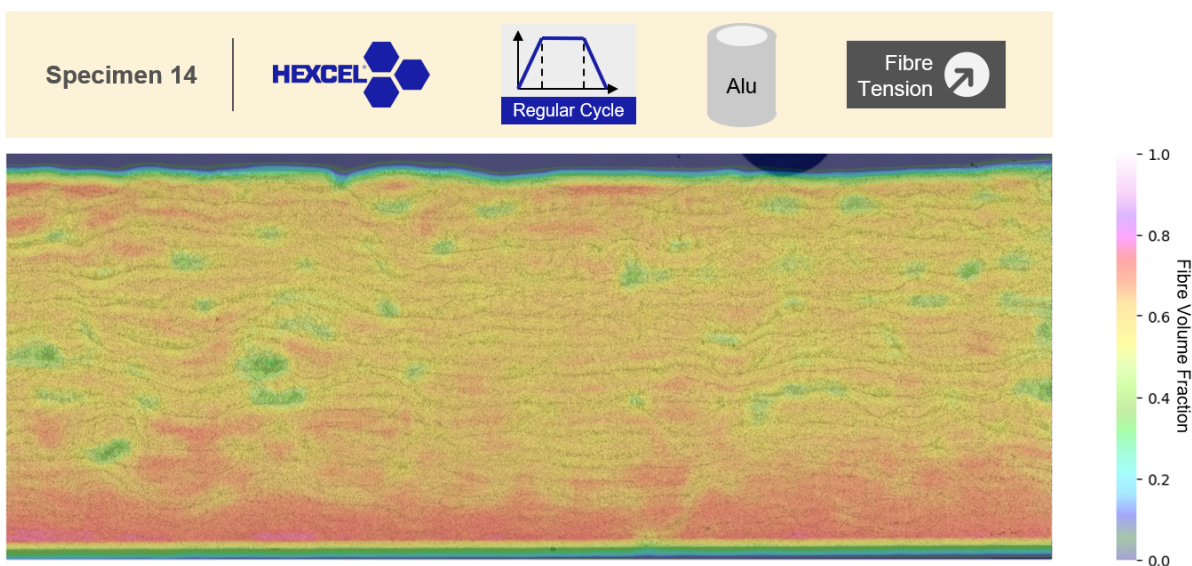
Figure 3.17: Heat-map of the local FVF of specimen 14.

The focus of this study is the gradient of FVF in thickness direction (i.e. the vertical direction in the micrographs and heat-maps). To be able to compare the specimens, the FVF values were averaged along the horizontal of the heat-map and plotted as a line as seen in Figure 3.18. Part of the heat-map is shown at the left of the plot to visualise the orientation of the plot with its horizontal FVF on the x-axis. For the calculation of the horizontal FVF the whole width of the heat-map was taken into account. The hatched areas on the top and bottom mark the two ends of the specimen and also include the area where the alogrithm introduces an error by

including pixels outside the specimen into the local FVF calculation. The oscillations observed in the plotted FVF along the thickness are related to the variations in FVF within the individual plies. Each plot shows 12 peaks, as showcased by the labels in Figure 3.18, which relate to the 12 plies per specimen. Some micrographs were not perfectly parallel to the horizontal of the image. This introduces a small error into the averaged results. However, the deviations from the horizontal are small enough to be negligible. The plots of the remaining specimens are found in Figure 3.19 to 3.23.
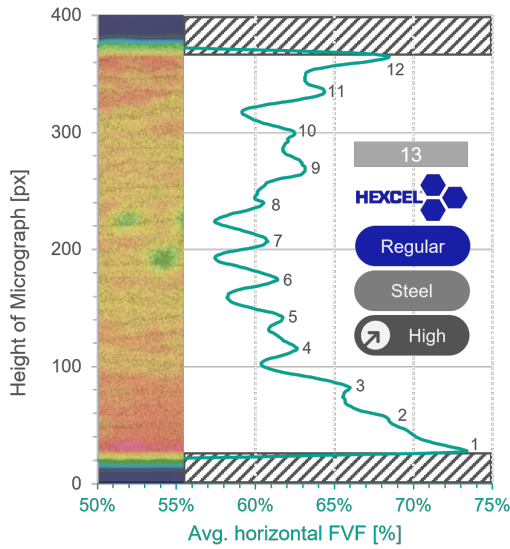
Figure 3.18: FVF profile along thickness of specimen 13.
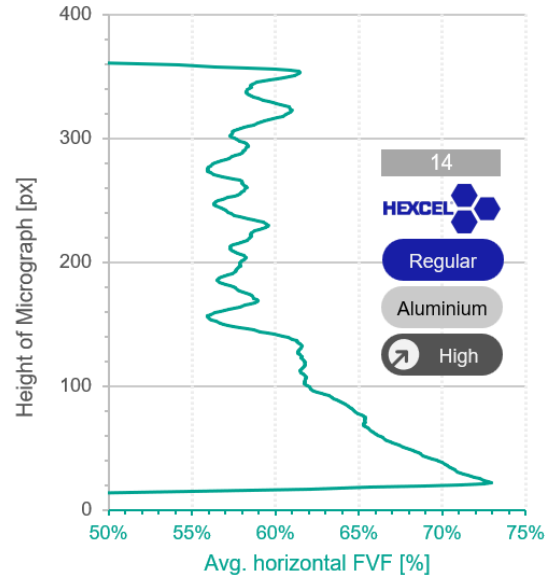
Figure 3.19: FVF profile along thickness of specimen 14.
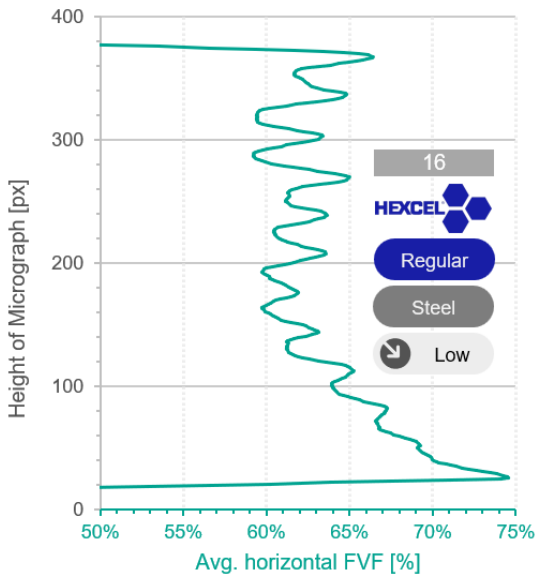
Figure 3.20: FVF profile along thickness of specimen 16.
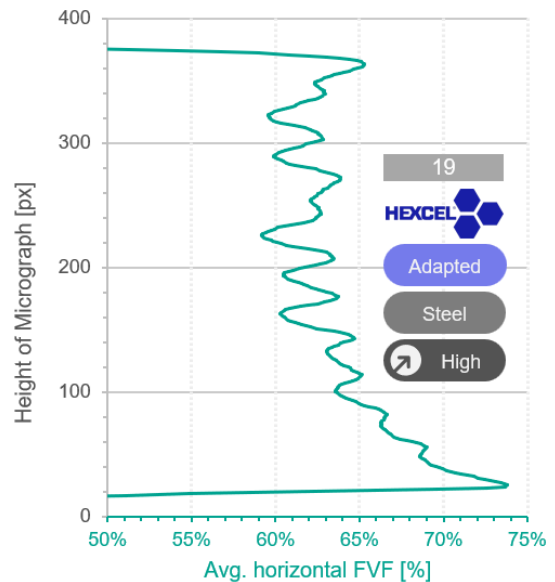
Figure 3.21: FVF profile along thickness of specimen 19.
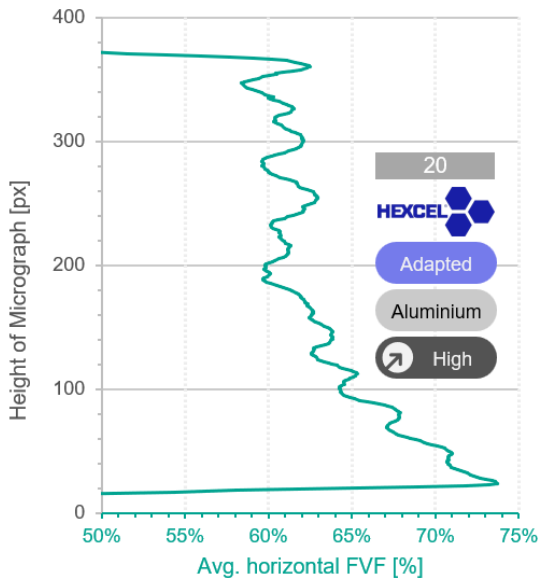
Figure 3.22: FVF profile along thickness of specimen 20.
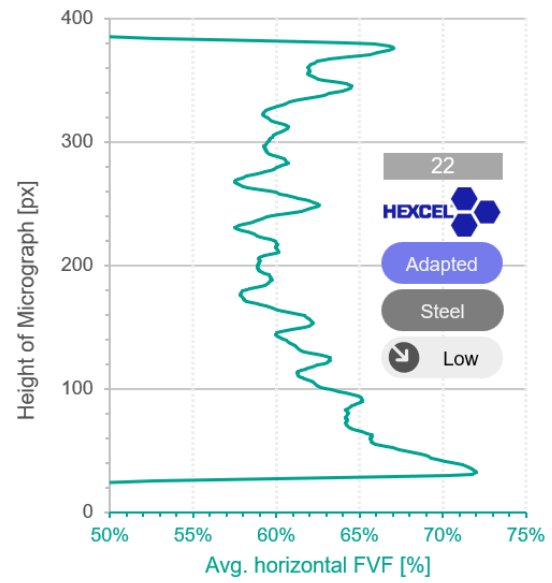
Figure 3.23: FVF profile along thickness of specimen 22.

As the resin flow phenomenon is an effect that spans among multiple plies, the curves should be flattened by averaging the data to allow for a comparison on a laminate scale. Averaging the data, removing the upper and lower ends and combining all lines into one graph leads to Figure 3.24.
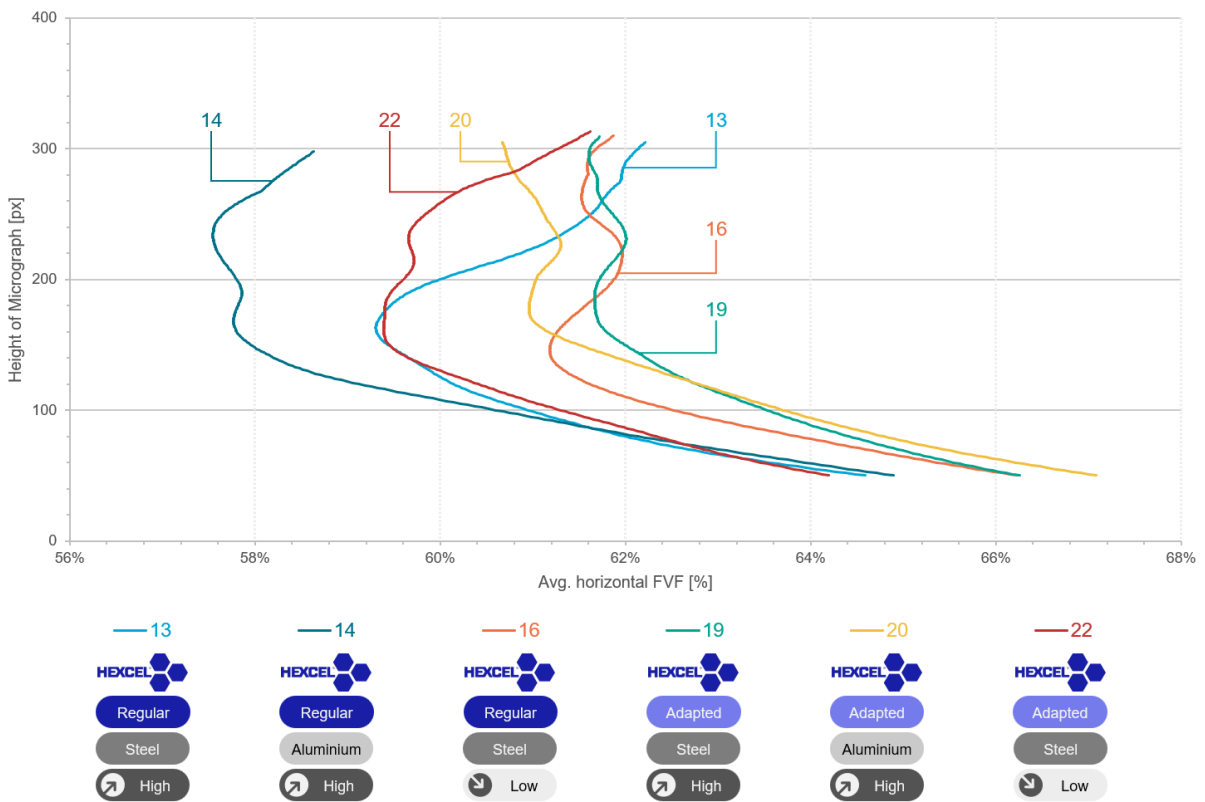
Figure 3.24: Averaged FVF profiles of all specimens made from Hexcel 6376 combined.

4

Discussion

The discussion chapter aims to provide a detailed interpretation and discussion of the results presented before. Section 4.1 discusses the general conclusions that can be drawn regarding the resin flow in Teijin and Hexcel specimens, regardless of the varied parameters. Section 4.2 then concludes how the variation in certain parameters influenced the resin flow, which is also the core of answering the research question. Next, section 4.3 discusses the applicability of the results of the small specimens on full-scale tanks. Finally, section 4.4 presents a manufacturing process guideline how parameters should be chosen to achieve a minimised FVF spread.

4.1. General Results of the Resin Flow Phenomenon

This section is split into two parts, one for Hexcel 6376 and one for Teijin Q183, as some effects are more pronounced in the graphs of one or the other material.

4.1.1. Interpretation of Hexcel 6376 Specimens

The data recorded during the curing cycle and material characterisation measurements provide coherent evidence on the resin flow phenomenon posed as a hypothesis in the Introduction chapter. Based on Figure 4.1, the pressure sensor curve in relation to the viscosity curve and the degree of cure are interpreted below.
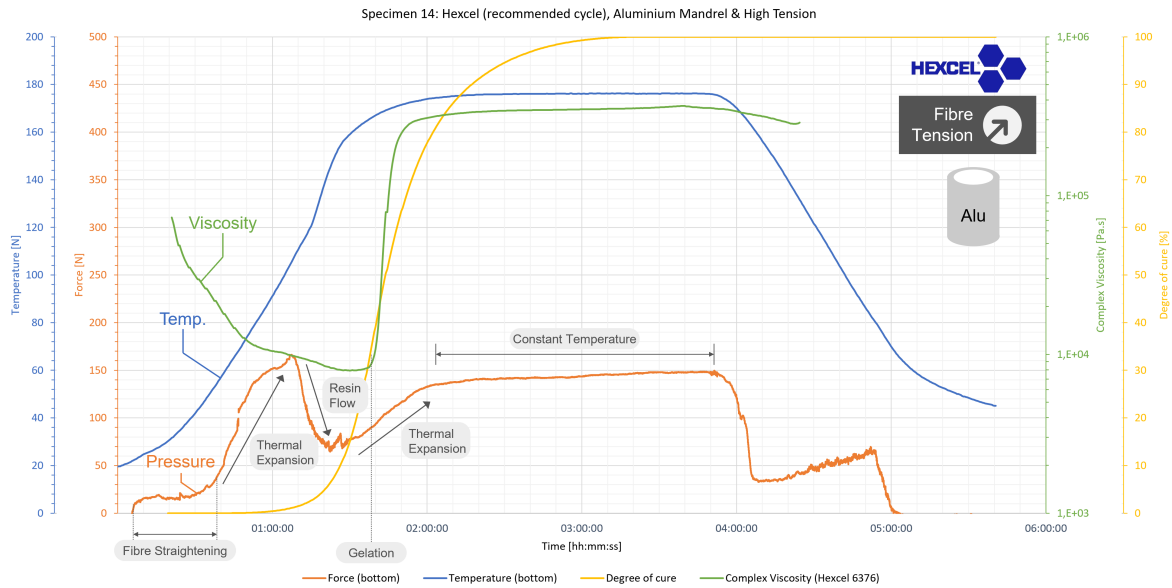
Figure 4.1: Interpretation of Hexcel 6376 pressure curve during autoclave curing.

Fibre Straightening At $t = 0$ the graph starts with the uncured material on the mandrel. As the temperature of the autoclave increased, the temperature of the mandrel also increased, and the thermal expansion led to an increase in mandrel diameter. The fibres that were wrapped around the mandrel had a CTE of slightly below 0 and therefore work against the expansion of the mandrel, creating pressure at the interface between laminate and mandrel. This pressure was captured by the pressure sensor. With increasing temperature, the pressure was expected to increase; however, the pressure remained roughly constant from 00:07:00 to 00:34:00. This can be explained by the effect of fibre straightening illustrated in Figure 4.2. The tortuosity and undulations of the fibres and the imperfections introduced during manufacturing were flattened in this phase. In fact, beyond the 2D plane observed in the illustration, this also applies to the depth direction where the fibre variabilty is flattened. The thermal expansion first had to exceed this clearance, or free play, of the system before the fibres were fully loaded in tension and generated the pressure measurable by the sensor.
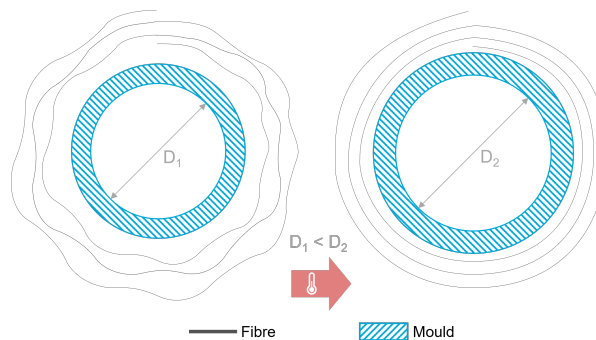
Figure 4.2: Illustration of the fibre straightening effect.

The free play of the system can be calculated from the temperature difference during which the pressure remains constant on average. Figure 4.3, a cut-out of Figure 4.1, graphically determines this temperature range to be from $23°C$ to $48°C$.
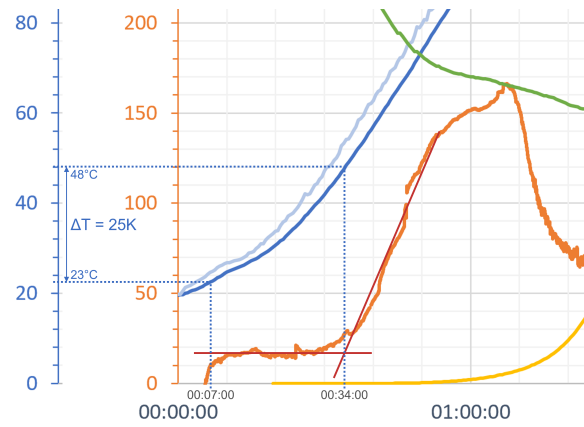
Figure 4.3: Temperature range of fibre straightening.

To calculate the thermal expansion, it was assumed that the thermal expansion of the wall thickness was negligible. The increase in diameter mainly stemmed from the thermal expansion in the circumferential direction. By theoretically opening the circumference C_0 and spreading it along a straight line as visualised in Figure 4.4, the thermal expansion of the circumference ΔC could be calculated by the formula for linear thermal expansion, as stated earlier in Equation 1.2. The mandrel in the given case was made from aluminium 6082 with $\alpha_L = 24 \cdot 10^{-6} m/mK$ and an outer diameter of $350mm$ at $23°C$. The circumference is therefore $C_0 = 1099.56mm$ and $\Delta T = +25K$, which yields the following:

$$\Delta C = C_0 \alpha_L \Delta T = 0.66mm \tag{4.1}$$

Hence the circumference at elevated temperature is $1100.22mm$. Converting this back to the diameter yields that the mandrel has a diameter of $D_1 = 350.21mm$ at $48°C$. This means that free play in the system allowed an increase in diameter of $\Delta D = 0.21mm$ or 0.06%.
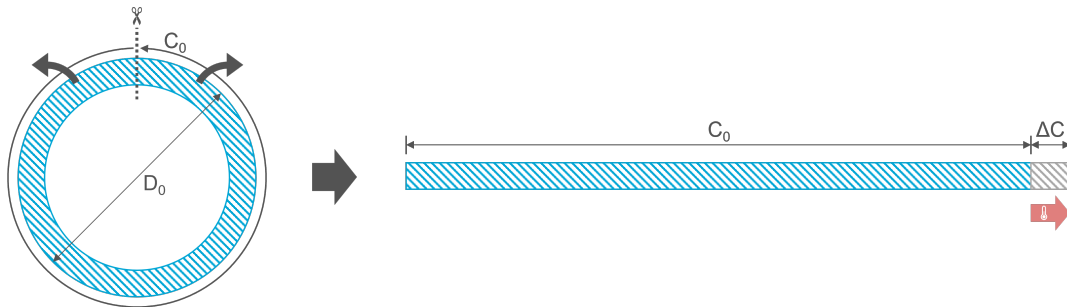
Figure 4.4: Thermal expansion of a hollow cylinder in circumferential direction.

Thermal Expansion Once the thermal expansion of the mandrel could not be absorbed through the fibre straightening anymore, the pressure began to increase more steeply because the fibres were then working against the mandrel and caused an increase in pressure.

Resin Flow As temperature increases, the viscosity decreases. According to Darcy's equation, a decreased viscosity increases the resin flow rate. This was also observed here. Once the viscosity of the resins was low enough, it was able flow. The fibres moved closer to the

mandrel, as this would release part of the tension. The reason for this is that closer to the mandrel, the circumference is smaller, which means that the elongation and tension are lower. This tendency to move inward causes opposing pressures that push the resin outward. This process can be imagined as an exchange of fibres moving inward and resin moving outward. After a while, the resin flow slowed down for two reasons. Firstly, a sufficient amount of fibres had moved close to the mandrel such that the fibres were already touching the adjacent fibres, which left no space for further compression and resin that could be pushed outward. The micrograph of specimen 14 (Figure 3.13) in fact shows that many of the fibres in the lower part (closer to the mandrel) were in direct contact with adjacent fibres, while the top most fibres mostly had resin all around individual fibres. Secondly, the progress of the cure of the resin led to gelation during which the viscosity rapidly rose and locked the fibres in place such that no resin could flow anymore. The gelation aligned with the degree of cure. This reinforces and verifies the correct execution and evaluation of the rheology study and the DSC measurement because the gelation was based on crosslinks formed during curing, which limit molecular mobility.

Thermal Expansion   Once the resin flow stopped, the fibres could no longer release tension through this phenomenon. The mandrel temperature and therefore its diameter still increased, which led to a second pressure increase.

Constant Temperature   Once the temperature plateau was reached and the mandrel temperature flattened out, the thermal expansion stopped and, therefore, the pressure remained constant.

Cool-down Phase   After the temperature plateau, the temperature of the mandrel and laminate decreased. As this is the reverse process of the thermal expansion, the pressure decreased with the shrinking mandrel. However, from 04:05:00 to 04:55:00 an increase in pressure could be observed. A similar trend was observed in specimen 13. The observed phenomenon can be explained by the following hypothesis: During the initial pressure decrease, the contact pressure remained relatively high, resulting in significant static friction at the mandrel-laminate interface, preventing any relative movement between the two surfaces. However, as the pressure continues to drop, it eventually reaches a point where the static friction is overcome, allowing small movements at the interface. These movements are likely caused by the mandrel's axial shrinkage, which exceeds that of the laminate. As a result, the sensor experiences shear loading, leading to an increase in the signal due to the piezo-crystal's sensitivity to shear forces. As the mandrel continues to shrink, it eventually completely separates from the laminate, reducing the pressure to zero. In future tests, the sensor could be shielded with a different release film, which provides better decoupling from shear forces.

4.1.2. Interpretation of Teijin Q183 Specimens

The specimens made of Teijin Q183 show a different pressure graph and are interpreted based on Figure 4.5. In general, the holding plateau of $20min$ at $160°C$ was just long enough for the laminate to reach $160°C$ and then immediately cool down again. Therefore, no plateau in temperature or pressure is seen.
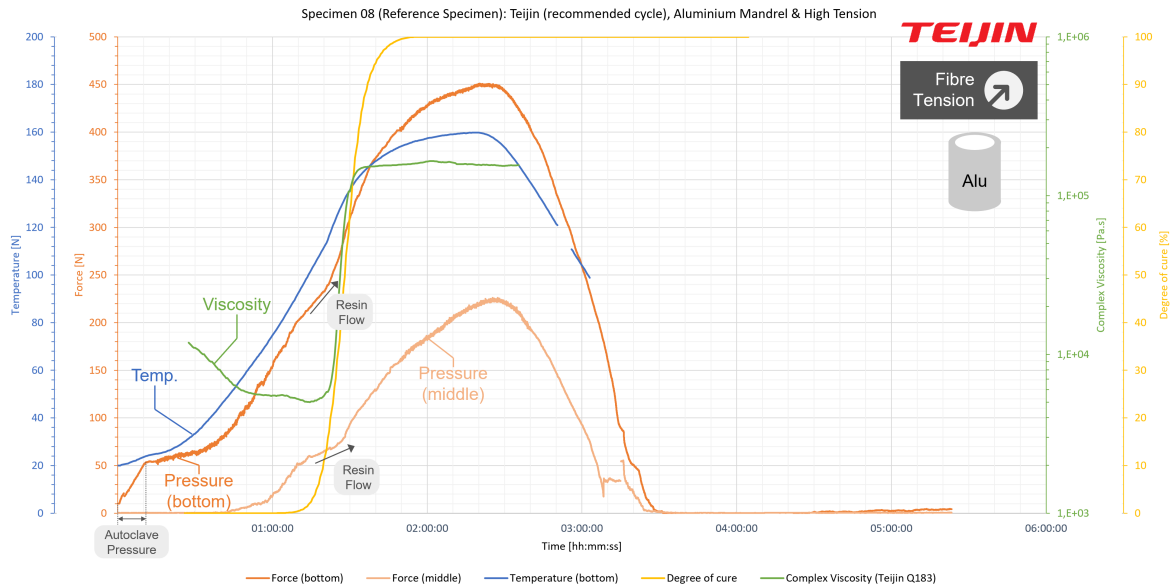
Figure 4.5: Interpretation of Teijin Q183 pressure curve during autoclave curing.

Resin Flow   Compared to the Hexcel 6376 specimens, the pressure drop due to resin flow was much less distinct in the Teijin Q183 specimens and only visible as a temporary change in slope but with a sustained strictly monotonic increase. Combining the pressure curve with the viscosity curve and the degree of cure confirms that the temporary change in slope indicates a phase of resin flow. However, the extent of the change in slope is much less and superimposed by the pressure increase as a result of thermal expansion. This can be explained by the different viscosity profiles of the two materials as seen in Figure 4.6. The data in this graph originate from the manufacturers, who tested the resin without fibres and therefore were able to provide reliable data for the absolute values, which was not possible during the rheology study performed for this thesis. According to the graph, Teijin's minimum viscosity is higher and occurs at a lower temperature ($8.6Pa.s$ at $100°C$) compared to Hexcel ($3.5Pa.s$ at $150°C$). Since the viscosity is inversely proportional to the resin flow rate in Darcy's equation (see Equation 1.3), a higher viscosity leads to less resin flow. In addition, the minimum viscosity is reached at a lower temperature. At that lower temperature, the mandrel had less thermal expansion and therefore less fibre tension, which ultimately leads to a decreased magnitude of the pressure in Darcy's equation. This also leads to a lower resin flow rate.
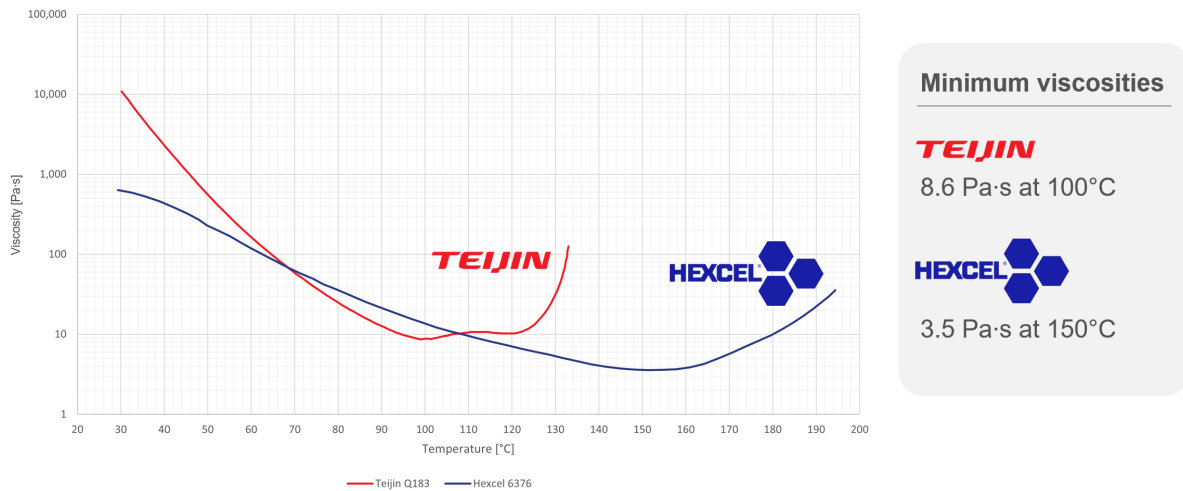
Figure 4.6: Resin viscosity of Teijin Q183 and Hexcel 6376 as provided by the manufacturers (both lines with 2K/min heat ramp) (Data retrieved from the respective data sheets).

Autoclave Pressure   At the beginning of the diagram from 00:00:00 to 00:10:00 the sensor captured the build-up phase of the autoclave pressure from 0bar to 5bar. This was also captured for specimens 11, 13, 16, 19 and 20, but not for the other specimens. The unforeseen correlation is that only those sensors that had been used in an earlier autoclave cycle captured the initial pressure increase . New sensors that had not yet been used (for instance, the middle sensor in Figure 4.5) did not capture the increase in autoclave pressure in the beginning. This difference in measurement can be attributed to insufficient conditioning of the sensor prior to its use. The manufacturer recommends loading the sensor multiple times to 120% of the maximum expected application load. This was done before the sensor calibration. However, because calibration was performed with the puck on the sensing area, as recommended by the manufacturer, the conditioning only affected the area just under the puck and not the full sensing area. This then led to inferior measurement signals in the early measurement period. With increasing pressure from the specimen, the conditioning was then completed during the experiment and the sensor delivered appropriate measurements for the remainder of the experiment. When the sensor was reused in a new specimen, it was already preconditioned from the beginning and captured the autoclave pressure without issue.

Middle Pressure Sensor   When looking at the maximum pressure measured at 02:25:00, the pressure sensor implemented in the middle of the laminate between plies 6 and 7 (see *Force (middle)* in the graph) measured half the pressure compared to the sensor at the bottom. This confirms the assumption that pressure builds up by superimposing the pressure exerted by each ply on top of the pressures of the plies above, as described by Tzeng (1988). The highest pressure is therefore below the lowest ply and half the pressure at half the laminate thickness, which suggests a linear relationship for the pressure gradient along the thickness. However, with the inaccuracies of the sensor it cannot be said with sufficient confidence that the relation is indeed linear. In future studies, more than two sensors should be distributed along the thickness of the laminate to investigate the pressure gradient.

Differences Autoclave Cycle 1 & 2   Autoclave cycles 1 and 2 were identical in their settings for curing the Teijin Q183 material. Specimens 01, 02, 03, and 04 were cured in cycle 1, while

specimens 08 and 11 were cured in cycle 2. A pressure drop was observed in all specimens from cycle 2, but not in any from cycle 1. This difference may be related to the waiting time between specimen manufacturing and the autoclave cycle. Specimens in cycle 1 were stored for 3 days, whereas those in cycle 2 were stored for 2 days. During storage at room temperature, the prepreg likely continued to cure slowly. The additional day of curing for cycle 1 specimens may have progressed to the point where the viscosity remained too high during the autoclave cycle to allow resin flow. Alternatively, the material in cycle 1 specimens may have settled more during the longer waiting time, reducing resin flow, or the sensor might have been affected by the prolonged pressure. Other possible factors include undetected deviations in the manufacturing process, such as the placement of breather material or vacuum bag overlap directly on the sensor, which could have influenced the measurements.

4.2. Specific Results of the Parameter Variation

In this section, the correlations between the varied parameters, pressure measurements and resin flow (i.e., FVF gradient) are discussed based on three indicators, which are maximum pressure, pressure drop, and the spread in FVF. The values of these indicators are shown per specimen in descending order.

Maximum Pressure In Figure 4.7 the respective maximum force values measured by the bottom pressure sensors during the cure cycle of each specimen are shown in descending order. It should be noted that the pressure sensor of sample 4 failed, and therefore no data can be shown. Specimen 11 used a cross-ply layup and is therefore not directly comparable with those with a pure UD layup. It will be discussed separately at the end.

Figure 4.7: Maximum force measured during the autoclave cycles by the respective bottom pressure sensors per specimen in descending order.

Pressure Drop The pressure drop of specimens 13, 14, 16 and 20 (all made from Hexcel 6376) are included in Figure 4.8, as only these specimens showed a distinct pressure drop that led to a decrease in pressure. The Teijin specimens showed a decrease in slope, but the pressure nevertheless increased. For better comparability, the pressure drop is expressed relative to the high point before the drop.
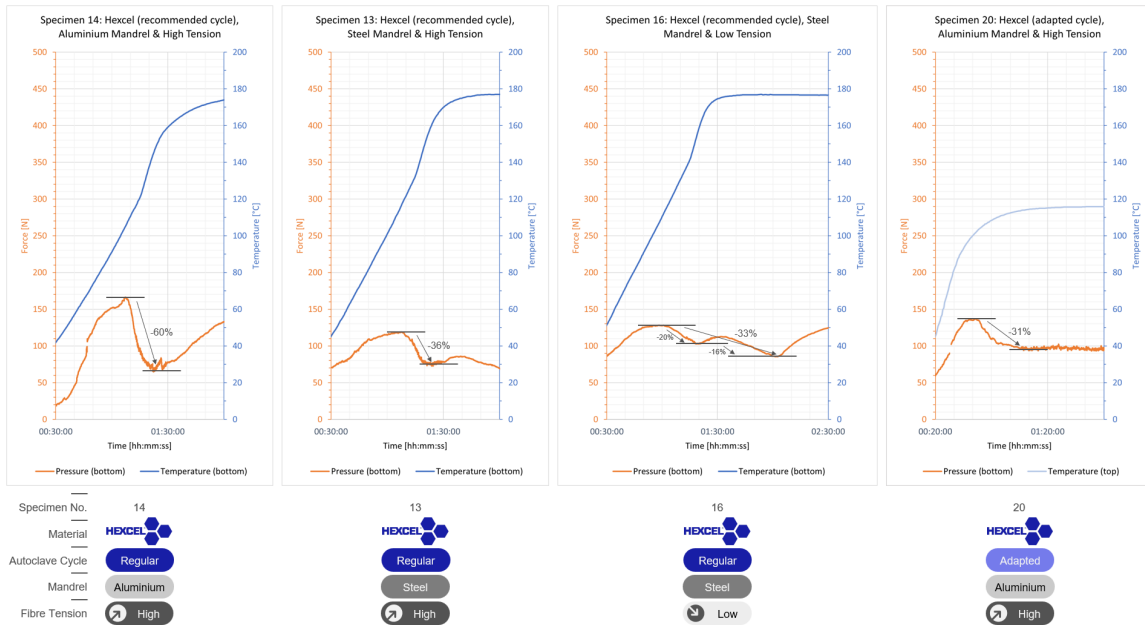
Figure 4.8: Pressure drop per specimen. Sorted in descending order.

Spread in FVF From the FVF gradient graphs in Figure 3.24, the maximum and minimum values could be extracted and plotted in Figure 4.9. The difference between the maximum and minimum values is referred to as the spread in FVF and the specimens are sorted according to this in descending order. The maximum and minimum values were retrieved from the averaged version of the FVF gradient graphs, as its scale is more suited for phenomena on the laminate level than the unaveraged FVF gradient graphs. The resolution in these graphs is high enough to show the FVF gradients within a single ply. The specimens made from Teijin Q183 could not be included here as the classification algorithm did not correctly separate the fibres and resin in the micrographs made of Teijin Q183.
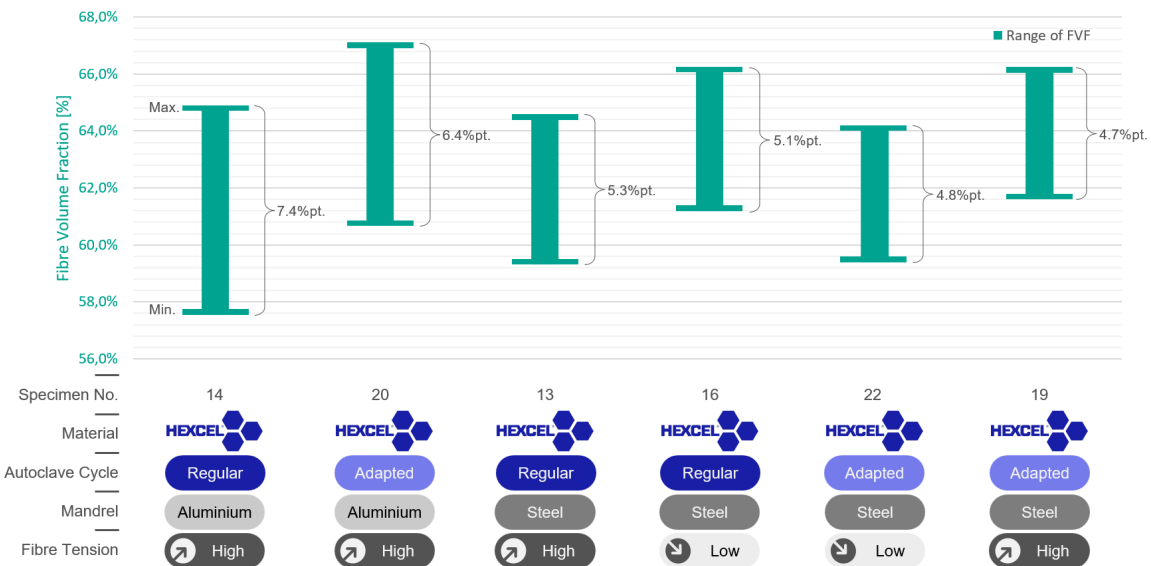
Figure 4.9: Comparison of local FVF range per specimen after averaging. Specimens are sorted according to the spread in descending order.

Varied Parameters

Based on these three indicators, the effect of each varied parameter is discussed below.

Resin Material   According to Figure 4.7, the highest pressures were achieved by the Teijin specimens. The Hexcel specimens which were cured with the adapted cycle also show high pressures; these are discussed in the next section on autoclave cycle adaption. The specimens made from Hexcel which were cured in a regular cycle led to the lowest pressure values. The FVF spread in Figure 4.9 only shows Hexcel specimens as the image recognition algorithm failed with the Teijin specimens. However, from visual observation of the micrographs, the spread in FVF was less in all Teijin specimens than in the Hexcel specimens. The higher gradients in the Hexcel specimens hint at a higher resin flow rate. Because resin flow is a way to release pressure and tension from the fibres, it can be concluded that a resin with a low viscosity profile and high gelation temperature, such as in the Hexcel material, results in high resin flow rates, which cause the fibre tension to dissipate and thus leads to comparatively low pressures but also high spread in the FVF. Out of all the parameters studied, the resin material had the highest impact on the FVF gradient.

Autoclave Cycle Adaption   In comparing the Hexcel specimens of the apdapted cycle with those of the regular cycle, the adapted cycle constantly leads to higher maximum pressures. Figure 4.9 shows that the spread in FVF is lower when comparing specimens of the same mandrel material (i.e. 22 & 19 have a lower spread than 13 & 16 and 20 has a lower spread than 14). The observed correlation is similar to the comparison between Hexcel and Teijin. High pressure values are a sign of small resin flow rates as more resin flow would have reduced the pressure. Small resin flow rates result in a low FVF gradient. The goal of the adapted cycle was to reduce the FVF gradient in comparison with the regular cycle. The data show that this had limited success. The reduction in spread was small, as seen from the percentage points in Figure 4.9. The choice of mandrel material had a greater impact on the spread than the adaption of the autoclave cycle. The adaption still appears to be a suitable method to reduce the resin flow when it is not feasible or too costly to change the other parameters. However, the disadvantage of this approach was a much longer cycle time, which increased autoclave occupancy, overall manufacturing duration, energy consumption and therefore cost. The adapted autoclave cycle used in this experiment was developed without DSC and rheology measurements and therefore still has great potential for improvement. In the adapted cycle, the material was cured with a $5h$ plateau at a reduced temperature of $115°C$. The regular cycle ($2h$ at $175°C$) was added as a second plateau afterwards to guarantee a full cure of the material. With better knowledge as to when the material would reach the final degree of cure, the regular cycle could be shortened. More knowledge on the rheology would help to improve the low temperature plateau to further decrease the FVF spread. For this, a follow-up study with additional DSC and rheology measurements may be necessary, as suggested in chapter 6, Recommendations for Future Work.

Mandrel Material   Within the group of Teijin specimens or the group of Hexcel specimens with regular cure, the aluminium mandrels consistently led to higher pressures than the steel mandrels. As it was hypothesised, this occurs due to the higher CTE of aluminium ($24 \cdot 10^{-6} m/mK$) versus steel ($12 \cdot 10^{-6} m/mK$). However, within the group of Hexcel specimens cured with the adapted cycle, specimens 22 and 20 did not perform as expected. Specimen

22, which was on a steel mandrel, resulted in higher pressures than specimen 20, which was on an aluminium mandrel. In this case, specimen 22 was most likely an outlier with abnormally high pressure readings. When comparing the FVF spreads, specimens with aluminium mandrels (14 & 20) yielded the greatest spreads in FVF while the steel mandrels (16, 22 & 19) led to lower fractions. In the FVF comparison, specimen 22 delivered results fitting the hypothesis; this reinforces the suspicion that the abnormal high maximum pressure values are outliers. The results of the FVF spread comparison are mostly confirmed when measuring the pressure drop, as depicted in Figure 4.8. Specimen 14, with regular cure and an aluminium mandrel, showed the highest pressure drop and also the highest FVF spread. Specimens 13 and 16 follow before specimen 20, which follows a reverse order compared to Figure 4.9. A potential cause for this might be that the resin flow and pressure drop in the adapted cycle of specimen 20 still continued during the holding plateau and was therefore measured as too low. This is possible because the gelation was delayed as a result of the reduced temperature compared to the regular cycle. The measured pressure drops of specimens 13, 16 and 20 were very close to each other with , -36%, -33% and -31%, respectively. A small change could result in the same order as the FVF comparison. The other specimens of the adapted cycle did not show a distinct pressure drop. This is due to the aluminium mandrel of specimen 20 which reached a thermal expansion sufficient enough to cause resin flow while the steel mandrels thermal expansion in specimens 19 and 22 remained too low for this. In conclusion, mandrels with higher thermal expansion, such as aluminium over steel, led to higher maximum pressures, higher pressure drops and higher FVF spreads.

Overall, the viscosity profile of the resin had the highest influence on the gradient in FVF. The mandrel material (aluminium vs. steel) had the second highest influence and the autoclave cycle adaption the third highest influence.

Winding Fibre Tension The winding fibre tension did not show a consistent correlation with the maximum pressure, the pressure drop or the FVF spread. An influence was expected to occur at the beginning of the autoclave cycle, as the initial fibre tension of the winding is quickly exceeded by the additional tension caused by the thermal expansion of the mandrel once the autoclave heats up. Due to the measurement behaviour of the sensor depending on whether it had been used before or not, insufficient reliable data is available to draw a conclusion on the impact of the winding fibre tension. However, it is assumed that it does not have a significant influence as the tension caused by the thermal expansion greatly exceeds the mandrel winding tension.

Stacking Sequence Specimen 11 was the special specimen with a $[0°_4/90°_4/0°_4]$ cross-ply layup that caused a different pressure gradient as only the $0°$ fibres contributed to the pressure at the interface. As the $0°$ plies made up $2/3$ of the laminate, it was expected that the pressure would be reduced by roughly $1/3$ compared to specimen 2 or 8. The results showed that the maximum pressure was reduced by more than half. One possible explanation is that the $90°$ plies do not contribute to the pressure but contribute to the resin flow as they receive pressure from the $0°$ block above. The $90°$ plies would then reduce the pressure of the $0°$ block above without introducing their own pressure.

4.3. Applicability to Larger Diameters

To reduce cost and complexity the specimens diameter was chosen to be only $350mm$ which is a standard size for industrial tubing. To transfer the results on the scales of a real hydrogen tank, the applicability to those larger diameters has to be discussed.

A typical design of a mandrel looks like the one in Figure 4.10. This mandrel is part of the HyStor project[1] which investigates manufacturing aspects of the dome and cylindrical part of a hydrogen tank made from CFRP. The mandrel is made from steel S235 with an outer diameter of $3m$ and a length of $2.5m$. It consists of a shell that is connected to the central axis through multiple planes of spokes.
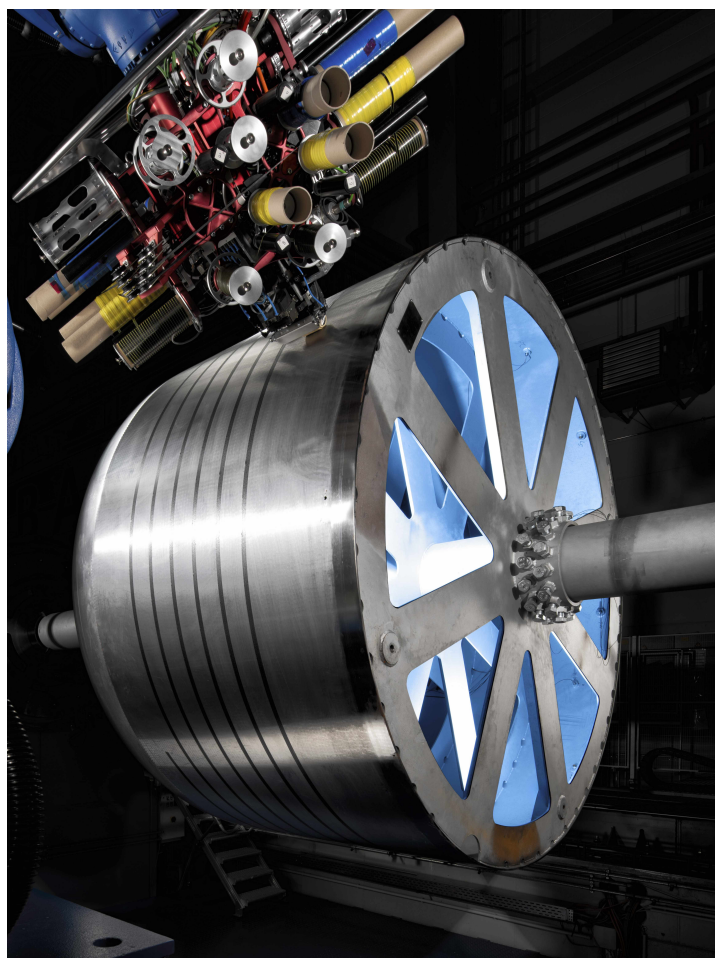
Figure 4.10: HyStor mandrel with rotational axis and AFP endefector (DLR).

The small mandrels used for the thesis at hand had a wall thickness of either $25mm$ (aluminium) or $10mm$ (steel) and no spokes as the shell carries itself. The HyStor mandrel needs spokes to create a connection between the axis and the shell and to keep the shell in the desired shape. The shell's wall thickness is only $10mm$.

The ratio between the laminate thickness and the tool's wall thickness influences which struc-

---

[1] https://leichtbau.dlr.de/speicherung-von-kryogenem-wasserstoff-in-composite-flugzeugtanks [Accessed: Aug. 26, 2024]

ture has higher rigidity and therefore takes the lower share of the strain in the incompatibility problem caused by the discrepancy in CTE. The wall thickness of the small mandrel is high compared to the laminate thickness. The thermal expansion of the mandrel wall thus dominates over the stiffness of the fibres and causes high strains and stresses in the fibres leading to the pressures measured in this study. In larger mandrels, such as HyStor, the wall thickness of the mandrel is low compared to the laminate thickness and the balance of rigidity is more towards the laminate, which means that a larger part of the thermal expansion is transformed into compressive strains of the mandrel which can lead to lower tension in the fibres.

The inclusion of spokes for structural reasons has the disadvantage that the thermal mass of these spokes creates local heat sinks. During a heat up phase, the region on the shell close to a spoke typically shows lower temperatures as it takes more time to reach the temperature. During a cool down phase, the opposite is true and that particular region remains warm for longer due to the higher thermal mass. This results in an inhomogeneous temperature distribution on the shell that impacts the local curing progress and rheology behaviour. In addition, the thermal expansion varies locally, leading to an inhomogeneous pressure field that could lead to more complex phenomena of resin flow.

The way in which the pressure caused by the fibre tension scales with increasing diameter of the mandrel had to be analysed. To derive this, a small portion $d\alpha$ of the mandrel was observed in its cross-section as seen in the left of Figure 4.11. Only a small section $d\alpha$ was taken from the mandrel. F_T is the force of the fibre tension. The resulting force pointing inwards to the mandrel is F_R as seen on the right side of Figure 4.11. The angle β follows from $d\alpha$.

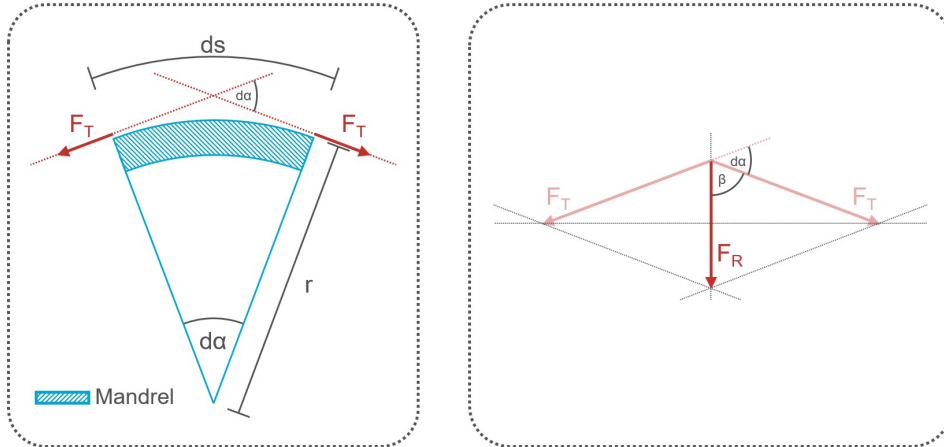$$\beta = \frac{\pi - d\alpha}{2} = \frac{\pi}{2} - \frac{d\alpha}{2}$$

Figure 4.11: Small portion $d\alpha$ of the mandrels cross-section with forces from the fibre tension F_T and the resulting inward-facing force F_R

With that, F_R can be expressed with F_T.

$$F_R = 2cos\left(\beta\right)F_T \tag{4.2}$$
$$= 2cos\left(\frac{\pi}{2} - \frac{d\alpha}{2}\right)F_T$$
$$= 2sin\left(\frac{d\alpha}{2}\right)F_T$$

The pressure would be F_R/A. However, as depth is taken out of consideration, only F_R/ds is left. ds is given by the fractional circumference of a circle. Hence, for F_R/ds the following can be written:

$$\frac{F_R}{ds} = \frac{2 sin \left(\frac{d\alpha}{2}\right) F_T}{\frac{d\alpha}{2\pi} 2\pi r} \tag{4.3}$$

When $d\alpha$ is infinitely small, it can be assumed that

$$sin\left(\frac{d\alpha}{2}\right) = \frac{d\alpha}{2}$$

Inserting this in Equation 4.3 results in

$$\frac{F_R}{ds} = \frac{2 \frac{d\alpha}{2} F_T}{\frac{d\alpha}{2\pi} 2\pi r} \tag{4.4}$$

$$\frac{F_R}{ds} = \frac{F_T}{r}$$

This shows that the pressure resulting from the fibre tension is inversely proportional to the radius. Hence, with increasing radius, the pressure decreases. Larger mandrels are thus effective in decreasing the pressure at the interface of laminate and mandrel. Based on the earlier conclusions, this also reduces the pressure drop and the spread in FVF. Nevertheless, the observed gradients in FVF in the small specimens of this thesis are significant enough to remain relevant even for larger diameters, but at a reduced scale.

4.4. Manufacturing Process Guideline for Minimised FVF Spread

In subsequent research, a conclusion must be reached as to whether a gradient in the FVF along the thickness indeed has a negative influence on the initiation or propagation of microcracks. If that is the case, or if for other reasons such as certifiability or mechanical properties a gradient is not desired, the conclusions of the performed study provide insight into how the FVF gradient can be influenced and eventually reduced. This was the research question posed in the Introduction. For convenience, it is repeated below:

How do changes in manufacturing parameters affect the gradient of the fibre volume fraction along the cross-section of curved laminates?

The conclusions gathered during the Discussion chapter can be combined in a condensed and simplified way in Figure 4.12. This figure provides a summarised answer to the research question by showing the qualitative relations between changes in the studied parameters and the influence level on measurable effects, which are the maximum pressure, the pressure drop and the spread in FVF. The spread in FVF is a distinct indicator for the gradient in FVF as referred to in the research question. The presented relations can serve as a manufacturing process guideline to choosing the type of resin, cure cycle and mandrel material for the design of new CFRP-tanks under the aspect of minimised gradients in FVF.

	Maximum Pressure	Pressure Drop	Spread in FVF
Resin with higher viscosity[1]	↗ ★★★	↘ ★★★	↘ ★★★
Resin with quicker gelation response[2]	↗ ★★★	↘ ★★★	↘ ★★★
Curing at lower temperature	↗ ★★☆	↘ ★☆☆	↘ ★☆☆ [3]
Mandrel with lower CTE	↘ ★★☆	↘ ★★☆	↘ ★★☆
Winding with higher fibre tension	→ ☆☆☆	→ ☆☆☆	→ ☆☆☆
Mandrel with larger diameter	↘ 4	↘ 4	↘ 4

Influence on the effect

↗ Increasing

↘ Reducing

→ No influence

Degree of influence

★☆☆ Low

★★☆ Medium

★★★ High

Footnotes

[1] Referring to the resin viscosity profile

[2] Resin with low gel times even at lower temperatures

[3] Untouched potential: Optimisation of cure cycle is likely to increase the degree of influence

[4] Not experimentally proven. Only analytical consideration

Figure 4.12: Qualitative interactions between selected manufacturing parameters and effects related to the gradient in FVF.

5

Conclusion

The manufacturing process of rotational-symmetric CFRP-components, specifically the autoclave curing process, can induce a significant gradient in the FVF across the laminate thickness. This gradient is driven by the thermal expansion of the mandrel which creates tension in the fibres wound in a circumferential direction and a contact pressure at the interface between the mandrel and the laminate. If the parameters of the process are an unfavourable combination, then this tension releases itself by inducing a resin flow in the direction of the thickness. As a result, the cured laminate has an FVF gradient along the thickness with high FVF close to the mandrel and lower FVF away from the mandrel. Quantifying the spread in FVF is highly dependent on how local or global the spread is measured. A suitable scale is reached by averaging the graphs of the FVF gradient such that intra-ply deviations are flattened and only the trends on the laminate level become apparent. In this case, spreads between the minimum and maximum FVF of up to 7.4%pt. can be observed.

The experimental study presented in this thesis has demonstrated that the most influential parameter is the rheological behaviour of the resin system. Resin systems with low viscosities at high temperatures and long gelation times at high temperatures result in the highest spread in FVF. The second most influential parameter is the choice of mandrel material. Materials with high coefficients of thermal expansion increase the tension in the fibres. Curing the components in an adapted autoclave cycle characterised by lower temperatures but longer holding phases proved to reduce the spread in FVF. In this study, this variation had the least impact. However, the potential to increase the impact is very high as the used cycle was not optimised with the data from the rheology measurements and differential scanning calorimetry yet due to the unavailability of the data at the time of the autoclave cycle. The pre-tension of the fibres applied during winding was found to be not correlated with the gradient in FVF.

The methodology developed and implemented in this study involved a simplified and scaled specimen geometry, representing the single-curved cylindrical section of a liquid hydrogen tank. For specimen production, a dedicated manufacturing rig was designed capable of producing specimens with controlled variations in the prepreg material, the autoclave cycle, the mandrel material and the fibre pre-tension. The Tekscan FlexiForce sensors implemented at the mandrel-laminate interface provided valuable insights into the changes in contact pressure during the autoclave cycle, where process observations are usually difficult due to the hostile environment and limited accessibility. The pressure readings were closely related to the resin

flow and therefore allowed for straightforward conclusions about the phenomenology of the resin flow in thickness direction. Limitations in the reliability of the absolute numerical values were noted due to challenges in the sensor calibration for the desired use case underneath a prepreg laminate. Furthermore, the sensor needed an extensive conditioning process before implementation in the laminate. During the study, the conditioning prior to the autoclave cycles was insufficient and the full conditioning was only achieved after the first autoclave cycle of each sensor. The measurement quality improved when the sensor was used for the second time. Despite these limitations, the qualitative data obtained from the sensors were crucial in understanding the resin flow dynamics and their impact on the final FVF distribution.

The conclusions drawn from the presented study confirm the applicability of Darcy's equation as claimed in the theoretical resin flow models of Tzeng (1988) and Calius and Springer, Lee and Springer and Calius et al. (1990). However, the observed influence of the winding tension on the pressure measurements as observed by Pérès et al. (2017) was not confirmed. Instead, the parameters mentioned above were found to be more influential.

The presented study reveals the discrepancies between a theoretically perfect design and the actual manufactured parts. Inhomogeneities induced during the manufacturing phase such as the gradient in FVF were not considered during the design phase. Considering that prepreg systems are usually tuned to FVFs of $\pm1\%$pt. the observed spreads are significant. One question which remains from this study would be to investigate whether the gradient in FVF has an effect on the mechanical performance or permeability of the laminate. The extent to which the gradient accelerates the initiation and propagation of microcracks is important information, as microcracks compromise the tank's ability to safely store liquid hydrogen and would be unacceptable in the highly safety-sensitive aviation environment. As the aviation industry moves towards decarbonization, hydrogen seems to be the most promising energy carrier to fulfil goals for sustainability. The insights gained from this study contribute to the broader effort of developing safe, efficient, and sustainable storage solutions for liquid hydrogen, which is a key component in the fight against climate change.

This study highlights the importance of accounting for manufacturing-induced inhomogeneities in composite materials and provides practical advice that will aid in the development of more reliable hydrogen storage solutions. As the world continues to search for sustainable alternatives to fossil fuels, the findings of this thesis could play a small but eventually significant role in ensuring safety in light-weight hydrogen storage technologies.

<div align="right">

6

</div>

Recommendations for Future Work

Throughout the execution and evaluation of this study, multiple topics were touched upon which are outside the scope of this master's thesis but could potentially be topics for future work. This chapter briefly outlines possible directions and potentials of those topics.

Micrograph Classification and Heat-map Algorithm Enhancements   The classification and heat-map generation algorithm was a core part of the methodology for analysing the micrographs. However, as noted already during the evaluation of the results, this algorithm has some disadvantages that could be eliminated in the further development of this algorithm. Firstly, the machine-learning based model was unable to correctly classify micrographs made from Teijin Q183 because the training database did not seem to be sufficient. In the next training iteration of the model, more training data showing Teijin Q183 micrographs should be included to allow for a reliable recognition of those micrographs. Secondly, the heat-maps had the inherent flaw that the local FVF on the heat-map rapidly decreases when getting closer to the edges of the micrograph of the image. This did not represent the reality as the FVF had already dropped when the end of the micrograph was not yet reached. The algorithm should be able to recognise the micrograph edge and adjust the region taken into account for calculating the local FVF.

Investigation of Other Parameters   Due to constrains in time and resources, the variation of parameters in this work had to be limited to four parameters (i.e. material, autoclave cycle, mandrel material and fibre tension). However, the variation of other parameters could yield similarly useful results. While this study tested only UD stackings, apart from one cross-ply specimen, more complex stackings will be used in cryogenic hydrogen tanks. The influence of this on the resin flow can be determined by future studies. Only the component in the circumferential direction causes the contact pressure that drives the resin flow. The resin of plies in a different orientation, however, could still contribute to the resin flow when they experience pressure from plies above them as it was the case for the single cross-ply specimen of this study. Furthermore, the stacking sequence might also impact the permeability of the fibre grid which in turn influences the resin flow rate based on Darcy's equation. For this it would also be important to study the gradient of pressure along the laminate's thickness by

implementing more sensors between different plies along the thickness. At a later stage the contact pressure and resin flow in more complex specimens with conical and double curvature surfaces should be investigated so as to draw conclusions about the dome section of the cryogenic hydrogen tank as well.

High Compressive Stresses at Mandrel-Laminate Interface   Even though no absolute number was given for the contact pressure between the mandrel and the laminate, it became apparent that the laminate was subjected to high transverse compressive loads. This has the potential to cause damage to the matrix system and requires deeper investigation.

Strain Amplification   This study described the resin flow during the autoclave curing cycle. The resin flow is a time-limited phenomenon. The resin flow stopped for two reasons: because the resin either gelled and could not flow anymore due its high viscosity or because the maximum amount of resin was already squeezed out and the fibres were already in direct contact with the adjacent fibres. When the second case occurs, a concern is that the laminates transverse tensile strength decreases. In transverse loading, the strains are carried mostly by the resin between the fibres. The closer the fibres get to each other the higher the stress concentrations on the resin between the fibres. This leads to a reduction in transverse tensile strength which is referred to as strain amplification by Schürmann (2005). Further investigations are required to assess the impact of these stress concentrations and the reduced transverse tensile strength in cryogenic hydrogen tanks. For such an investigation, it would be crucial to quantify the distance between the centre points of adjacent fibres in a micrograph where the distance equals exactly one fibre diameter the fibres are just touching each other. The machine-learning based classification algorithm used to create the heat-maps as developed by Naumann (2024) has the potential to provide the necessary image recognition tools by automatically detecting all fibre centre points in a micrograph and to measure the distances to the adjacent fibres. This would allow for an evaluation of how susceptible a specimen which experienced significant resin flow is to the strain amplification effect and how this impacts the mechanical performance and microcrack behaviour of a cryogenic hydrogen tank.

Optimisation of Adapted Autoclave Cycle   The adapted autoclave cycle resulted in a significant reduction of the FVF gradient. This occurred despite the fact that the cycle had not yet been fully optimised. More insights into cure and rheology behaviour are needed for this optimisation. Additional DSC measurements are suggested which follow the cycle with a plateau at a lower temperature to determine the required duration to cure the material. Instead of a plateau at a constant low temperature, a slowly increasing temperature ramp is a suggestion that would be more tailored to the increase in the glass transition temperature with the progressing cycle and could reduce the cycle time while reaching the same result. Repetition of the rheology measurement for such an adapted cycle could determine the moment of gelation. As the resin flow stops at this point, the temperature could be increased to the regular recommended temperature once gelation is passed to speed up the cycle. The precise temperatures, temperature gradients, and duration must be determined, taking into account the curing behaviour, rheology, and thermal expansion of the mandrel. This could be studied in another experimental study or using a suitable theoretical model. However, in each of these considerations, the challenges of certification must be taken into account. The applied cure cycle deviates from the cycle that was used to certify the material. Therefore, it must be proven that the adapted cycle does not deteriorate the properties of the material.

In-line Process Monitoring with Pressure Sensors   The piezoelectric pressure sensors implemented between the laminate and mandrel delivered crucial data during the autoclave cycle without significantly impacting the CFRP-component quality. After demoulding, only a minor imprint of the sensor's outline remained on the component. This opens up the potential for the sensor to be used for in-line cure monitoring during curing of rotational symmetric components. If the resin rheology and cure kinetics are known, it is possible to use either the pressure curve or the more distinct pressure drops to identify when a certain degree of cure is reached. Additionally, the sensor could be used to identify manufacturing flaws such as missing plies, wrong layups or inferior material deposition quality as these should all lead to different pressure graphs. Furthermore the pressure data could already be used in the material deposition phase to build an in-line quality monitoring system that measures and validates the AFP endefectors compression force. However, for these potential applications the sensor and its correct deployment must be better understood. One challenge faced during this study was the senor calibration that needed to be tailored to the use-case underneath a laminate in order to achieve accurate absolute pressure data in future measurements. The reason why the sensors performed better in and after their second autoclave cycle should also be investigated. If the hypothesis of insufficient sensor conditioning turns out to be true, the next question would be how a sufficient conditioning can be reached outside of the autoclave.

References

Air, A., Shamsuddoha, M., & Prusty, B. G. (2023). A review of Type V composite pressure vessels and automated fibre placement based manufacturing. *Composites Part B: Engineering, 253*, 110573.

Airbus Deutschland GmbH et al. (2003). *Liquid Hydrogen Fuelled Aircraft - System Analysis* (CRYOPLANE).

Arrabiyeh, P. A., Dlugaj, A. M., Eckrich, M., & May, D. (2024). Designing an End Effector and a Thickness Adaptive Compression Molding Process for Wet Fiber Placement. *Applied Composite Materials*.

Arrhenius, S. (1889). Über die Dissociationswärme und den Einfluss der Temperatur auf den Dissociationsgrad der Elektrolyte. *Zeitschrift für Physikalische Chemie, 4U*(1), 96–116.

Azeem, M., Ya, H. H., Alam, M. A., Kumar, M., Stabla, P., Smolnicki, M., Gemi, L., Khan, R., Ahmed, T., Ma, Q., Sadique, M. R., Mokhtar, A. A., & Mustapha, M. (2022). Application of Filament Winding Technology in Composite Pressure Vessels and Challenges: A Review. *Journal of Energy Storage, 49*, 103468.

Bahar, M., & Sinapius, M. (2020). Adaptive Feeding Roller with An Integrated Cutting System for Automated Fiber Placement (AFP). *Journal of Composites Science, 4*, 92.

Bakhshi, N., & Hojjati, M. (2020). Effect of compaction roller on layup quality and defects formation in automated fiber placement. *Journal of Reinforced Plastics and Composites, 39*, 3–20.

Calius, E., Lee, S.-Y., & Springer, G. (1990). Filament Winding Cylinders: II. Validation of the Process Model. *Journal of Composite Materials, 24*, 1299–1343.

Calius, E., & Springer, G. (1990). A model of filament-wound thin cylinders. *International Journal of Solids and Structures, 26*, 271–297.

Carman, P. C. (1937). Fluid flow through granular beds. *Chemical Engineering Research and Design*, 32–48.

Carman, P. C. (1956). Flow of gases through porous media. *(No Journal Title)*.

Castro, J., & Macosko, C. (1980). Kinetics and rheology of typical polyurethane reaction injection molding systems. *Society of Plastics Engineers (Technical Papers)*, 434–438.

Darcy, H. (1856). *Les fontaines publiques de la ville de dijon: Exposition et application des principes à suivre et des formules à employer dans les questions de distribution d'eau* (Vol. 1). Victor Dalmont.

Drone Industry Insights. (2017). *Pushing the Boundaries – Drone Energy Sources*.

Ermanni, P. (2007). *Composites Technologien* (Vorlesungsskript). ETH Zürich.

Farooq, U., Sakarinen, E., Teuwen, J., Alderliesten, R., & Dransfeld, C. (2023). Synergistic Toughening of Epoxy through Layered Poly(ether imide) with Dual-Scale Morphologies. *ACS Applied Materials and Interfaces, 15*, 53074–53085.

Fleming, G. G., de Lépinay, I., & Schaufele, R. (2022). *Environmental Trends in Aviation to 2050*. International Civil Aviation Organization (ICAO).

Geng, G., Ma, X., Geng, H., & Wu, Y. (2018). Effect of thermal cycles on the thermal expansion behavior of T700 carbon fiber bundles. *Chemical Research in Chinese Universities, 34*, 451–456.

Graver, B., Zhang, K., & Rutherford, D. (2019). *CO_2 emissions from commercial aviation, 2018*.

Hahn, H. T., & Lee, S. S. (1992). *The stress development during filament winding of thick cylinders*. Pennsylvania State University.

IEA. (2019). *The Future of Hydrogen*. IEA.

IPCC. (2021). *Climate Change 2021: The Physical Science Basis. Contribution of Working Group I to the Sixth Assessment Report of the Intergovernmental Panel on Climate Change* (Vol. In Press). Cambridge University Press.

Joven, R., Ahmed, A., Tavakol, B., Das, R., Roozbehjavan, P., & Minaie, B. (2012). Study of thermal expansion in carbon fiber-reinforced polymer composites. *SAMPE International Symposium Proceedings, Charleston, SC*.

Kamal, M., & Sourour, S. (1973). Kinetics and thermal characterization of thermoset cure. *Polymer Engineering & Science*, *13*, 59–64.

Kozeny, J. (1927). Über kapillare Leitung des Wassers im Boden. *Sitzungsberichte der Akademie der Wissenschaften in Wien*, *136*.

Kwik, J. (2019). *Entwicklung eines Materialmodells zur Vorhersage von Schäden an Faserhalbzeugen während automatisierter Ablegeprozesse* (Master Thesis). DLR e.V.

Langston, T. (2016). The tensile behavior of high-strength carbon fibers. *Microscopy and Microanalysis*, *22*, 841–844.

Lee, S.-Y., & Springer, G. (1990). Filament Winding Cylinders: I. Process Model. *Journal of Composite Materials*, *24*, 1270–1298.

Liu, F., Wang, D., Liu, J., Wei, H., Zhang, H., Xu, J., Li, S., Qin, Z., Wang, R., Jia, H., & Zhang, J. (2020). Reviews on interfacial properties of the carbon fiber reinforced polymer composites. *Journal of Physics: Conference Series*, *1637*.

Mallick, P. K. (2018). *Processing of Polymer Matrix Composites*. Taylor & Francis Group.

Naumann, J. (2024, January). *Robust Detection and Explanation of Cracks in Microscopic Images* (Master Thesis). TU Braunschweig.

Pérès, P., Dupillier, J., Lynam, C., & Forghani, A. (2017). Winding process modelling - validation through spring-in prediction. *ICCM International Conferences on Composite Materials*.

Pradere, C., & Sauder, C. (2008). Transverse and longitudinal coefficient of thermal expansion of carbon fibers at high temperatures (300–2500 K). *Carbon*, *46*, 1874–1884.

Sbanca, M., Boboc, R., & Mogan, G. (2023). Fiber tensioning systems in a robotized winding procedure for composite materials building processes. *Electronics (Switzerland)*, *12*.

Schürmann, H. (2005). *Konstruieren mit Faser-Kunststoff-Verbunden*. Springer-Verlag.

Tzeng, J. T. (1988). *A model of the winding and curing processes for filament wound composites* (PhD Thesis). Virginia Polytechnic Institute and State University.

UNFCCC. (2016). *The Paris Agreement*. Paris Climate Change Conference.

Wilson, A. J. C. (1941). The thermal expansion of aluminium from $0°C$ to $650°C$. *Proceedings of the Physical Society*, *53*(3), 235.

Yakout, M., Elbestawi, M. A., & Veldhuis, S. C. (2018). A study of thermal expansion coefficients and microstructure during selective laser melting of Invar 36 and stainless steel 316L. *Additive Manufacturing*, *24*, 405–418.

A
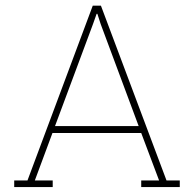
Confidential Appendix

This appendix is not meant for publication in the freely accessible version as it contains results that would contravene the agreement with Teijin for providing the material for this thesis.
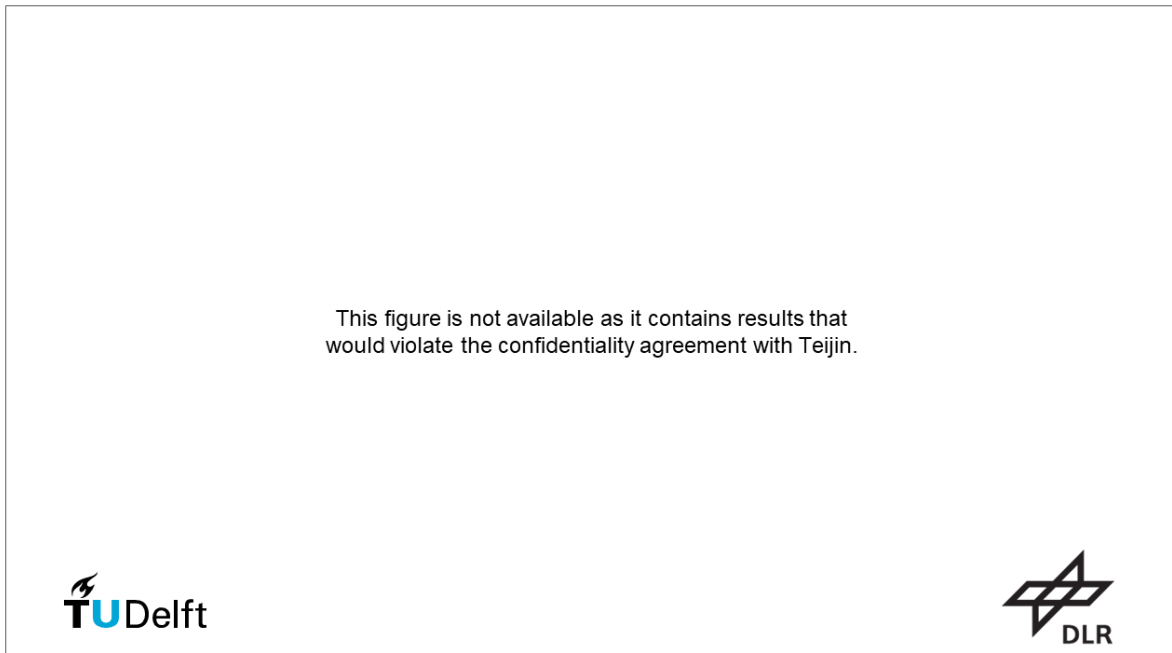
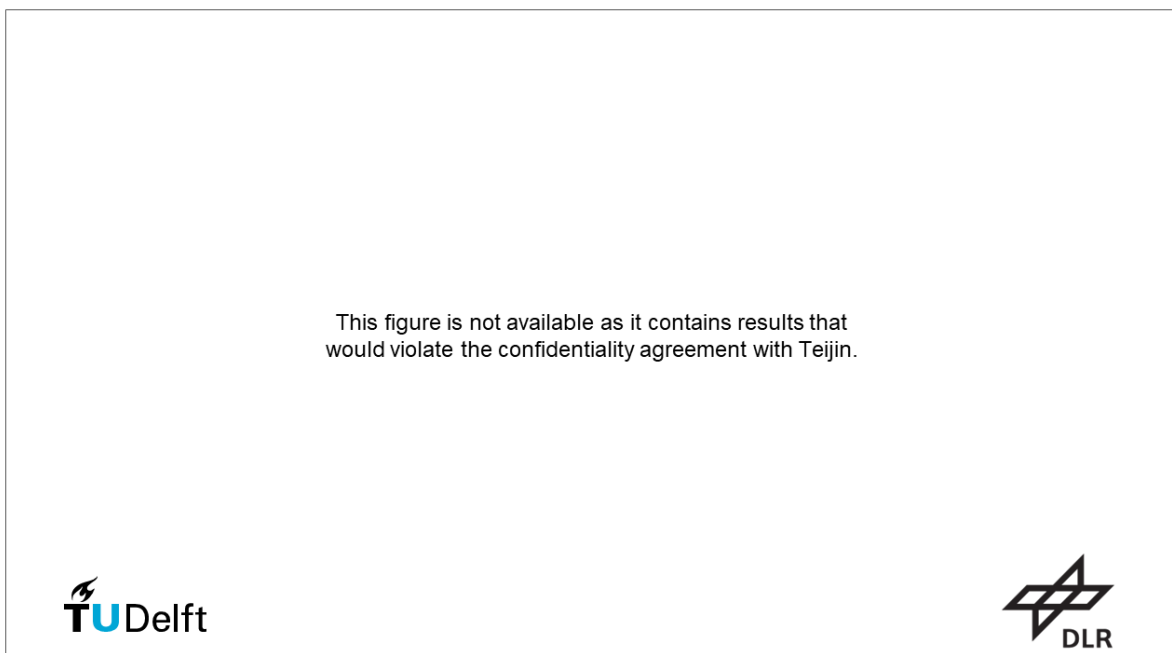**Figure A.1:** Storage and loss modulus plotted against temperature for Teijin Q183.

Figure A.2: Complex viscosity and temperature plotted against time for Hexcel 6376 and Teijin Q183.

This figure is not available as it contains results that
would violate the confidentiality agreement with Teijin.

TUDelft

DLR

Figure A.3: DSC measurement of Teijin Q183. Temperature Modulation with TOPEM®.

This figure is not available as it contains results that
would violate the confidentiality agreement with Teijin.

TUDelft

DLR
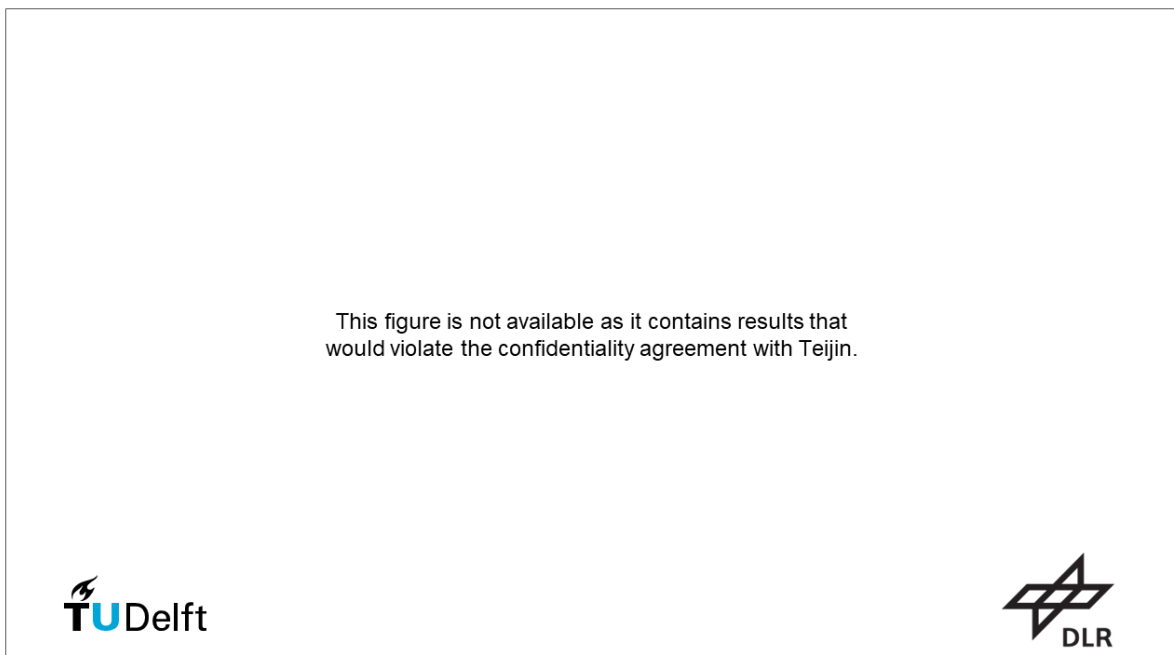
Figure A.4: TMA of Teijin Q183.

B

All Pressure & Temperature Graphs
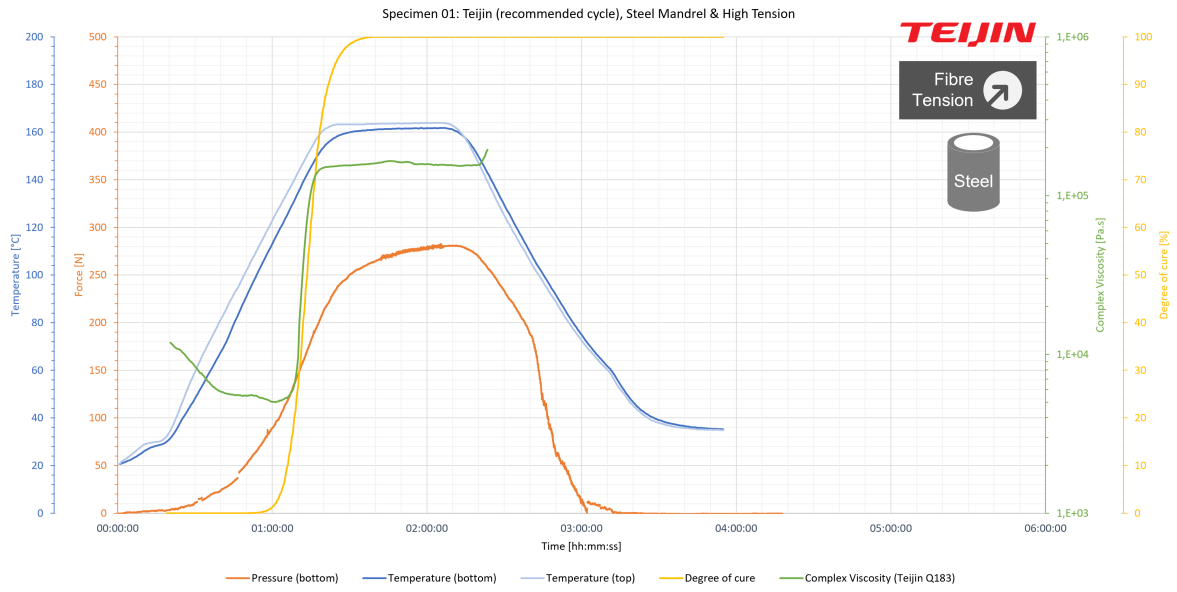
Figure B.1: Recorded data during curing of specimen 01
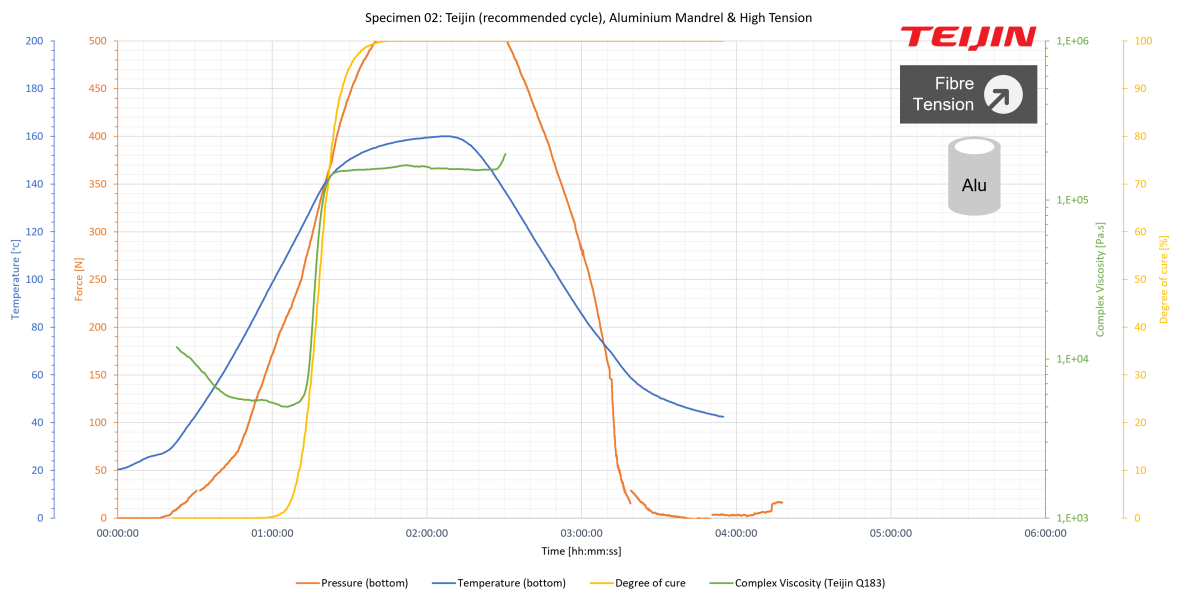
Figure B.2: Recorded data during curing of specimen 02
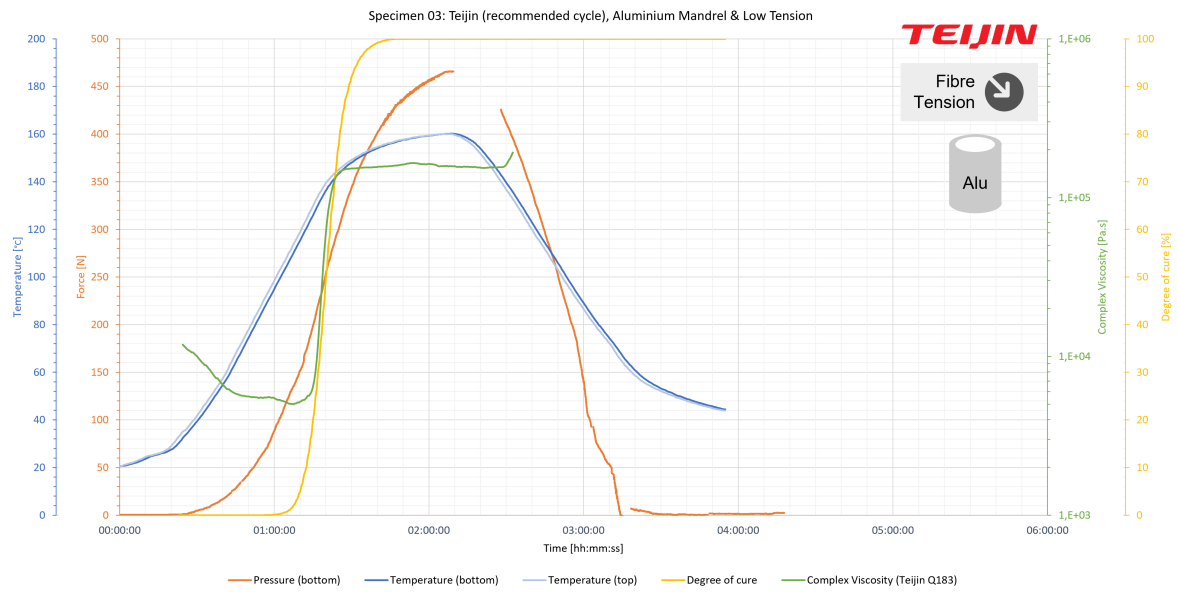
Figure B.3: Recorded data during curing of specimen 03
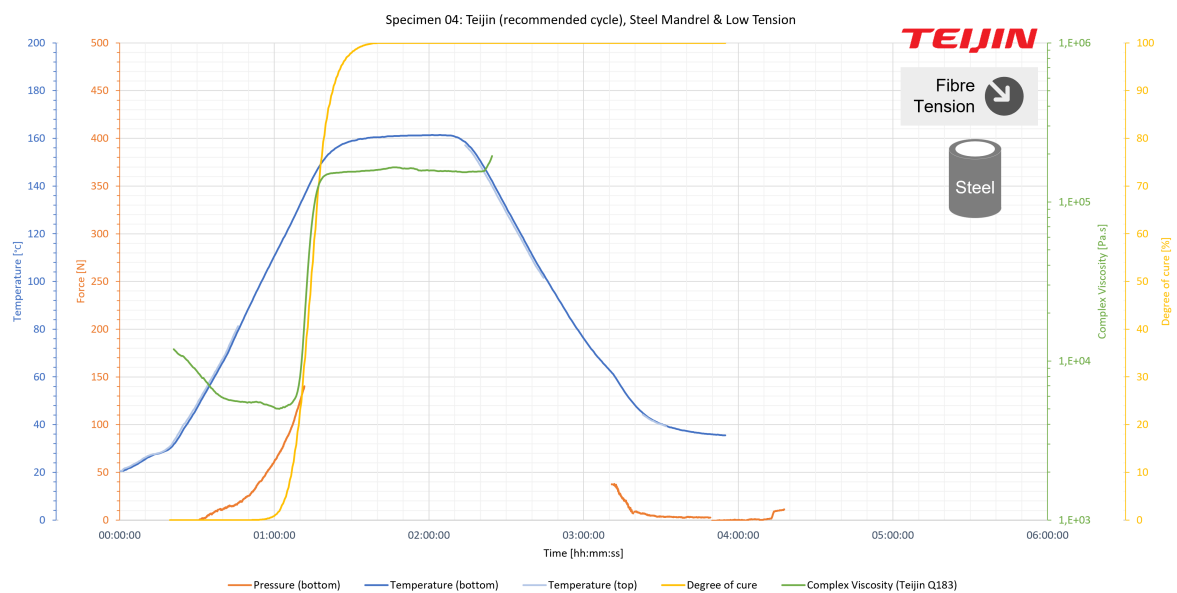
Figure B.4: Recorded data during curing of specimen 04. Due to a loose connection majority of the pressure measurement was lost.
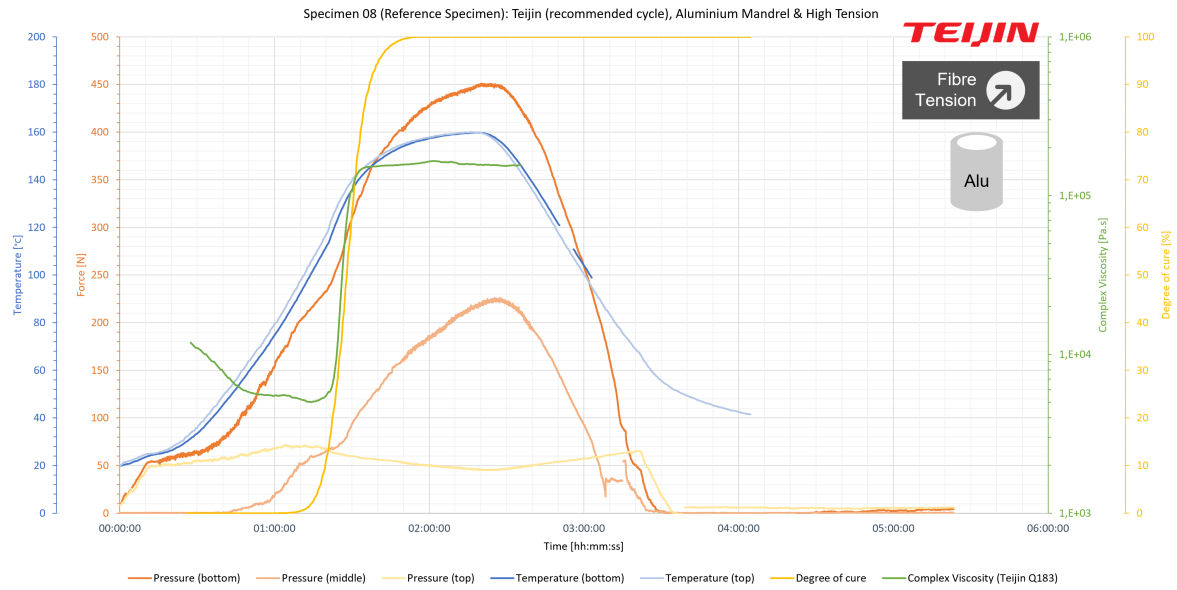
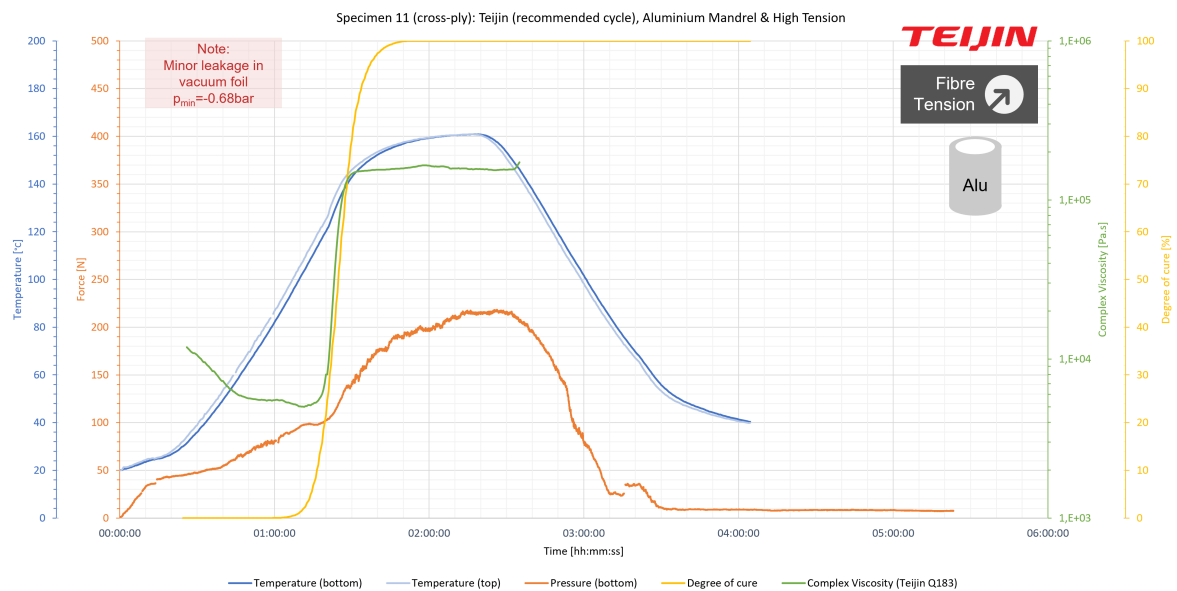**Figure B.5:** Recorded data during curing of specimen 08. In this specimen 3 pressure sensors were embedded.

Figure B.6: Recorded data during curing of specimen 11. A minor leakage in the vacuum foil occurred but vacuum was sustained throughout the process with a minimum pressure of $-0.68 bar$ compared to a nominal vacuum value of $-1 bar$.
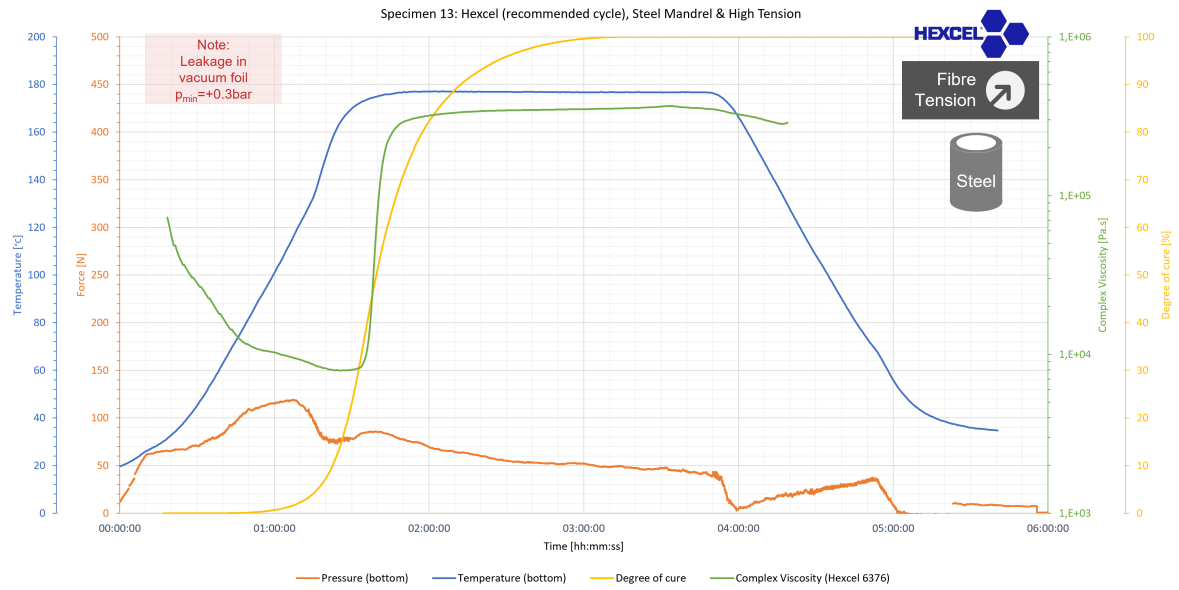
Figure B.7: Recorded data during curing of specimen 13. Leakage in the vacuum foil occurred. The leak was small enough to keep the vacuum pump running but the pressure reached $+0.3bar$ compared to a nominal vacuum value of $-1bar$.
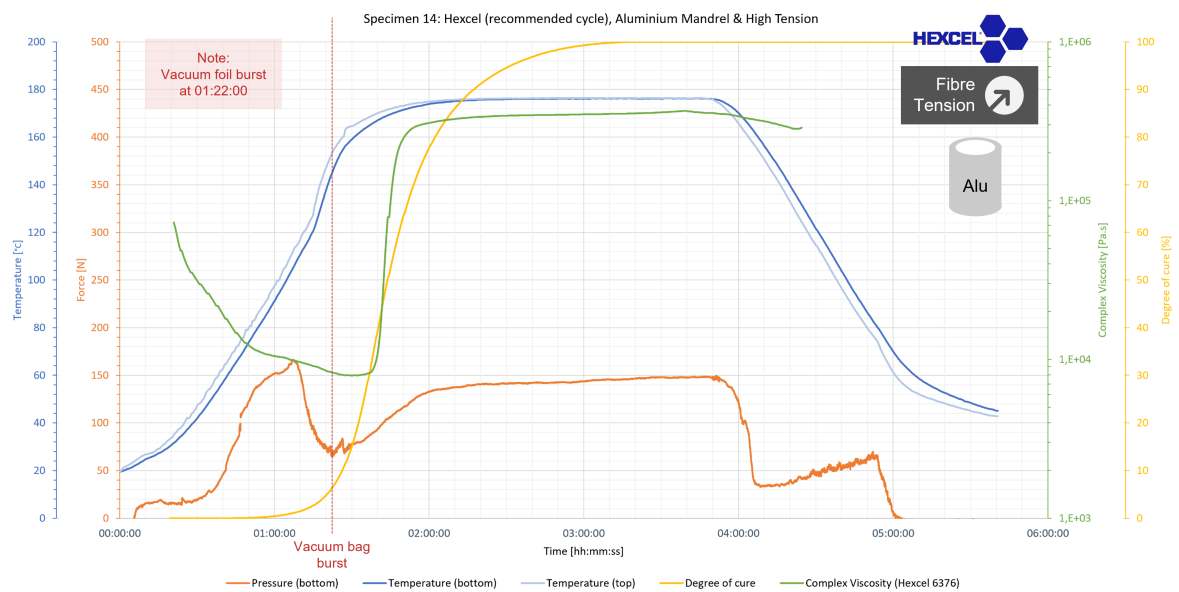

Figure B.8: Recorded data during curing of specimen 14. The vacuum foil burst at 01:22:00 and the vacuum pump had to be turned off because of that.
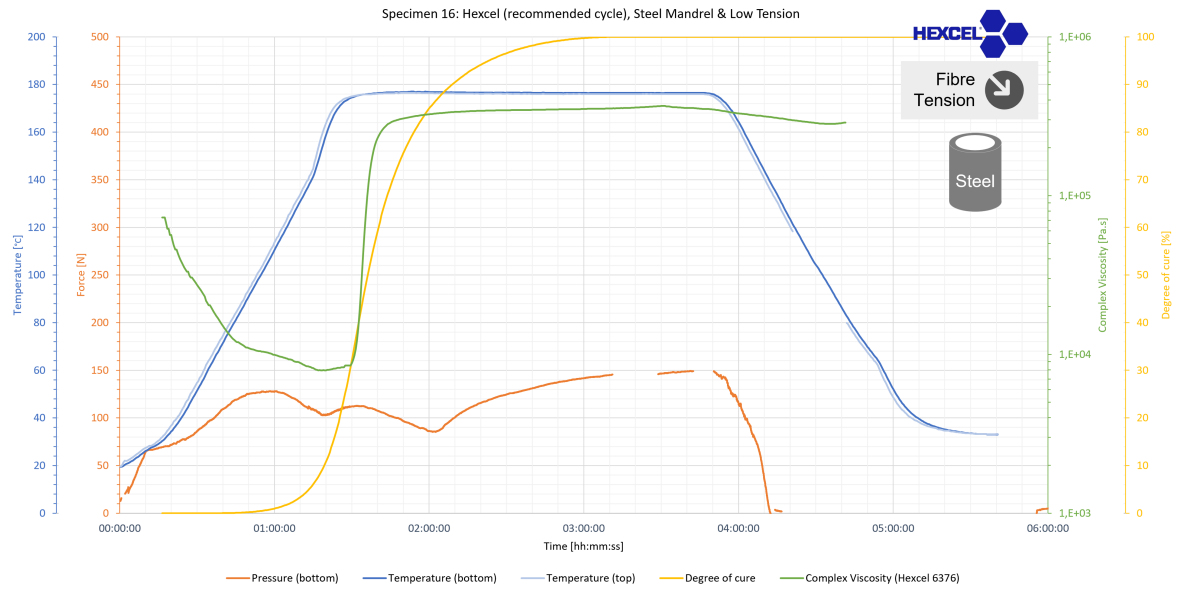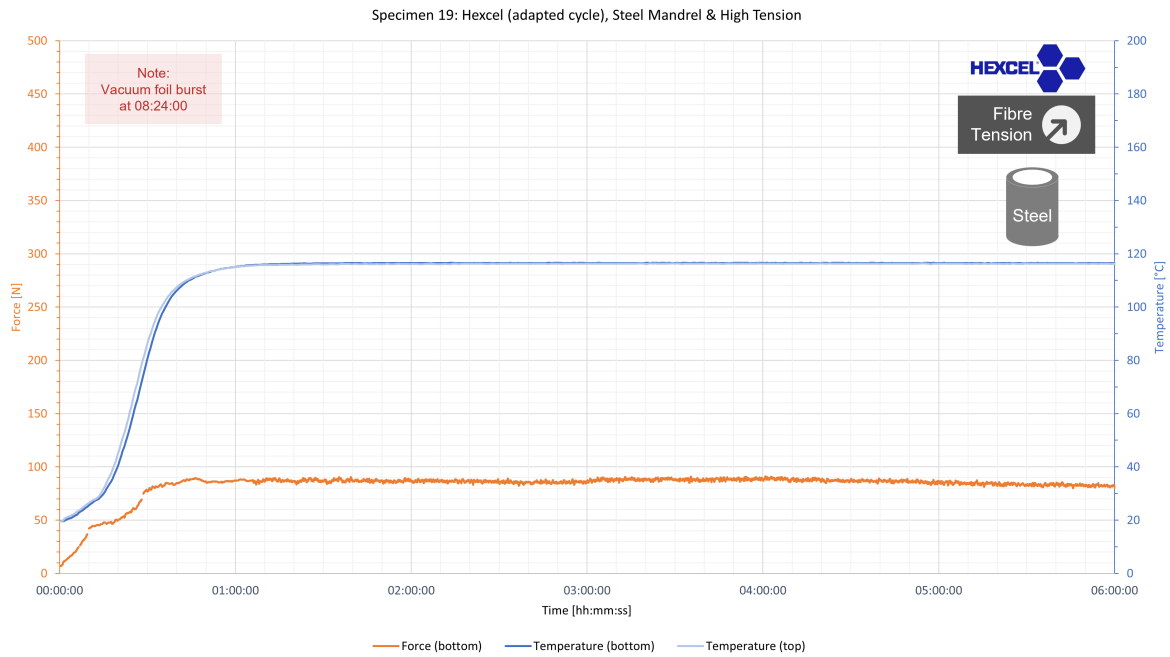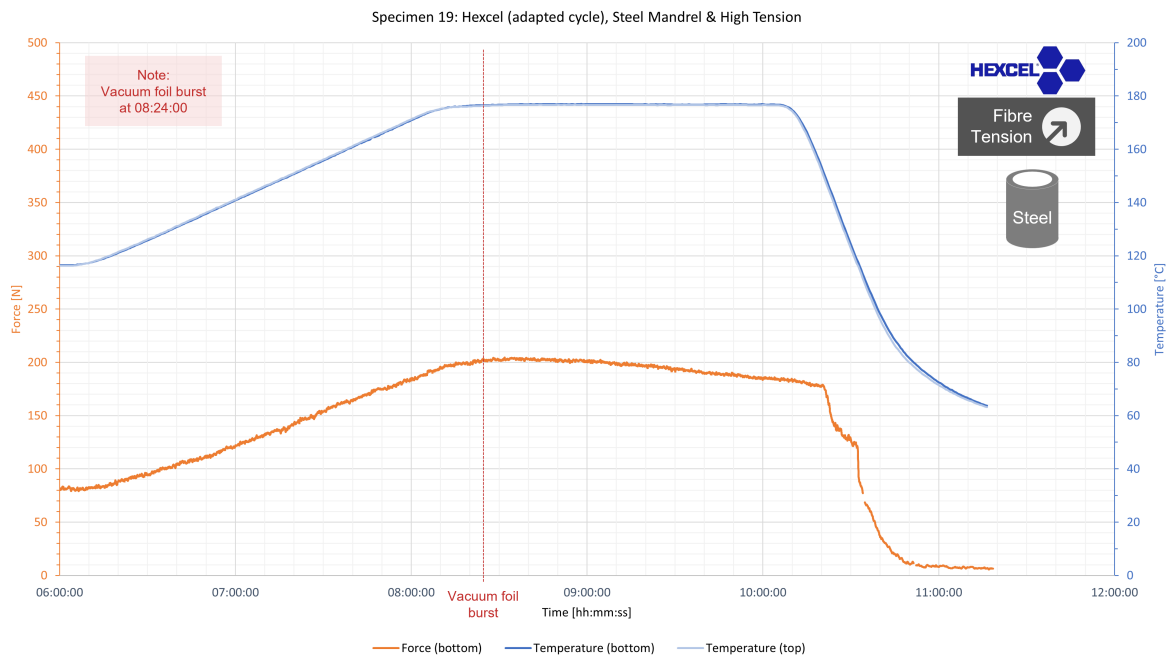
Figure B.9: Recorded data during curing of specimen 16

(a) Time from 00:00:00 to 06:00:00

(b) Time from 06:00:00 to 12:00:00

Figure B.10: Recorded data during curing of specimen 19 with the adapted cycle. For comparability the same time scale was maintained and the graph split in (a) and (b). The vacuum foil burst at 08:24:00 and the vacuum pump had to be turned off because of that. The impact on the specimen was negligible as the curing was already sufficiently advanced at this point.
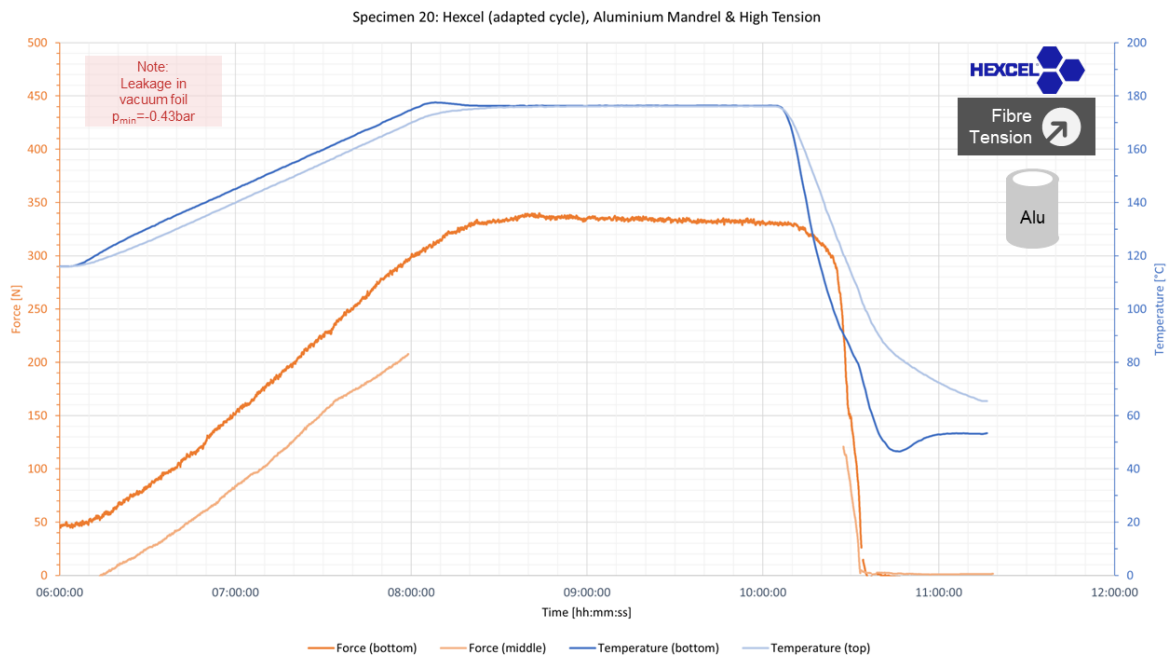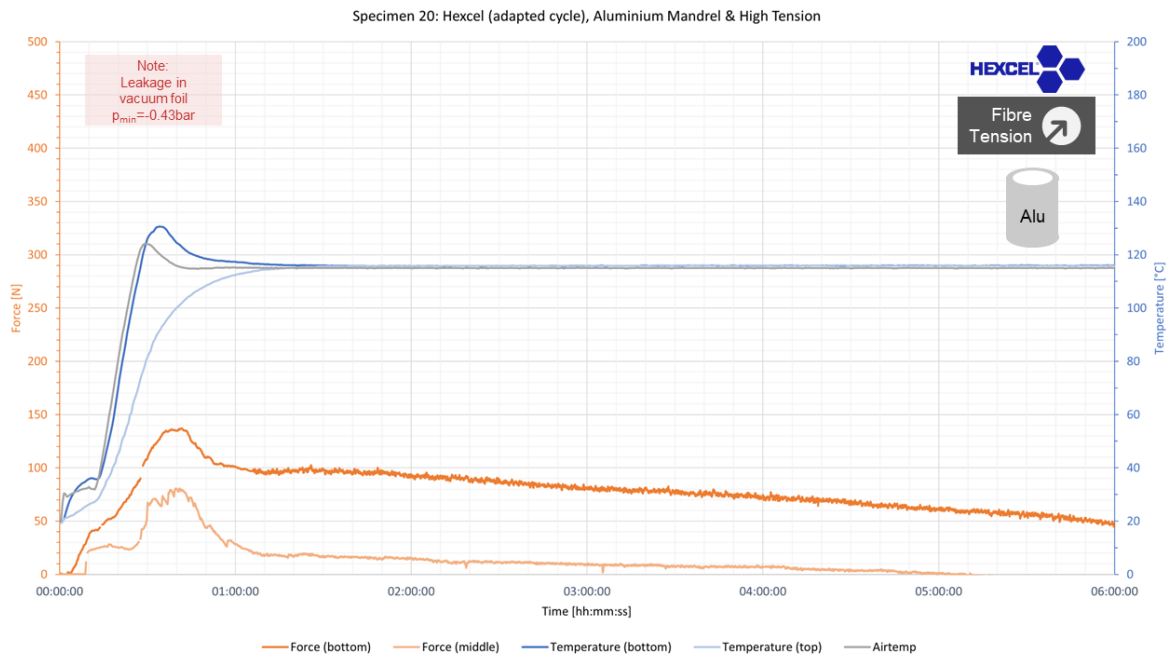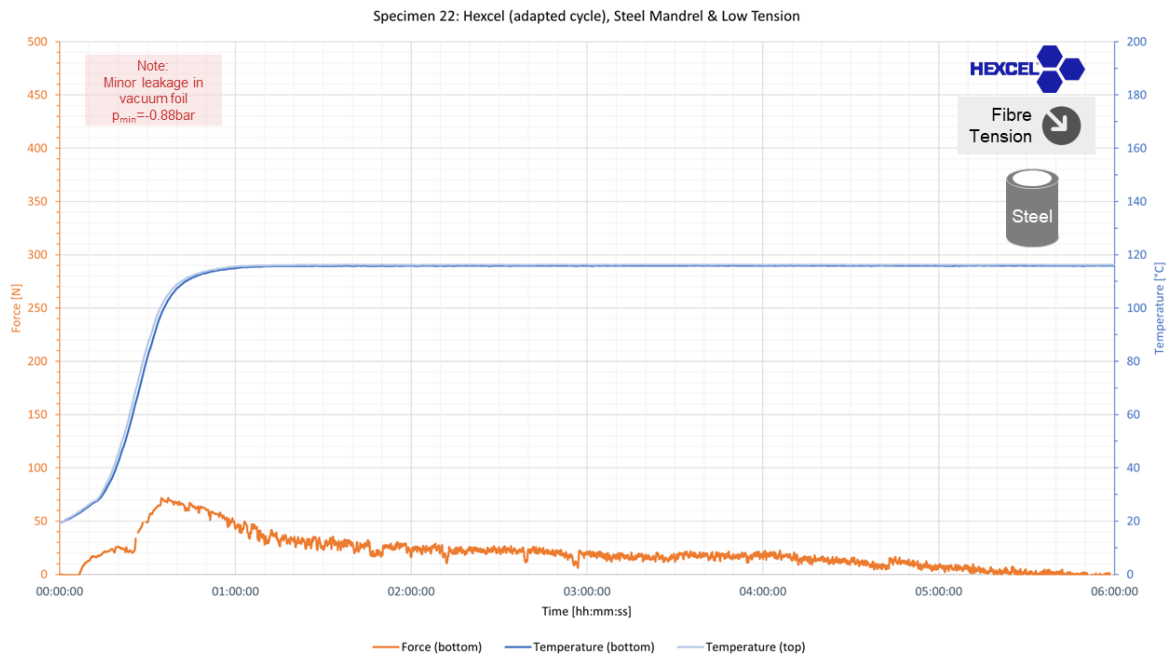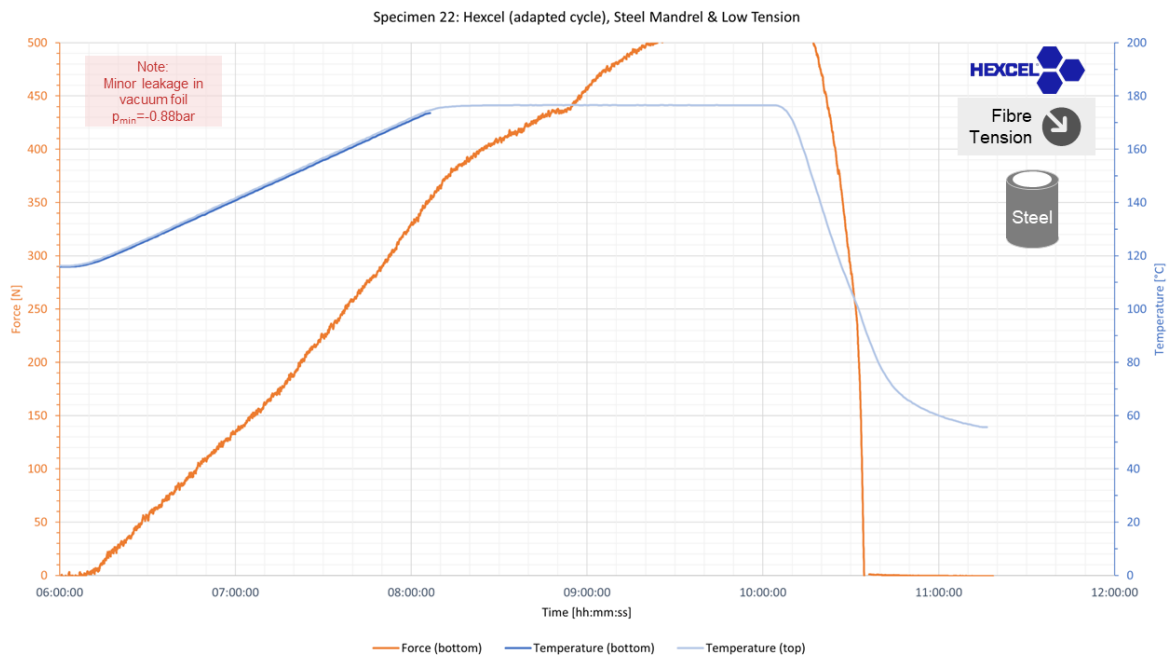
(a) Time from 00:00:00 to 06:00:00

(b) Time from 06:00:00 to 12:00:00

Figure B.11: Recorded data during curing of specimen 20 with the adapted cycle. For comparability the same time scale was maintained and the graph split in (a) and (b). A minor leakage in the vacuum foil occurred but vacuum was sustained throughout the process with a minimum pressure of $-0.43bar$ compared to a nominal vacuum value of $-1bar$. The sensors show significant signal drift and move out of the calibration range leading to negative values.

(a) Time from 00:00:00 to 06:00:00

(b) Time from 06:00:00 to 12:00:00

Figure B.12: Recorded data during curing of specimen 22 with the adapted cycle. For comparability the same time scale was maintained and the graph split in (a) and (b). A minor leakage in the vacuum foil occurred but vacuum was sustained throughout the process with a minimum pressure of $-0.88bar$ compared to a nominal vacuum value of $-1bar$. The sensor shows signal drift and temporarily moves out of the calibration range leading to negative values.
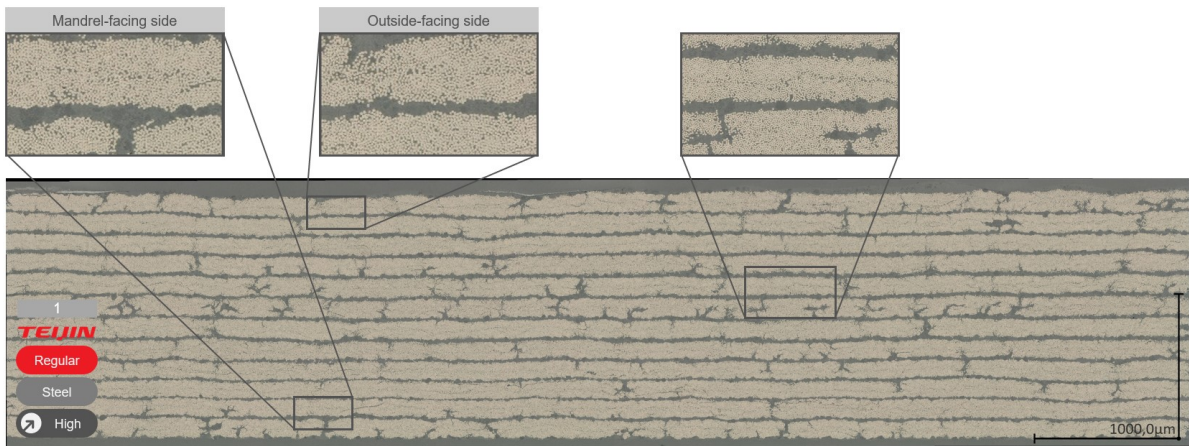
C

Micrographs

Figure C.1: Micrograph of specimen 01.

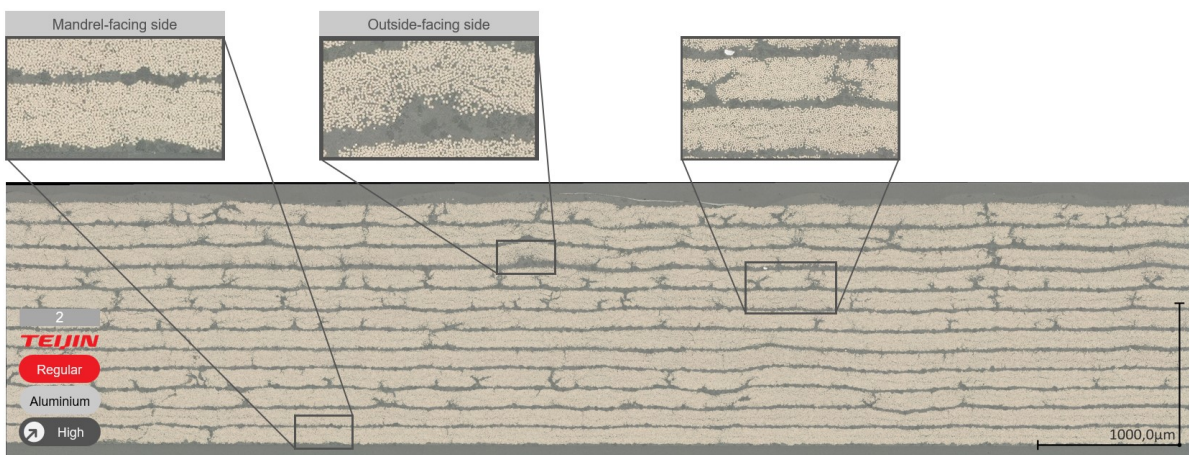**Figure C.2:** Micrograph of specimen 02.

Figure C.3: Micrograph of specimen 03.
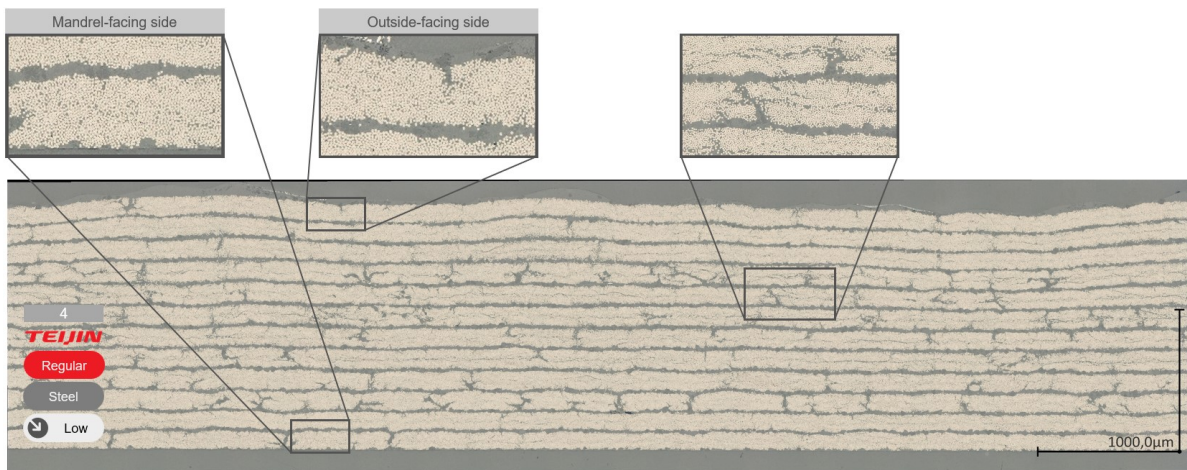
Figure C.4: Micrograph of specimen 04.
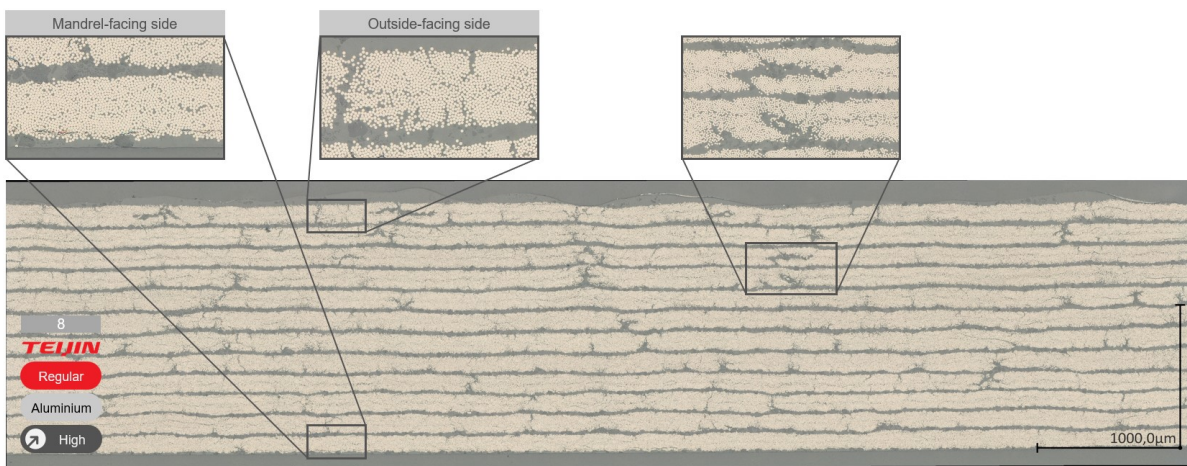
Figure C.5: Micrograph of specimen 08.
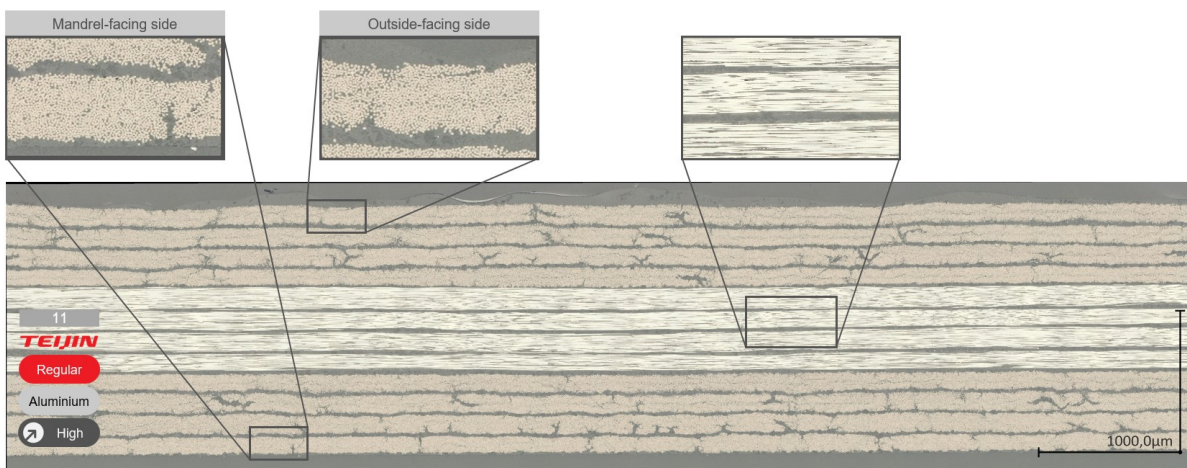
Figure C.6: Micrograph of specimen 11.

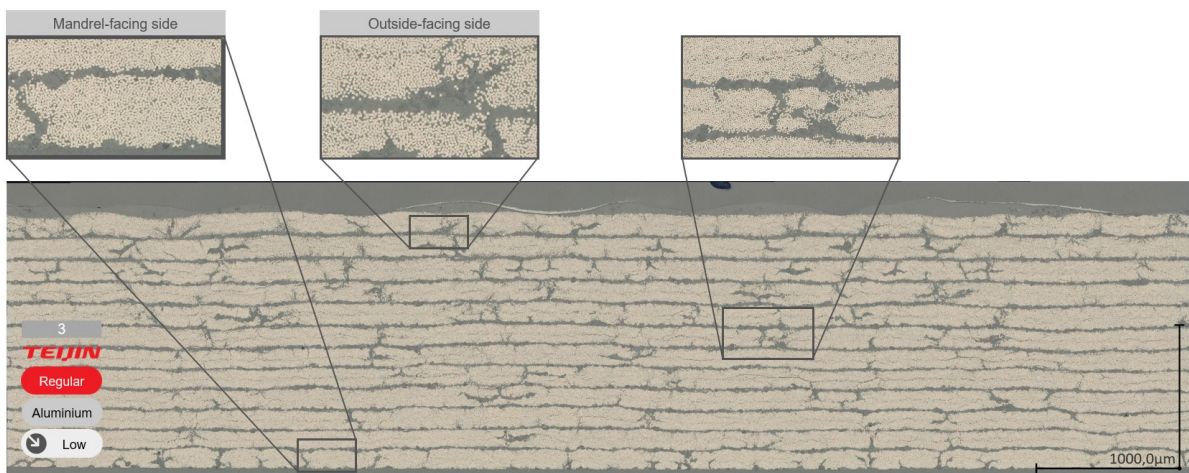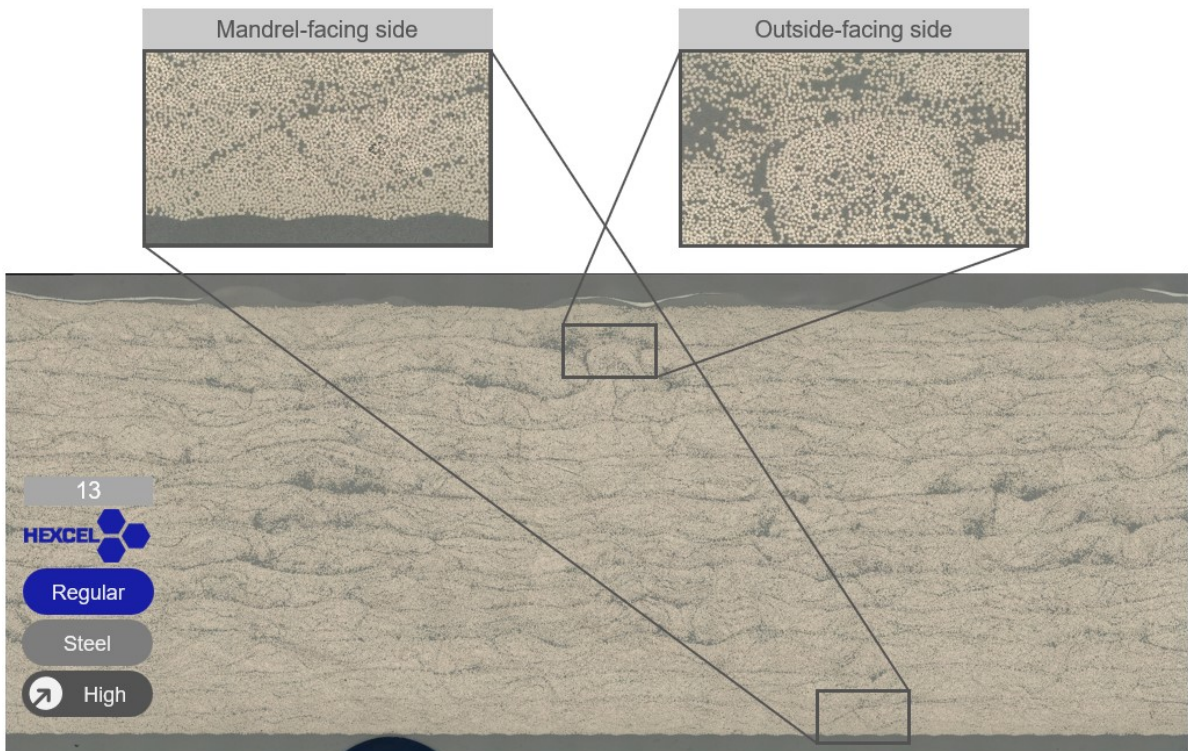**Figure C.7:** Micrograph of specimen 13.
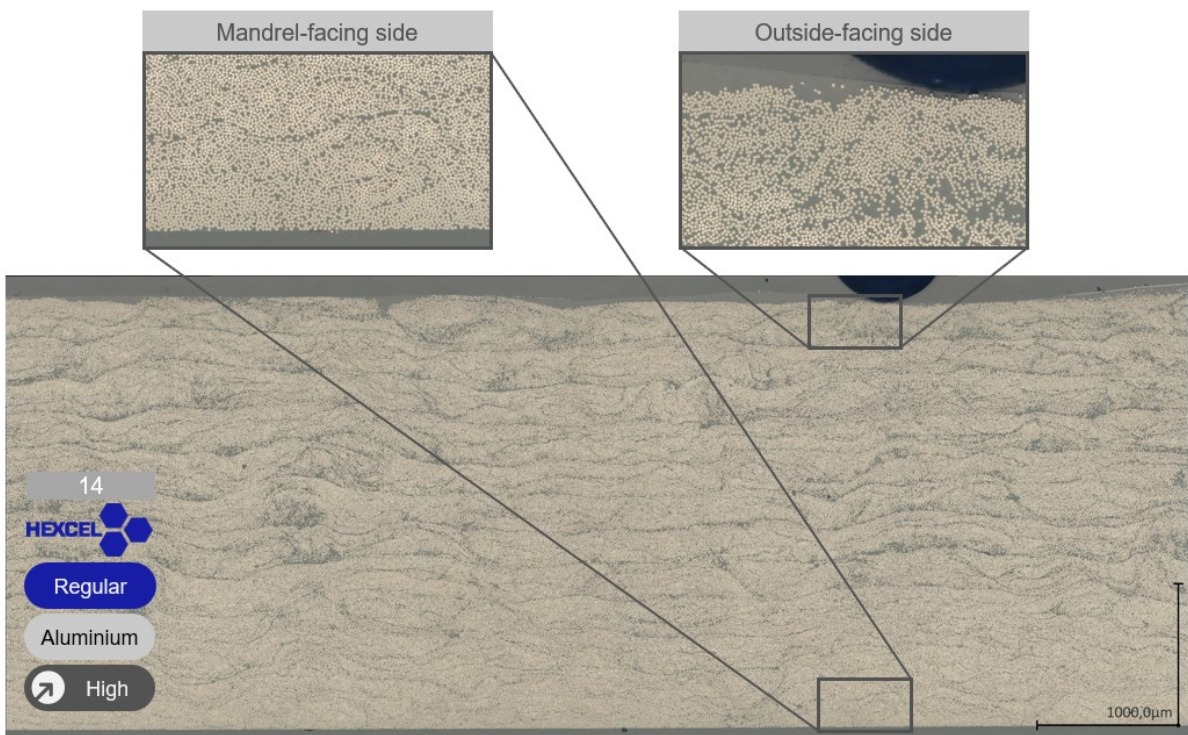
Figure C.8: Micrograph of specimen 14.
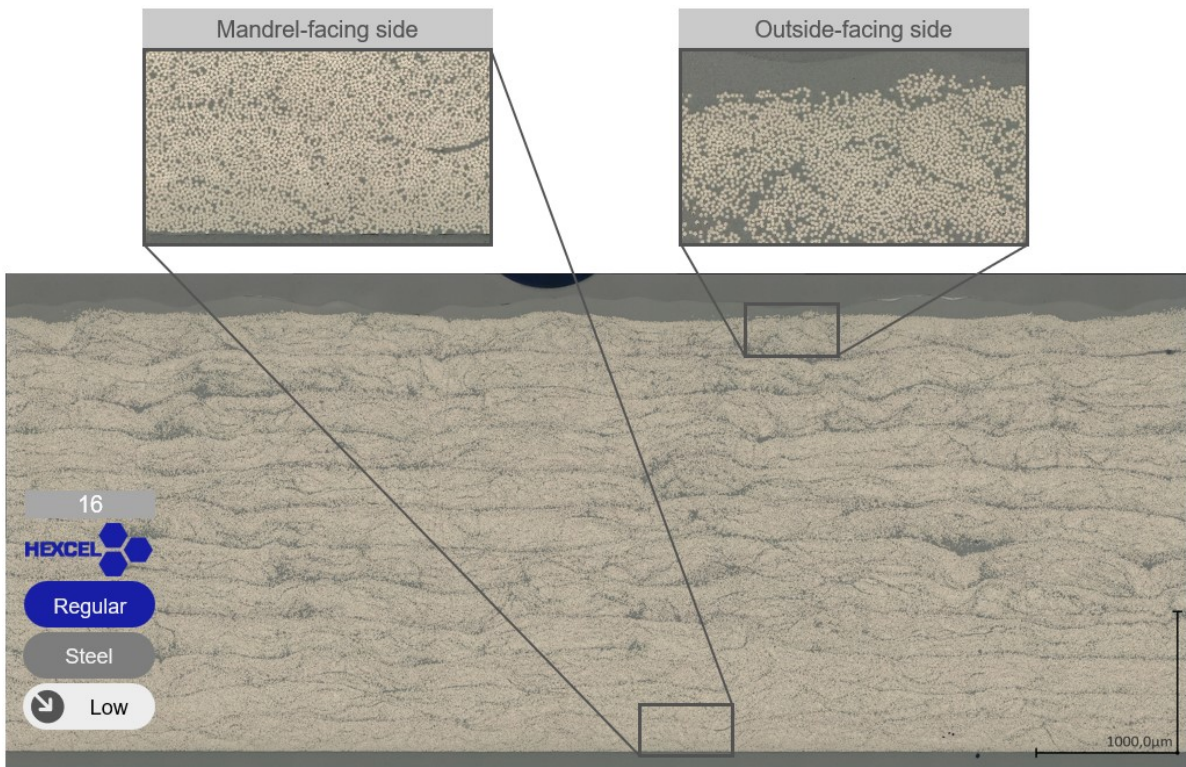
Figure C.9: Micrograph of specimen 16.
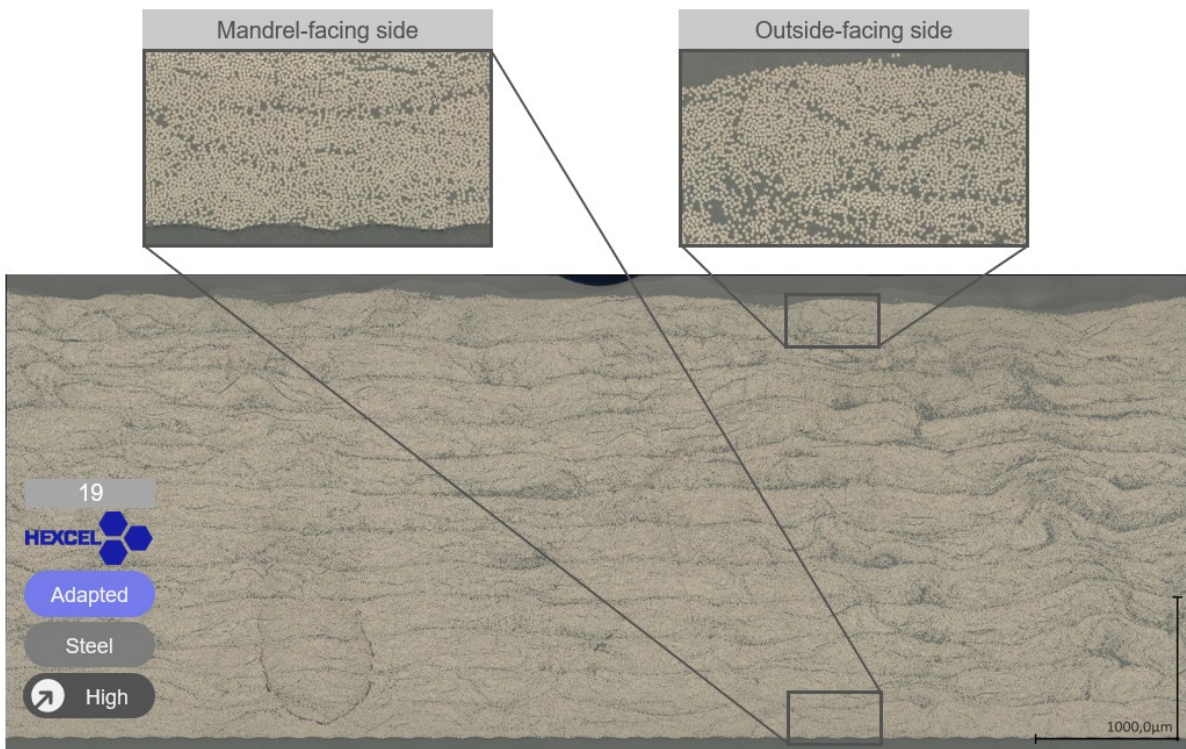
Figure C.10: Micrograph of specimen 19.
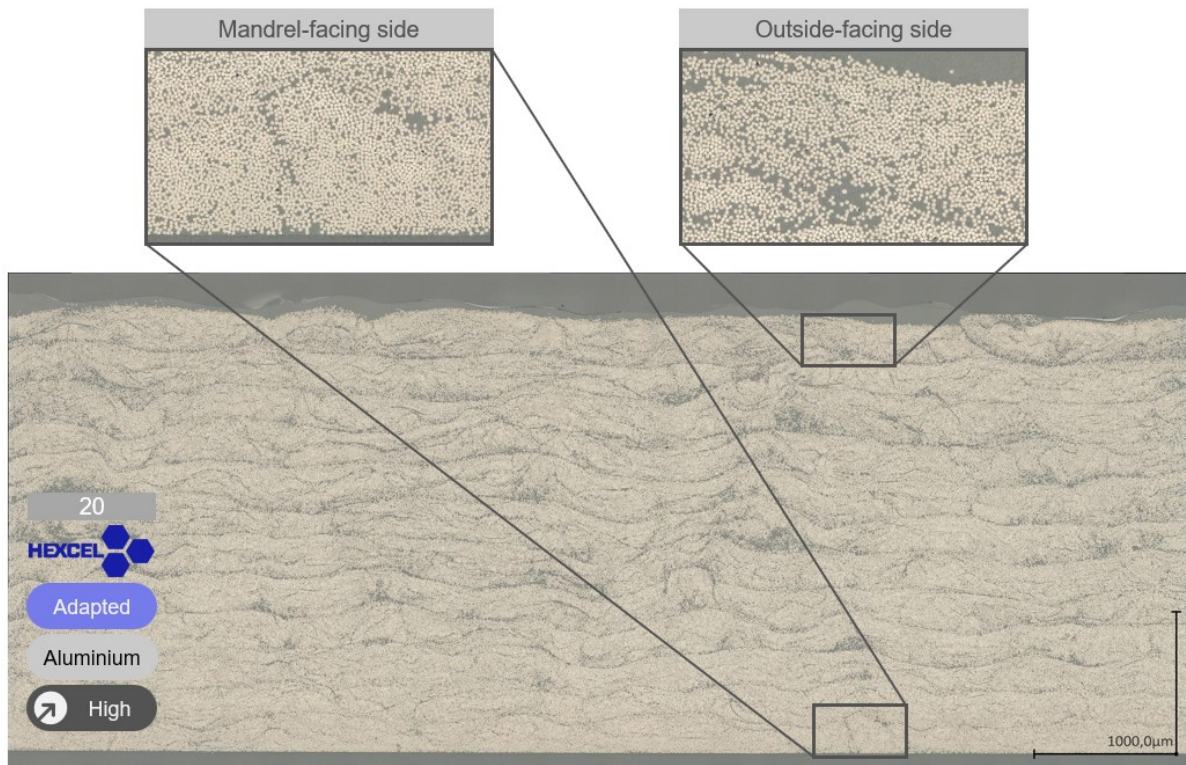
Figure C.11: Micrograph of specimen 20.
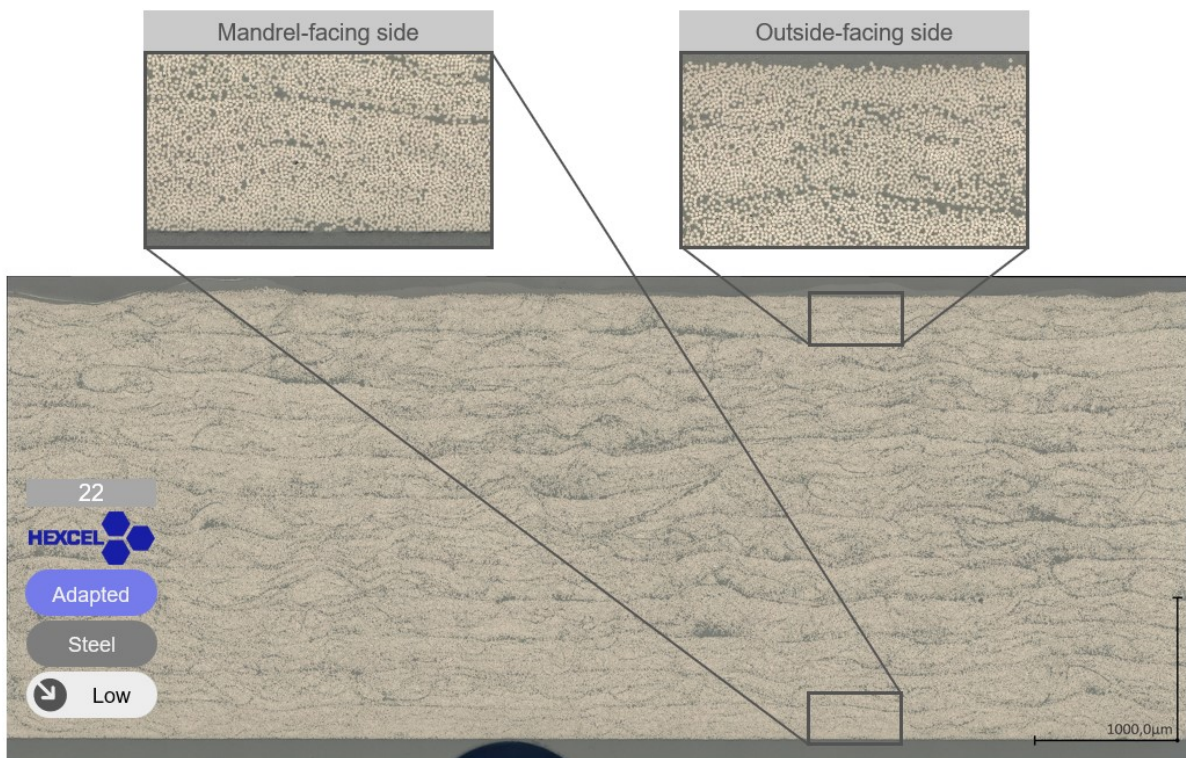
Figure C.12: Micrograph of specimen 22.

D

Heat-Maps
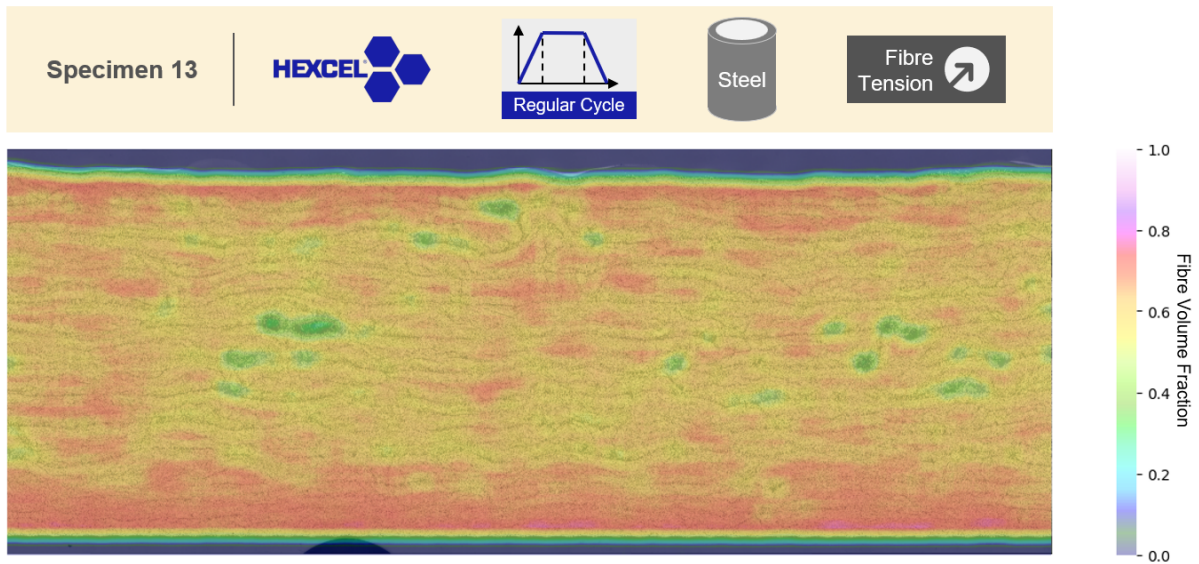
Figure D.1: Heat-Map of the local FVF of specimen 13.
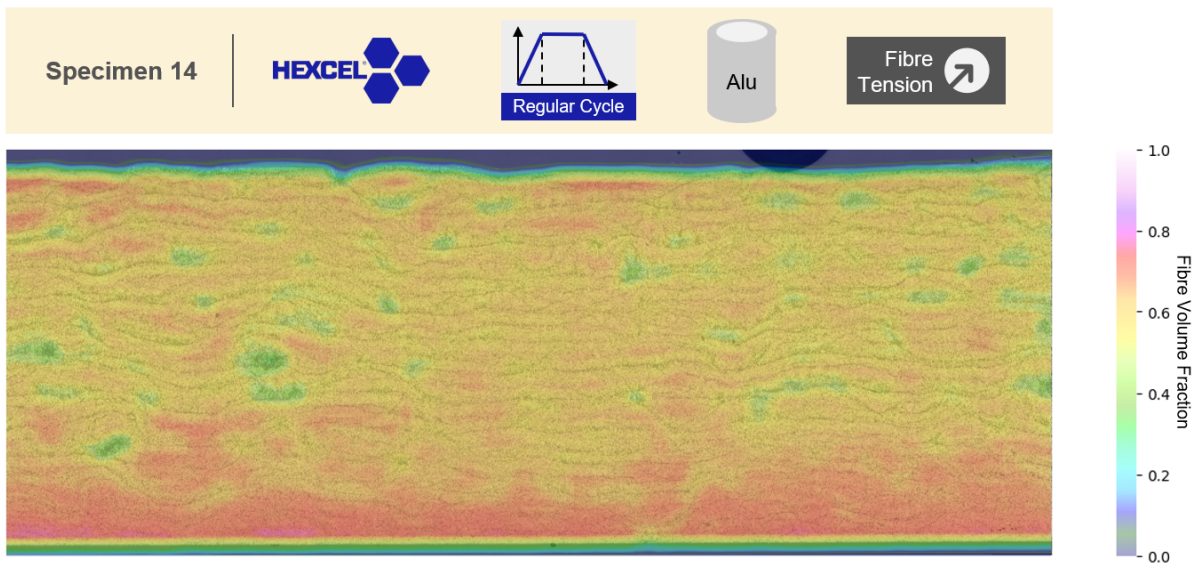
Figure D.2: Heat-Map of the local FVF of specimen 14.
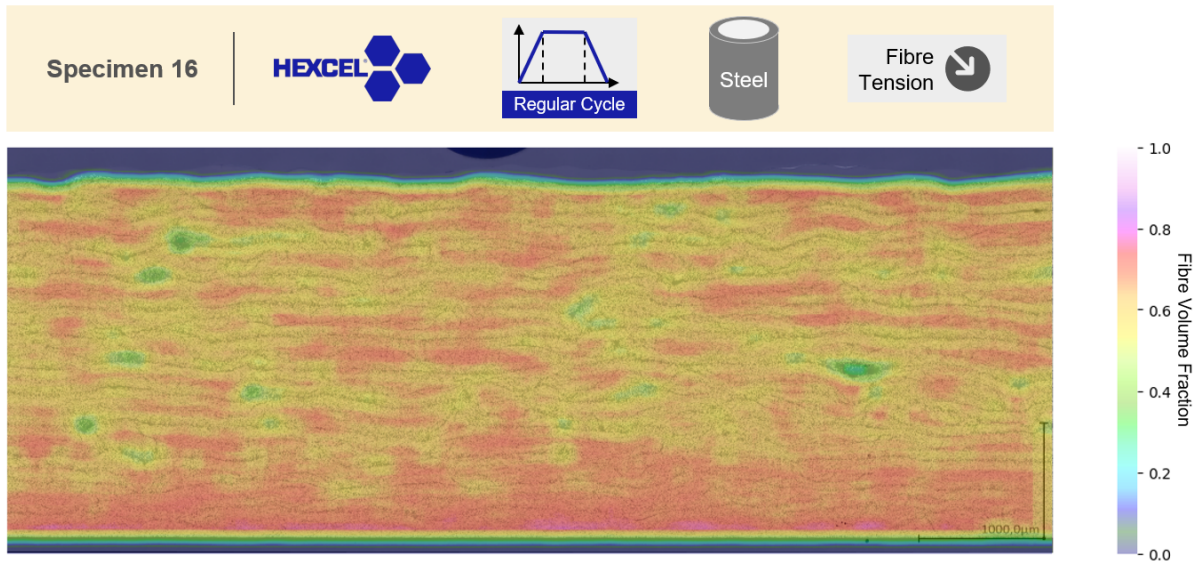
Figure D.3: Heat-Map of the local FVF of specimen 16.
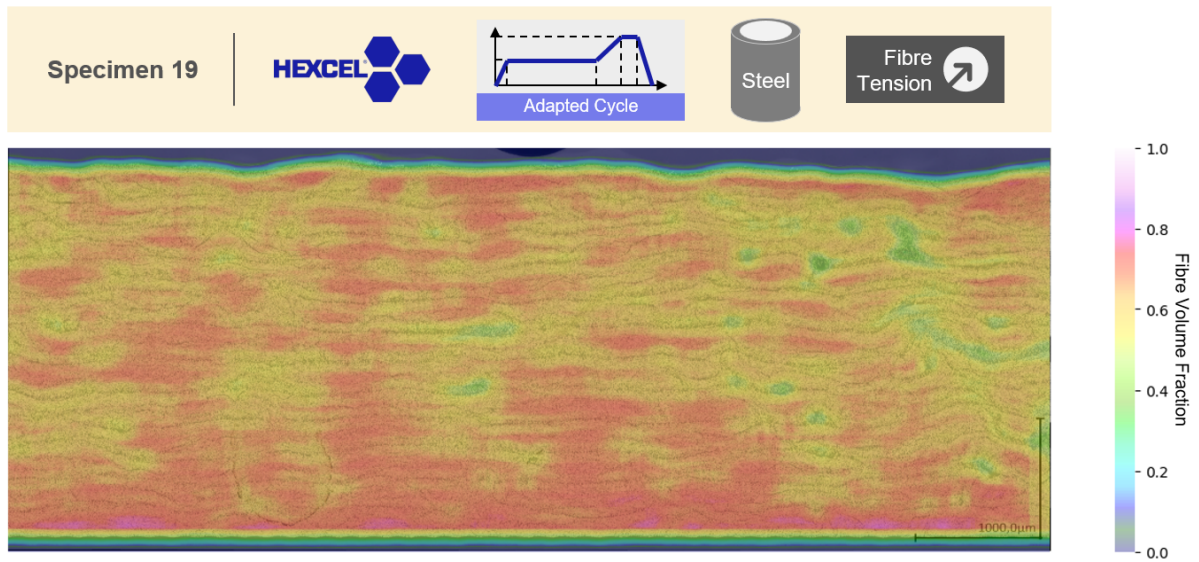
Figure D.4: Heat-Map of the local FVF of specimen 19.
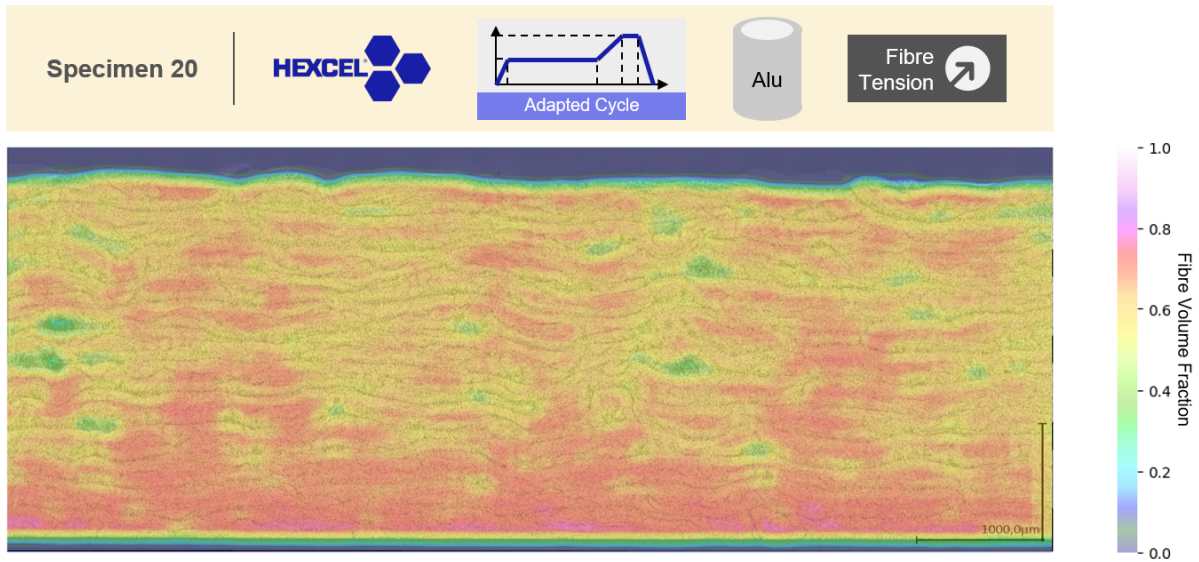
Figure D.5: Heat-Map of the local FVF of specimen 20.
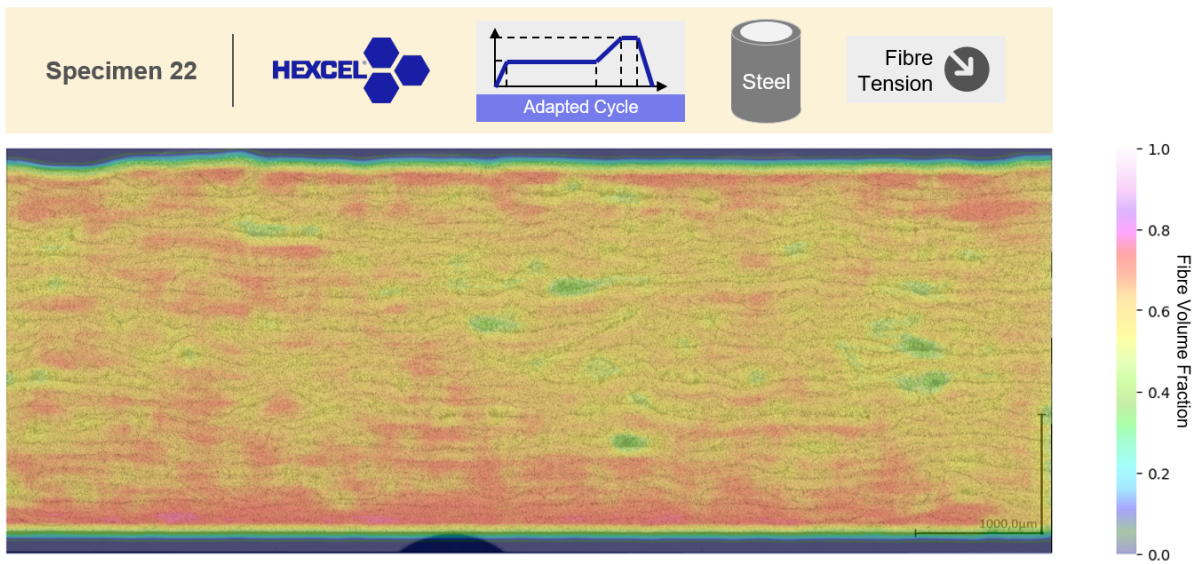
Figure D.6: Heat-Map of the local FVF of specimen 22.

E

Material Data Sheets

HexPly® 6376
175°C curing epoxy matrix

HEXCEL®

Description

HexPly® 6376 is a high performance tough matrix formulated for the fabrication of primary aircraft structures. It offers high impact resistance and damage tolerance for a wide range of high temperature applications.

Benefits and Features

- Excellent toughness and damage tolerance
- Simple straight-up cure cycle
- Controlled matrix flow for ease of processing
- Effective translation of fibre properties
- Good hot/wet properties up to 150°C

Resin Matrix Properties

Rheology

Viscosity/poise vs Temperature °C

Gel Time

Gel Time (minutes) vs Temperature °C
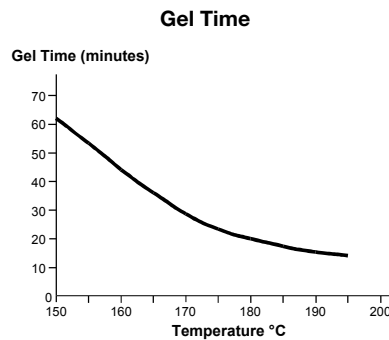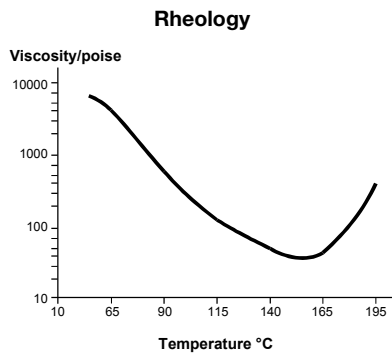
Cured Matrix Properties (cured at 175°C)

Property	Value	Method
Tensile strength	105 MPa	ISO R527 type 1
Tensile modulus	3.60 GPa	ISO R527 type 1
Tensile strain	3.1%	ISO R527 type 1
Flexural strength	144 MPa	ISO 178
Flexural modulus	4.4 GPa	ISO 178
Toughness G_{1C}	432 J/m²	Tested in accordance with EGF Task Group on Polymers and Composites protocol.
Cured density	1.31 g/cm³	

Prepreg Curing Conditions

2 hours at 175°C and 700kN/m² (7 bar) pressure.

Heat up rate 2°C to 5°C.

Components up to 30 mm thick can be cured without a dwell in the schedule provided that the heat-up rate is not more than 3°C/minute. There is no deterioration in performance after 3 times the recommended cure schedule (verified by interlaminar shear strength tests).

Prepreg Storage Life

- Tack Life   @ 23°C   10 days (still processable for up to 21 days).
- Guaranteed Shelf Life   @ -18°C   12 months *(maximum, from date of manufacture)*
- Storage conditions.

HexPly⁵ 6376 prepregs should be stored as received in a cool dry place or in a refrigerator. After removal from refrigerator storage, prepreg should be allowed to reach room temperature before opening the polythene bag, thus preventing condensation. (A full reel in its packaging can take up to 48 hours).

Precautions for Use

The usual precautions when handling uncured synthetic resins and fine fibrous materials should be observed, and a Safety Data Sheet is available for this product. The use of clean disposable inert gloves provides protection for the operator and avoids contamination of material and components.

For more information

Hexcel is a leading worldwide supplier of composite materials to aerospace and industrial markets.
Our comprehensive range includes:

- HexTow® carbon fibers
- HexForce® reinforcements
- HiMax® multiaxial reinforcements
- HexPly® prepregs
- HexMC®-i molding compounds

- HexFlow® RTM resins
- HexBond™ adhesives
- HexTool® tooling materials
- HexWeb® honeycombs
- Acousti-Cap® sound attenuating honeycomb

- Engineered core
- Engineered products
- Polyspeed® laminates & pultruded profiles
- HexAM® additive manufacturing

For U.S. quotes, orders and product information call toll-free 1-800-688-7734. For other worldwide sales office telephone numbers and a full address list, please go to:

https://www.hexcel.com/contact

FTA-051-MY20

Tenax™ Prepreg Q183 series is a rapid curing carbon fiber prepreg system. The resin formulation allows this prepreg to cure in approximately 20 minutes at a temperature of 160 °C, enabling short cycle out-of-autoclave press molding process for monolithic and sandwich core panel application. The increase in production efficiency due to this rapid processing enables high-rate composite manufacturing capacities. These system is mainly formulated for the aerospace industry to replace standard-cure materials.
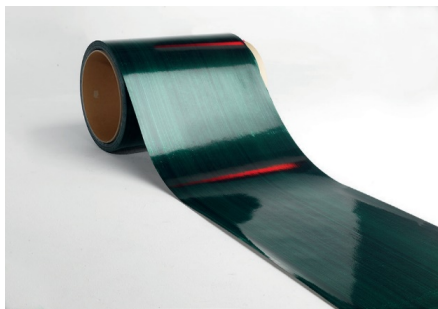
Product benefits

- For aerospace applications
- Excellent hot/wet properties
- Low void content
- Good tack and drape
- Typical prepreg shelf life

Process benefits

- Focused on high-rate part manufacturing
- Fully cured in 20 min – no post cure
- Designed for press cure but also applicable for autoclave cure
- Applicable for ATL and AFP process
- Cost effective

Physical properties

	Test method	Unit	Typical values
Resin density	ISO 1183	g/cm³	1.21
Volatile content	EN 2558	wt %	<0.5
Resin flow	EN 2560	wt %	6 - 8
Moisture uptake	EN 3615 (70 °C/85 % r.h.)	%	<1.5
DMA-T_G (Dry)	ASTM D7028	°C	182
DMA-T_G (Wet*)	ASTM D7028	°C	151

* Wet conditioning: 70 °C and 85 % r.h.

TEIJIN LIMITED
TEIJIN CARBON EUROPE GMBH
TEIJIN CARBON AMERICA, INC.

customer@teijin.co.jp
sales@teijincarbon.com
info@teijincarbon.us

www.teijincarbon.com

Version 1.0
2022-03-01
Page 1/8

Brand name	Tenax™	
Product designation	Q183-UD-194-34/STS-24K	
Style	UD	
Fiber	Tenax™-E STS40 E23 24K 1600tex	
Fiber areal weight	194 g/m²	
Resin	Q183	
Matrix content	34 %	
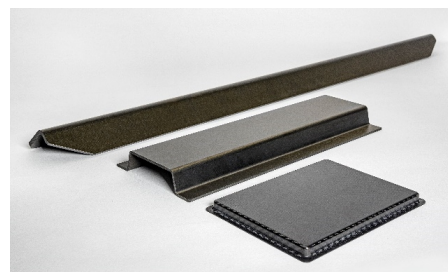
Properties (test direction)		Conditioning		Test temperature	Unit	Typical values
Tensile (0°) EN 2561 B	strength	dry:	23 °C / 50 % r.h.	RT	MPa	2066*
	modulus	dry:	23 °C / 50 % r.h.	RT	GPa	138*
Tensile (90°) EN 2597 B	strength	dry:	23 °C / 50 % r.h.	RT	MPa	72*
		wet:	70 °C / 85 % r.h.	70 °C	MPa	35*
	modulus	dry:	23 °C / 50 % r.h	RT	GPa	8.3*
		wet:	70 °C / 85 % r.h.	70 °C	GPa	7.2*
Compression (0°) EN 2850 A4	strength	dry:	23 °C / 50 % r.h.	RT	MPa	1386
		wet:	70 °C / 85 % r.h.	70 °C	MPa	1155
	modulus	dry:	23 °C / 50 % r.h.	RT	GPa	116
Compression (90°) EN 2850 B	strength	dry:	23 °C / 50 % r.h.	RT	MPa	209
		wet:	70 °C / 85 % r.h.	70 °C	MPa	164
	modulus	dry:	23 °C / 50 % r.h.	RT	GPa	8.3
Poissons ratio (0°/90°) EN 2561 B	-	dry:	23 °C / 50 % r.h.	RT	-	0.29
ILSS EN 2563	strength	dry:	23 °C / 50 % r.h.	RT	MPa	91*
		wet:	70 °C / 85 % r.h.	70 °C	MPa	66*

* Normalized to 57 % Vf%

TEIJIN LIMITED
TEIJIN CARBON EUROPE GMBH
TEIJIN CARBON AMERICA, INC.

customer@teijin.co.jp
sales@teijincarbon.com
info@teijincarbon.us

www.teijincarbon.com

Version 1.0
2022-03-01
Page 2/8

Brand name	Tenax™
Product designation	Q183-UD-268-34/ITS-24K
Style	UD
Fiber	Tenax™-E ITS55 E23 24K 1600tex
Fiber areal weight	268 g/m²
Resin	Q183
Matrix content	34 %
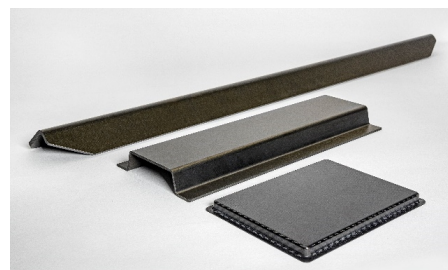
Properties (test direction)		Conditioning		Test temperature	Unit	Typical values
Tensile (0°) EN 2561 B	strength	dry:	23 ℃ / 50 % r.h.	RT	MPa	2690*
		wet:	70 ℃ / 85 % r.h.	70 ℃	MPa	2494*
	modulus	dry:	23 ℃ / 50 % r.h.	RT	GPa	162*
Tensile (90°) EN 2597 B	strength	dry:	23 ℃ / 50 % r.h.	RT	MPa	51*
		wet:	70 ℃ / 85 % r.h.	70 ℃	MPa	23*
	modulus	dry:	23 ℃ / 50 % r.h	RT	GPa	8.0*
		wet:	70 ℃ / 85 % r.h.	70 ℃	GPa	7.4*
Compression (0°) EN 2850 A4	strength	dry:	23 ℃ / 50 % r.h.	RT	MPa	1310
		wet:	70 ℃ / 85 % r.h.	70 ℃	MPa	951
	modulus	dry:	23 ℃ / 50 % r.h.	RT	GPa	131
Compression (90°) EN 2850 B	strength	dry:	23 ℃ / 50 % r.h.	RT	MPa	229
		wet:	70 ℃ / 85 % r.h.	70 ℃	MPa	163
	modulus	dry:	23 ℃ / 50 % r.h.	RT	GPa	9.4
		wet:	70 ℃ / 85 % r.h.	70 ℃	GPa	8.1
Poissons ratio (0°/90°) EN 2561 B	-	dry:	23 ℃ / 50 % r.h.	RT	-	0.32
ILSS EN 2563	strength	dry:	23 ℃ / 50 % r.h.	RT	MPa	81*
		wet:	70 ℃ / 85 % r.h.	70 ℃	MPa	59*

* Normalized to 57 % Vf%

TEIJIN LIMITED
TEIJIN CARBON EUROPE GMBH
TEIJIN CARBON AMERICA, INC.

customer@teijin.co.jp
sales@teijincarbon.com
info@teijincarbon.us

www.teijincarbon.com

Version 1.0
2022-03-01
Page 3/8

Brand name	Tenax™
Product designation	Q183-PW-193-38/HTS-3K
Style	Plain weave
Fiber	Tenax™-J HTS40 E13 3K 200tex
Fiber areal weight	193 g/m²
Resin	Q183
Matrix content	38 %
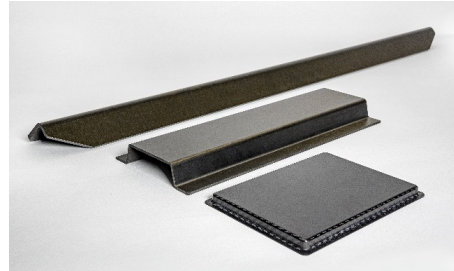
Properties (test direction)		Conditioning	Test temperature	Unit	Typical values
Compression (warp) EN 2850 B1	strength	dry: 23 °C / 50 % r.h.	RT	MPa	782*
		wet: 70 °C / 85 % r.h.	70 °C	MPa	484*
	modulus	dry: 23 °C / 50 % r.h.	RT	GPa	58*
Compression (weft) EN 2850 B2	strength	dry: 23 °C / 50 % r.h.	RT	MPa	789*
		wet: 70 °C / 85 % r.h.	70 °C	MPa	492*
	modulus	dry: 23 °C / 50 % r.h	RT	GPa	58*
ILSS EN 2563	strength	dry: 23 °C / 50 % r.h.	RT	MPa	67*
		wet: 70 °C / 85 % r.h.	70 °C	MPa	46*

* Normalized to 53 % Vf%

TEIJIN LIMITED
TEIJIN CARBON EUROPE GMBH
TEIJIN CARBON AMERICA, INC.

customer@teijin.co.jp
sales@teijincarbon.com
info@teijincarbon.us

www.teijincarbon.com

Version 1.0
2022-03-01
Page 4/8

Coefficient of thermal expansion (CTE)

Properties (Test direction)		Material	Test range	Unit	Typical values
CTE ASTM E381	0°	Q183-UD-194-34/ITS-24K	-30 °C – 200 °C	x10⁻⁵/°C	0.00
	90°		25 °C – 175 °C	x10⁻⁵/°C	3.98
	90°		175 °C – 200 °C	x10⁻⁵/°C	7.35
CTE ASTM E381	warp	Q183-2/2TW-285-38/HTS-6K	25 °C – 175 °C	x10⁻⁵/°C	-0.21
	warp		175 °C – 200 °C	x10⁻⁵/°C	-0.81
	weft		25 °C – 175 °C	x10⁻⁵/°C	0.19
	weft		175 °C – 200 °C	x10⁻⁵/°C	-0.09

Dynamic viscosity at 2 °C/minute
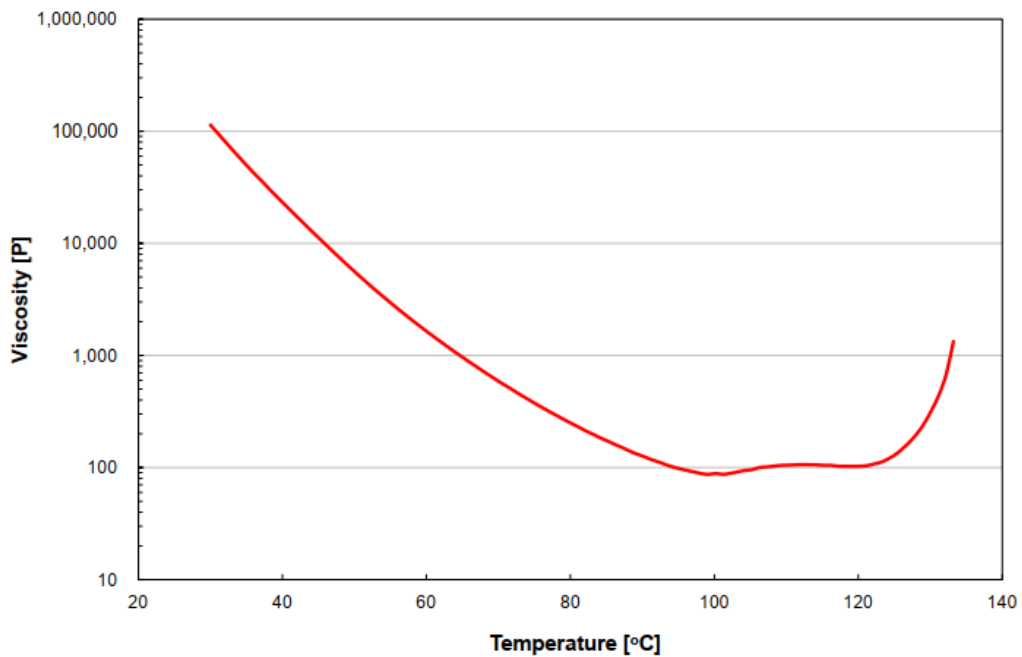
Gel time (Isothermal conditions)

Gel time at 100 ºC : 60 min.
at 120 ºC : 17 min.
at 140 ºC : 5.5 min.
at 150 ºC : 4.0 min.
at 160 ºC : 2.5 min.

TEIJIN LIMITED
TEIJIN CARBON EUROPE GMBH
TEIJIN CARBON AMERICA, INC.

customer@teijin.co.jp
sales@teijincarbon.com
info@teijincarbon.us

www.teijincarbon.com

Version 1.0
2022-03-01
Page 6/8
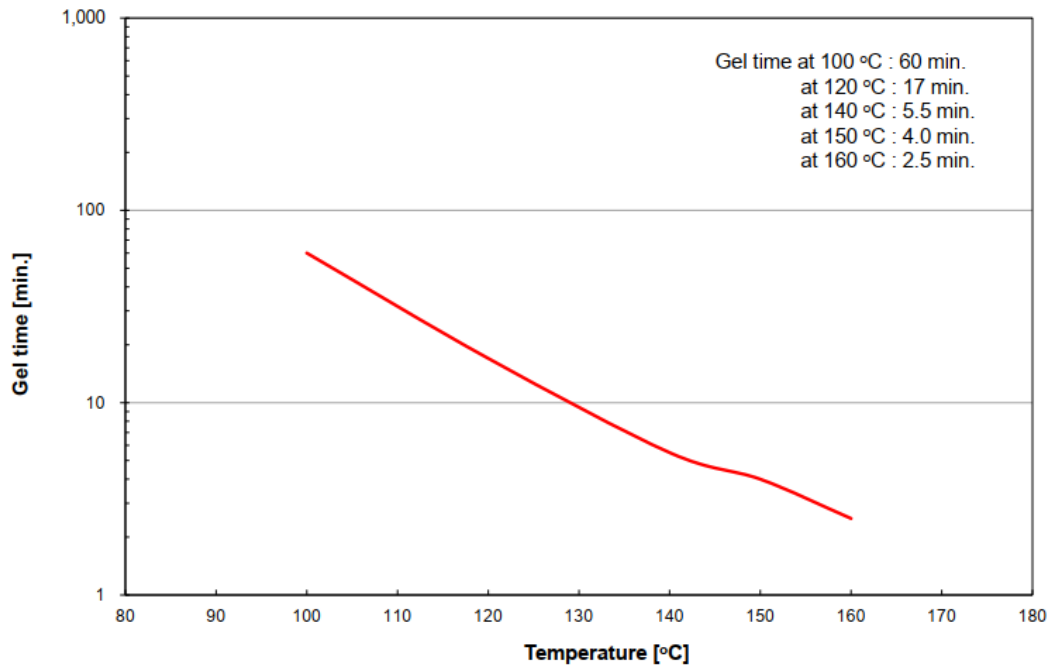
Prepeg curing conditions

Defined heat-up rates will vary depending on the size of the component to be manufactured.

- **Press cure** (compression molding)
    1. Set heat up to 160 ℃ ± 5 ℃ with heat-up rate between 50 - 100 ℃/minute (depending in mold tooling)
    2. Press pressure at 1 - 2 MPa (= 10 – 20 bar)
    3. Hold at 160 ℃ ± 5 ℃ for 20 minutes
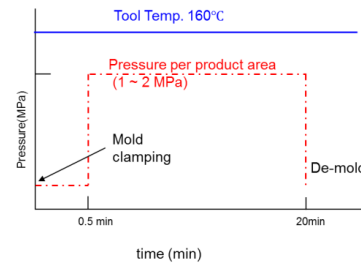
- **Autoclave cure** – monolithic parts
    1. Apply minimum vacuum (80 kPa)
    2. Apply typically 0.5 MPa of pressure to the laminate
    3. Set heat up to 160 ℃ ± 5 ℃ with heat-up rate between 2 - 5 ℃/minute
    4. Hold at 160 ℃ ± 5 ℃ for 20 minutes
    5. Cool component to 60℃ or below at a cool-down rate of 2 - 5 ℃/minute
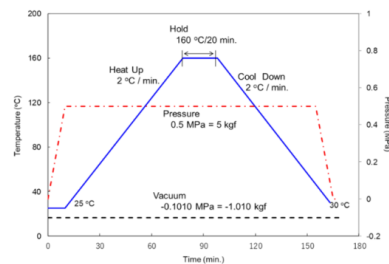
- **Autoclave cure** – sandwich parts
    1. Apply minimum vacuum (65 kPa)
    2. Apply 0.3 MPa of pressure to the laminate
    3. Vent the vacuum bag to atmospheric pressure once the pressure reaches 0.14 MPa
    4. Set heat-up to 160 ℃ ± 5 ℃ with heat-up rate between 2 - 5 ℃/minute
    5. Hold at 160 ℃ ± 5 ℃ for 20 minutes
    6. Cool component to 60℃ or below at a cool-down rate of 2 - 5 ℃/minute

TEIJIN LIMITED   customer@teijin.co.jp   www.teijincarbon.com   Version 1.0
TEIJIN CARBON EUROPE GMBH   sales@teijincarbon.com   2022-03-01
TEIJIN CARBON AMERICA, INC.   info@teijincarbon.us   Page 7/8
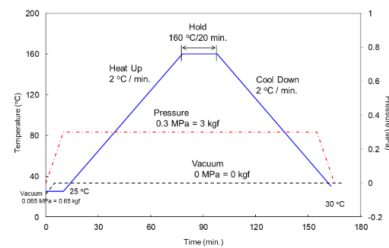
Storage condition and shelf life

- Storage at -18 ℃:   12 months from date of manufacture
- Storage at 23 ℃:   30 days from date of manufacture
- It is recommended that Tenax™ Thermoset Prepregs be stored in a dry cool area. User should allow the prepreg to reach room temperature before opening the sealed bag. The thawing time strongly depends on the amount of material on a single roll. Please contact us for more information.

Product form

- This product is available in a wide range of formats. Please contact us for more information.

Precautions for use

- A product information sheet on safe handling is available. Please contact us.

General Information

- All data shown are typical values representative of the material and cannot be guaranteed. Properties may vary depending on samples preparation and test methods.
- For each shipment an inspection certificate is generated and supplied.
- A detailed customer specification is arranged on request.
- The export or transfer of carbon fiber products can be subject to authorization, depending on end-use and final destination

TEIJIN LIMITED
TEIJIN CARBON EUROPE GMBH
TEIJIN CARBON AMERICA, INC.

customer@teijin.co.jp
sales@teijincarbon.com
info@teijincarbon.us

www.teijincarbon.com

Version 1.0
2022-03-01
Page 8/8

F

Pressure Sensor Data Sheet

FlexiForce™
Standard Model HT201

The FlexiForce HT201 is our enhanced thin and flexible piezoresistive force sensor ideal for high temperature applications. The HT201 is capable of measuring force and pressure in environments as hot as 400°F (approximately 200°C). These ultra-thin sensors are ideal for non-intrusive force and pressure measurement in a variety of applications. The HT201 can be used with our test & measurement, prototyping, and embedding electronics, including the FlexiForce Sensor Characterization Kit, FlexiForce Prototyping Kit, FlexiForce Quickstart Board, and the ELF™ System*. You can also use your own electronics, or multimeter.

Benefits

- Operates in temperatures up to approximately 200°C (400°F)
- Thin and flexible
- Easy to use
- Available off-the-shelf

√ ROHS COMPLIANT

Physical Properties

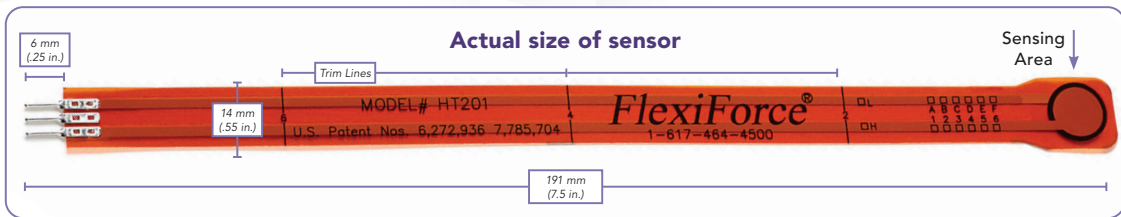|	
Thickness	0.203 mm (0.008 in.)
Length	191 mm (7.5 in.)** (optional trimmed lengths: 152 mm (6 in.), 102 mm (4 in.), 51 mm (2 in.))
Width	14 mm (0.55 in.)
Sensing Area	9.53 mm (0.375 in.) diameter
Connector	3-pin Male Square Pin (center pin is inactive)
Substrate	Polyester
Pin Spacing	2.54 mm (0.1 in.)

* *Sensor will require an adapter/extender to connect to the ELF System. Contact your Tekscan representative for assistance.*
** *Length does not include pins. Please add 31.75 mm (0.25 in.) for pin length to equal a total length of 203.2 mm (8 in.).*

	Typical Performance (Ambient Temperature)	Evaluation Conditions	***
Linearity (Error)	< ±3% of full scale****	Line drawn from 0 to 50% load	
Repeatability	< ±3.5%	Conditioned sensor, 80% of full force applied	
Hysteresis	< 3.6% of full scale	Conditioned sensor, 80% of full force applied	
Drift	< 3.3% per logarithmic time scale	Constant load of 111 N (25 lb)	
Response Time	< 5μsec	Impact load, output recorded on oscilloscope	
Operating Temperature	-40°C - 240°C (-40°F - 400°F)	Convection and conduction heat sources	
Durability	≥ 3 million actuations	Perpendicular load, room temperature, 22 N (5 lb)	
Temperature Sensitivity	0.36%/°C (± 0.2%/°F)	Conductive heating	

***All data above was collected utilizing an Op Amp Circuit (shown on the next page). If your application cannot allow an Op Amp Circuit, visit www.tekscan.com/flexiforce-integration-guides, or contact a FlexiForce Applications Engineer. Specifications based on pressures up to 500 psi and represent the average value throughout a range of temperatures up to 400°F.

**** Linearity up to 889 N (200 lb).

ISO 9001:2008 Compliant & 13485:2016 Registered

Tekscan™

Actual size of sensor

6 mm
(.25 in.)

Trim Lines

14 mm
(.55 in.)

MODEL# HT201
U.S. Patent Nos. 6,272,936 7,785,704

FlexiForce®
1-617-464-4500

Sensing
Area

191 mm
(7.5 in.)

Standard Force Ranges
as Tested with Circuit Shown

222 N (0 - 50 lb) [†]

[†] This sensor can measure up to 2,224 N (500 lb). In order to measure forces outside specified ranges, use recommended circuit and adjust drive voltage and/or reference resistance.

Sensor output is a function of many variables, including interface materials. Therefore, Tekscan recommends the user calibrate each sensor for the application. The graph below is an illustration of how a sensor can be used to measure varying force ranges by changing the feedback resistor (**Figure 1** should not be used as a calibration chart).
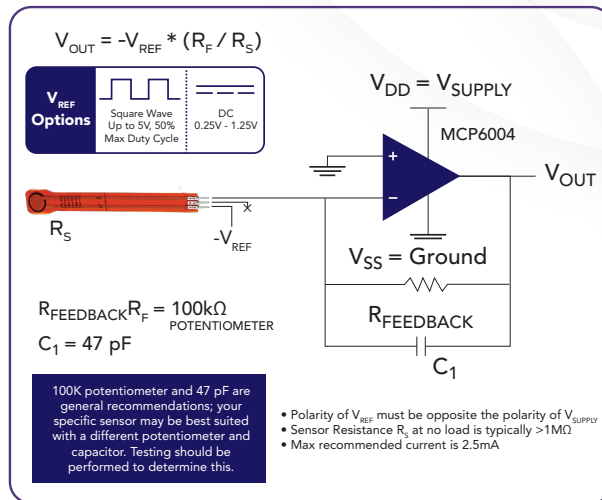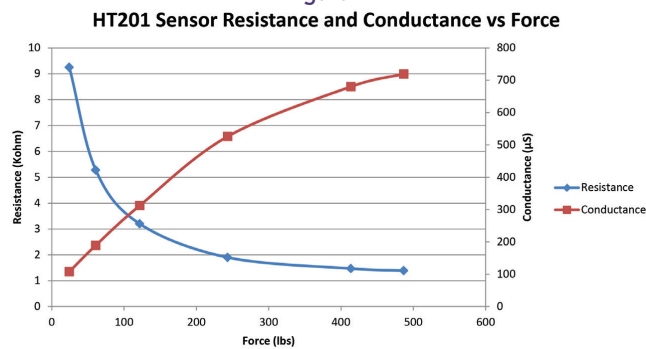
Recommended Circuit

$$V_{OUT} = -V_{REF} * (R_F / R_S)$$

V_{REF} Options

Square Wave Up to 5V, 50% Max Duty Cycle

DC 0.25V - 1.25V

R_S

$-V_{REF}$

$V_{DD} = V_{SUPPLY}$

MCP6004

V_{OUT}

V_{SS} = Ground

$R_{FEEDBACK}$ R_F = 100kΩ POTENTIOMETER

C_1 = 47 pF

$R_{FEEDBACK}$

C_1

100K potentiometer and 47 pF are general recommendations; your specific sensor may be best suited with a different potentiometer and capacitor. Testing should be performed to determine this.

• Polarity of V_{REF} must be opposite the polarity of V_{SUPPLY}
• Sensor Resistance R_S at no load is typically >1MΩ
• Max recommended current is 2.5mA

Figure 1
HT201 Sensor Resistance and Conductance vs Force

PURCHASE TODAY ONLINE AT WWW.TEKSCAN.COM/STORE

Ask Us About Our
VOLUME
DISCOUNTS